

Tools for designing the next generation of stellarators

Inauguraldissertation

zur

Erlangung des akademischen Grades eines
Doktors der Naturwissenschaften
(Dr. rer. Nat.)

der

Mathematisch-Naturwissenschaftlichen Fakultät

der

Universität Greifswald

vorgelegt von
Jim-Felix Eduard
Lobsien
geboren am 26.06.1988
in Berlin

Greifswald, 09.09.2020

Dekan	Prof. Dr. Werner Weitschies
1. Gutachter	Prof. Dr. Thomas Sunn Pedersen
2. Gutachter	Prof. Dr. David Bindel
Tag der Promotion:	26.08.2020

“The beauty of science is that all the
important things are unpredictable.”

Freeman Dyson

Contents

1. Introduction	1
1.1. Plasma Physics	3
1.1.1. Plasma Description	4
1.1.2. Magnetic Field Properties	7
1.1.3. Equilibrium Properties	9
1.2. Stellarator	17
1.3. Stellarator Optimization	20
1.4. Stellarator Coil Optimization	23
1.5. Construction of Stellarators	30
1.5.1. Construction of Wendelstein 7-X	30
1.5.2. Construction of NCSX	31
1.5.3. Construction of CNT	31
1.5.4. Final Remarks	32
1.6. Stochastic Stellarator Coil Optimization	32
2. Summary of Articles	37
2.1. Article I: Stellarator coil optimization towards higher engineering tolerances	38
2.2. Article II: Physics analysis of results of stochastic and classic stellarator coil optimization	40
2.3. Article III: Improved performance of stellarator coil design optimization	41
3. Near Term Objectives	43
3.1. Stochastic Version of FOCUS	46
3.2. Stochastic Stellarator Optimization	47
3.3. United Stochastic Stellarator and Coil Optimization	47
Bibliography	49

Contents

Acronyms	59
List of Symbols	61
List of Figures	67
A. Thesis Articles	69
A.1. Article I	72
A.2. Article II	88
A.3. Article III	117
B. CV	135
C. Acknowledgements	137
Eigenständigkeitserklärung	139

1

Introduction

In the 21st century the world needs to reconsider its energy production mix. In its recent energy study [1], the Federal Institute for Geosciences and Natural Resources estimated an annual world energy consumption of 609 EJ in 2017, which reflects the primary energy used globally. It consisted of 77% fossil fuels, 5% nuclear fuels and 18% renewables. They estimate the combined global reserves and resources to be 580 769 EJ of fossil fuels, and 9651 EJ of nuclear fission fuels. Thus, assuming a constant energy consumption, the world could sustain its energy needs approximately 1000 (16) years relying on fossil fuels (nuclear fuels) only, but the rising effects of climate change ought to prohibit the further use of fossil fuels and the danger and unimaginable long lifetime of nuclear fission waste questions the economical and safety aspects of fission energy production. Renewable energy production is on the rise, but the distribution of hydro and geothermal resources is sparse and the weather dependent fluctuations of wind and solar energy unavoidably limit their practicability [2]. It is important to understand that any possible energy crisis of the 21st century will not be caused by the lack of resources, but rather by their excessive use on one side and the lack of efficient energy storage systems on the other. Nuclear fusion has the potential to solve this dilemma thanks to its base load capability, unlimited fuel resources and near environmental perfection [3]. A promising candidate for such a future fusion reactor is the stellarator, but its design and construction are very challenging. The path to the first fusion power plant consists of even more challenging science and engineering problems, but the technique of stochastic stellarator design, where the first tools are described in this thesis, has the potential to solve two of them explained hereinafter.

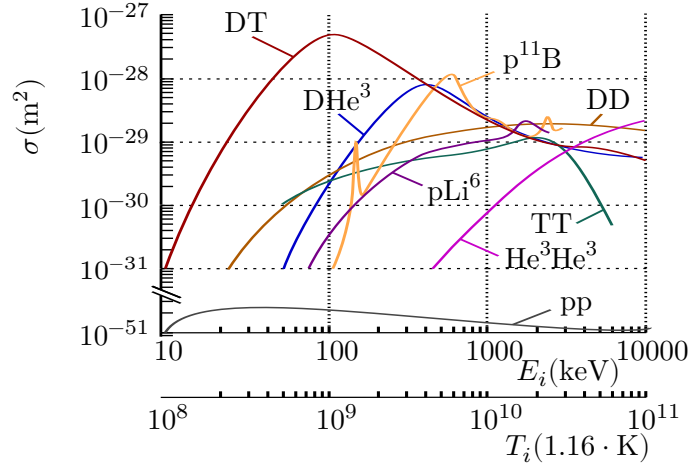
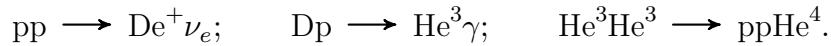


Figure 1.1.: Experimentally measured cross sections for the DT, DD, TT, DHe³, He³He³, pLi⁶, pB¹¹, and pp fusion reactions as a function of the center of mass energy of the two particles. The y-axis is broken to fit the mentioned cross sections onto one coordinate system. The pD cross section is not shown because it is on the order of $1 \times 10^{-32} \text{ m}^2$. Source [4].

Nuclear Fusion has the potential to be the energy source of the future. In a fusion reaction, two light nuclei merge and release on the order of one million times more energy per elementary particle than any chemical reaction. Instead of using the potential energy of electrons within the atomic structure, a nuclear reaction releases nuclear binding energy by decreasing the final mass of the nuclei, which is transformed into their kinetic energy. Mass and energy are related by Einstein's famous formula

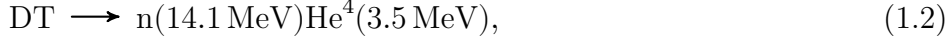
$$E = mc^2. \quad (1.1)$$

The sun converts the energy of nuclear fusion into a useful societal application already for billions of years by fusing hydrogen to helium according to the following reaction chain [5]



The probability that any of these two nuclei will overcome the repelling Coulomb force and undergo a nuclear fusion reaction is defined by their reaction cross section (see figure 1.1). The very low reaction rate of the pp reaction makes the fusion reaction of the Sun impractical on Earth, but by

defining the life-time of the Sun it made life on Earth possible. Figure 1.1 shows the reaction cross section of many possible fusion reactions, of which the deuterium-tritium (two hydrogen isotopes with one and two neutrons) reaction has the most favorable reaction cross section, which peaks at a center of mass energy of 100 keV. Its reaction follows



producing a neutron and a helium nucleus. Realizing many of these reactions simultaneously requires a shift from the single particle description to a thermodynamic description of gases. At these temperatures, a DT-gas will be a plasma consisting of charged particles in which Coulomb collisions lead to a Maxwellian distribution. Fusion ignition is reached when the energy of the 3.5 MeV α -particles is sufficient to sustain the temperature of the plasma by transfer of its energy to the DT-plasma through binary collisions. The optimal temperature is about 15 keV [3] and most of the fusion reactions occur for particles on the high energy tail of the distribution function. The remaining values for the density n and energy confinement time τ_E required for fusion ignition can be derived from the triple product criterion [6]

$$nT_i\tau_E \geq 3 \times 10^{21} \text{ keV s m}^{-3}. \quad (1.3)$$

It requires, in addition to a temperature of 15 keV, a combined density and energy confinement time of $n\tau_E \geq 2 \times 10^{20} \text{ s m}^{-3}$. The ignition requirement assumes that the DT-plasma is stationary and confined by electromagnetic fields. In a future fusion reactor the power for electricity is obtained from the 14.1 MeV neutrons which are not affected by the electromagnetic fields and can leave the inner vessel of the fusion reactor. The neutrons will be, additionally, used to breed tritium from lithium, since tritium does not occur naturally on earth.

1.1. Plasma Physics

Plasma is defined as a quasi-neutral gas of charged (and neutral) particles that exhibits collective behavior [7]. The term appeared first in a study of gas discharges by Tonks and Langmuir in 1929 [8]. It is an electrically conducting gas that strongly responds to electromagnetic fields such that

its motion depends not only on local conditions but on the state of the plasma in remote regions as well [7]. The necessity to describe a plasma as an electromagnetic fluid is primarily the reason to refer to it as the fourth state of matter, distinct from ordinary gases [9].

1.1.1. Plasma Description

Any plasma description starts with Maxwell's equations, the set of four coupled partial differential equations that constitute the foundation of electromagnetism:

$$\nabla \cdot \mathbf{E} = \frac{\varrho}{\epsilon_0}, \quad (\text{Gauss's law}) \quad (1.4)$$

$$\nabla \cdot \mathbf{B} = 0, \quad (\text{Gauss's law for magnetism}) \quad (1.5)$$

$$\nabla \times \mathbf{E} = -\frac{\partial \mathbf{B}}{\partial t}, \quad (\text{Maxwell-Faraday equation}) \quad (1.6)$$

$$\nabla \times \mathbf{B} = \mu_0 \left(\mathbf{J} + \epsilon_0 \frac{\partial \mathbf{E}}{\partial t} \right). \quad (\text{Ampère's law}). \quad (1.7)$$

They describe the divergence and curl of the electric \mathbf{E} and magnetic field \mathbf{B} in terms of their mutual time evolution, the charge density ϱ , and the current density \mathbf{J} . Here, ϵ_0 and μ_0 denote the electric vacuum permittivity and magnetic vacuum permeability. An additional connection to Boltzmann's kinetic model and a subsequent derivation of the mass, momentum and energy moments leads to the theory of magnetohydrodynamics (MHD) that describes the plasma as a single, electrically conducting, but uncharged fluid with density ϱ , flow velocity \mathbf{v} and pressure p . The first and second moment lead to the conservation of mass relation and the MHD equation of motion:

$$\frac{\partial \varrho}{\partial t} + \nabla \cdot (\varrho \mathbf{v}) = 0, \quad (\text{Continuity equation}) \quad (1.8)$$

$$\varrho \frac{d\mathbf{v}}{dt} - \mathbf{J} \times \mathbf{B} + \nabla p = 0. \quad (\text{MHD equation of motion}) \quad (1.9)$$

The equation of motion (eq. 1.9) uses the convective derivative, i.e.

$$\frac{d}{dt} = \frac{\partial}{\partial t} + \mathbf{v} \cdot \nabla, \quad (1.10)$$

which is taken w.r.t. a moving frame. The equation of motion (eq. 1.9), additionally, assumes a vanishing resistivity related to ideal MHD that transforms the plasma into a perfect conductor. Thus, the electric field vanishes in a frame moving with the fluid:

$$\mathbf{E} + \mathbf{v} \times \mathbf{B} = 0. \quad (\text{Ideal Ohm's law}) \quad (1.11)$$

The third momentum leads to the energy equation, which states that entropy is a convective invariant in ideal MHD

$$\frac{d}{dt} \left(\frac{p}{\rho^{5/3}} \right) = 0. \quad (\text{Adiabatic energy equation}) \quad (1.12)$$

The assumptions underlying the MHD equations are valid for fusion plasmas except that the collisionality is low, which however does not play an important role in most MHD stability and equilibrium phenomena.

The time-independent static form ($\mathbf{v} = 0$) of the MHD equations are the the equilibrium equations:

$$\mathbf{J} \times \mathbf{B} = \nabla p, \quad (\text{Force balance}) \quad (1.13)$$

$$\nabla \times \mathbf{B} = \mu_0 \mathbf{J}, \quad (\text{Reduced Ampère's law}) \quad (1.14)$$

$$\nabla \cdot \mathbf{B} = 0. \quad (\text{Divergence constraint}) \quad (1.15)$$

The magnetic force $\mathbf{J} \times \mathbf{B}$ is balanced by the pressure gradient force ∇p , leading to surfaces of constant pressure

$$\mathbf{B} \cdot \nabla p = 0. \quad (1.16)$$

The "hairy ball" theorem states that such a non-vanishing tangential vector field can only be realized on the torus [10]. Hence, nested toroidal surfaces are traced out by magnetic field lines, which degenerate in the center to the single magnetic line of maximum pressure called the *magnetic axis*.

It follows from the ideal Ohm's law (eq. 1.11) that field lines are "frozen in" the magnetic field which prevents it from changing their topology within the description of ideal MHD. Consequently, the toroidal and poloidal flux

$$\psi = \int_{S_\varphi} \mathbf{B} \cdot d\mathbf{S}, \quad (\text{Toroidal flux}) \quad (1.17)$$

$$\chi = \int_{S_\vartheta} \mathbf{B} \cdot d\mathbf{S} \quad (\text{Poloidal flux}) \quad (1.18)$$

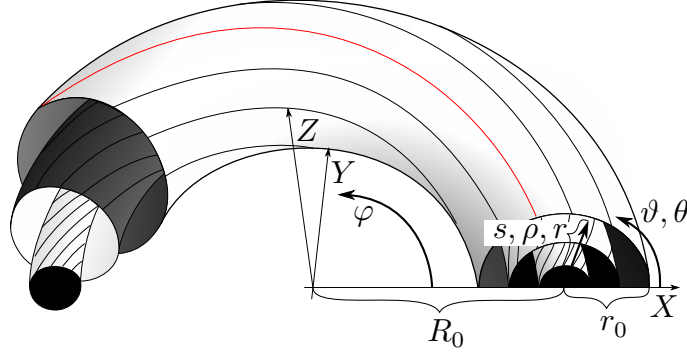


Figure 1.2.: Field lines generating nested magnetic flux surfaces. Source [4].

are conserved on surfaces of constant pressure, leading to the term *flux surfaces*. The surfaces of constant pressure S_φ and S_ϑ keep the toroidal angle φ and the poloidal angle ϑ constant, respectively. Extending the two angles by a minor radius leads to a toroidal coordinate system as visualized in figure 1.2. The minor radius can be measured in terms of the toroidal flux, which is denoted by s when normalized to the toroidal flux of the outermost flux surface. Taking the squared root of s defines the normalized minor radius $\rho := \sqrt{s}$, which is frequently used throughout the attached **Article I, II and III**. If the minor radius is not normalized, we denote it with r . The ratio of the major radius R_0 (distance from the origin to the magnetic axis) to the minor radius of the outermost flux surface r_0 defines the aspect ratio $A = R/r_0$. An equivalent coordinate system is the cylindrical coordinate system related via

$$R = R_0 + \rho \cos \vartheta \quad (1.19)$$

$$Z = \rho \sin \vartheta. \quad (1.20)$$

Using the properties of the magnetic field, one can transform an arbitrary toroidal coordinate system $(\rho, \vartheta, \varphi)$ into magnetic coordinates in Clebsch form

$$\mathbf{B} = \nabla\psi \times \nabla\theta + \nabla\varphi \times \nabla\chi, \quad (1.21)$$

that keep ψ and χ constant on flux surfaces while the magnetic field lines are straight in terms of the other coordinates [11]. Here $\theta = \vartheta + \gamma$, where γ is

some arbitrary function divided by the derivative of the toroidal flux ψ' . This version of magnetic coordinates, where the toroidal angle φ does not change during the coordinate transformation, are referred to as PEST coordinates [12]. Other important magnetic coordinates are Boozer coordinates [13], where the field lines are never perpendicular to \mathbf{B} , but always tangential to flux surfaces ψ , and Hamada coordinates [14], where the streamlines of \mathbf{B} and \mathbf{J} are straight.

1.1.2. Magnetic Field Properties

The change of the poloidal flux with respect to the toroidal flux defines the *rotational transform*

$$\iota(\psi) = \frac{d\chi}{d\psi} = \frac{d\theta}{d\varphi}, \quad (1.22)$$

which quantifies how many times a field line turns poloidally within one toroidal turn around the flux surface. If ι is rational, i.e. $\iota \in \mathbb{Q}$, then the field line exactly closes on itself after a finite number of toroidal turns. At these *rational surfaces*, closed magnetic flux tubes may emerge that are called *magnetic islands*. If ι is irrational, i.e. $\iota \in \mathbb{R}/\mathbb{Q}$, then the field line covers the whole flux surface by going around it ergodically. When magnetic surfaces break up, *stochastic regions* emerge where the field lines fill a finite volume. From eq. (1.16) it follows that p is constant over the whole stochastic volume, which implies that the transport is infinitely large [15].

The change of ι across the toroidal domain is captured by its radial gradient

$$\varsigma = -\frac{r}{\iota} \frac{d\iota}{dr}, \quad (1.23)$$

and is called the *magnetic shear*. The total toroidal volume of the magnetic domain is defined as

$$V = \int \int \int \sqrt{g} d\psi d\theta d\varphi, \quad (1.24)$$

where $\sqrt{g} = \mathbf{r}_\psi \cdot \mathbf{r}_\theta \times \mathbf{r}_\varphi$ is the Jacobian. One can define the derivative of the volume V w.r.t ψ

$$V' = \frac{dV}{d\psi} = \int \int \sqrt{g} d\theta d\varphi, \quad (1.25)$$

called the *specific magnetic volume* as the average line integral normalized by the magnetic field strength [16]

$$V' = \lim_{N \rightarrow \infty} \frac{1}{N} \int_N \frac{dl}{B}. \quad (1.26)$$

Naturally, the contained volume increases in radial direction, $V'(s) > 0$, and the magnetic field has a *magnetic well* when the rate of increase decreases with radius [17], i.e.

$$V'' = \frac{dV'}{d\psi} = \int \int \frac{\partial \sqrt{g}}{\partial \psi} d\theta d\varphi < 0. \quad (1.27)$$

Using the maximum (minimum) magnetic field strength along a field line l

$$B_{\max} := \max_{x \in l} |\mathbf{B}(x)| \quad (1.28)$$

$$B_{\min} := \min_{x \in l} |\mathbf{B}(x)|, \quad (1.29)$$

one is able to define the *magnetic mirror*

$$m := \frac{B_{\max} - B_{\min}}{B_{\max} + B_{\min}}. \quad (1.30)$$

Continuous Symmetry of the magnetic domain in toroidal direction is called *axisymmetry* and reduces the magnetic field of interest to a function of two dimensions. Poloidal or helical symmetry are absent in toroidal geometry and can only occur in unbounded magnetic fields. Toroidal magnetic fields without axisymmetry are functions of three dimensions. They are able to possess so-called *quasisymmetry*, i.e. quasi-axisymmetry, quasi-helical symmetry or quasi-poloidal symmetry. Among many equivalent definitions, quasi-symmetry is achieved when $\mathbf{B} \cdot \nabla B$ is a function that only depends on the flux ψ and the magnetic field strength B [18], such that the guiding center particle trajectories behave exactly as if they were in a truly symmetric magnetic field. Unfortunately, it is not possible to achieve exact quasi-symmetry in the whole magnetic domain, only on isolated surfaces [19].

High quality of vacuum magnetic field surfaces is desired to properly confine the plasma. In low-shear configurations, low-order rational values of the rotational transform ι should be avoided, since it is most likely that islands arise at these rational surfaces, that reduce the confinement. Also, stochastic regions are undesirable due to poor confinement. A low order rational value at the boundary of the confinement region will guarantee good magnetic surfaces and may establish an outer island chain that can eventually be used for a particle exhaust.

1.1.3. Equilibrium Properties

We describe the properties of a plasma that is confined by a toroidal magnetic field \mathbf{B} and is in equilibrium according to eq. (1.13), (1.14), and (1.15). The space between the plasma and the outer wall is characterized by very low density and can be approximated by a vacuum. In the MHD equations, the system is mathematically described by the vector field \mathbf{B} and the scalar function p .

The total energy of the system in equilibrium is defined by the thermal and magnetic energy

$$W = \int_V \left(\frac{B^2}{2\mu_0} + p \right) dV. \quad (1.31)$$

The MHD equilibrium can be computed by minimizing eq. (1.31) in a toroidal domain under certain constraints as done by the variational moments equilibrium code (VMEC) [20]. In its first version, VMEC described the plasma as contained within a fixed boundary, but was later extended to include an exterior vacuum region [21], essentially solving a free boundary problem. The ratio of average thermal to average magnetic energy

$$\langle \beta \rangle = \frac{3/2 \langle p \rangle}{\langle B^2/2\mu_0 \rangle} \quad (1.32)$$

is used as an economic measure of the underlying reactor concept. The higher the thermal pressure for a given magnetic pressure, the higher is the triple product (eq. 1.3), which can be reformulated to

$$p\tau_E \geq 3 \times 10^{21} \text{ keV s m}^{-3}, \quad (1.33)$$

where the confinement time $\tau_E \propto B^{0.84}$ (see ISS04 scaling [22]) depends among other things on the magnetic field strength B .

Good finite- β Equilibrium Properties are present when the rotational transform ι , the shear, and the position of the magnetic axis are only marginally affected by an increase of β . The shift of the magnetic axis is called *Shafranov shift* and occurs, when $\beta \ll 1$, linearly with the increase of $\langle\beta\rangle$. The origin of the deformation of the magnetic field can be explained by the force balance (eq. 1.13). An increase in pressure p leads to an increase of the internal plasma currents \mathbf{J} that are not equally distributed due to the toroidal shape of the equilibrium. A stronger poloidal field contribution from the current on the inboard side compared to the outboard side shifts the magnetic field radially outward and changes its interior. Thus, good finite- β equilibrium properties can be achieved by reducing the parallel current density [23]

$$\mathbf{J}_{\parallel}^2 / \mathbf{J}_{\perp}^2 \lesssim 1. \quad (1.34)$$

The subscripts $_{\parallel}$ and $_{\perp}$ denote the component parallel and perpendicular to the magnetic field \mathbf{B} .

Stability Theory perturbs the MHD equilibrium and analyzes the growing, oscillating or damped behavior. Perturbations that destabilize the plasma become more severe at high values of β , the stability limit of a configuration being the threshold β -value between stable and unstable MHD properties.

An MHD equilibrium is said to be stable if the sum of the magnetic and thermal plasma energy increases as a result of any admissible displacements, or unstable if a perturbation exists for which the energy decreases [24], respectively. Admissible perturbations are those with bounded kinetic energy that satisfy the boundary conditions of the equilibrium and the other constraints of ideal MHD. It is assumed that plasma perturbations are small enough that only the linear terms of the perturbations need to be considered. The linearized equations of ideal MHD can be cast into a second-order in time differential equation for the displacement employing the ideal MHD force operator with time-independent coefficients. Separating temporal and spatial dependence leads to an eigenvalue problem for the force operator. The so-called *mode analysis* answers the stability question by evaluating the sign of the lowest eigenvalue [25]. In addition to the global assessment of ideal MHD, local criteria are available that evaluate the stability on flux surfaces (for example, Mercier criterion [26] or resistive interchange [27]), along

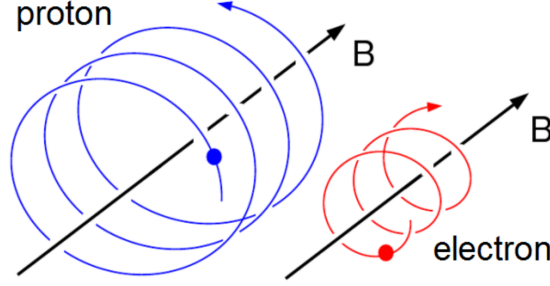


Figure 1.3.: Motion of charged particles in a magnetic field. Source [30].

field lines in flux tubes (local field line ballooning), or localized at the edge (peeling modes [28]). Ballooning modes are driven by the pressure gradient ∇p . Global ballooning stability can be calculated numerically by the Code for the Analysis of the MHD Stability of 3D Equilibria (CAS3D) which uses features of the perturbation function and the stellarator symmetry to make the problem tractable and facilitate their description.

For stellarators with flat rotational transform profile and vanishing net toroidal current (eq. 1.34), the vacuum-field magnetic well can be considered as a sufficient stability criterion according to the following relation

$$p'V'' - \int \int \frac{\mathbf{J}^2 \sqrt{g}}{|\nabla s|^2} d\theta d\varphi > 0, \quad (1.35)$$

which is a good approximation of the stability criterion [29]. Since the pressure usually decreases radially outward, $p' < 0$, and the integral is negative due to the negative sign in front of the positive definite integral, inequality (1.35) holds if $V'' < 0$, which is the definition of the vacuum-field magnetic well.

Particle Drifts are essential to understand the transport of particles and energy. Electrically charged particles gyrate in the presence of a magnetic field due to the Lorentz force. The corresponding gyromotion consists of a circular motion at constant speed around the guiding center perpendicular to the magnetic field \mathbf{B} . The corresponding gyrofrequency and Larmor radius

(gyroradius) are

$$\omega_c = \frac{|q|B}{m}, \quad (1.36)$$

$$\rho_L = \frac{v_\perp}{\omega_c}. \quad (1.37)$$

In the presence of an electric field \mathbf{E} , a drift of the particles emerges perpendicular to \mathbf{B} referred to as $\mathbf{E} \times \mathbf{B}$ -drift

$$\mathbf{v}_E = \frac{\mathbf{E} \times \mathbf{B}}{B^2}. \quad (1.38)$$

The drift is independent of the charge leading to the same motion for ions and electrons such that no current is produced. If B is nonuniform, e.g. bent to a torus, then two drifts emerge. Once a particle moves into a stronger magnetic field its Larmor radius reduces, eventually leading to a cycloid motion caused by the ∇B -drift

$$\mathbf{v}_{\nabla B} = \frac{mv_\perp^2}{2qB} \frac{\mathbf{B} \times \nabla B}{B^2}. \quad (1.39)$$

The curvature of the magnetic field \mathbf{B} leads to a drift velocity out of the magnetic surface against the centripetal force called the curvature-drift

$$\mathbf{v}_R = \frac{mv_\parallel^2}{qB} \frac{\mathbf{R}_c \times \mathbf{B}}{R_c^2 B^2}. \quad (1.40)$$

Here, \mathbf{R}_c is the radius of the corresponding magnetic field line curvature pointing outwards. Particle drifts are the reason why a plasma cannot be confined in a purely toroidal magnetic field and the rotational transform is, therefore, necessary for toroidal confinement.

Transport of energy from the center of the plasma to the wall is characterized by the confinement times τ_E which is desired to be large. In an optimal situation, the particle transport time to the wall is short and the kinetic energy of the particle is transferred to the plasma before it reaches the wall. This way, impurities can leave the plasma confinement quickly. Unfortunately, very fast particles such as fusion-produced α -particles tend to leave

the plasma without transferring their entire kinetic energy to the plasma. Thus, fast particles must transfer their kinetic energy to the background plasma so that the burning of the plasma can be sustained by fusion reactions. This process is characterized by the slowing-down time τ_s .

Classical Transport Theory assumes a random walk of the plasma particles in which the step size is the Larmor radius. The particles change their path due to Coulomb collisions and eventually leave the confinement volume. The rate of diffusion is given by $\nu_c \rho_L^2$, where ν_c is the collision frequency. Hence, classical transport is far too slow to be of concern.

Neoclassical Transport Theory follows the particles along their guiding center by averaging over the gyroradius and takes the magnetic field geometry into account. Except on isolated flux surfaces, three-dimensional magnetic fields lack an ignorable coordinate such that their nonuniformity strongly modifies the orbits of a class of trapped particles in form of radially outward drifts, leading to a transport much higher than predicted by classical transport theory. A derivation of the neoclassical transport model starts from the Vlasov equation and reduces the system by assuming a small Larmor radius and a large gyrofrequency. Collisions are taken into account. The corresponding system reduces to the Drift-Kinetic Equation (DKE) [31]

$$\frac{\partial f_\alpha}{\partial t} + \left(\mathbf{v}_\parallel \frac{\mathbf{B}}{B} + \mathbf{v}_D \right) \cdot \nabla f_\alpha = C_\alpha(f_\alpha), \quad (1.41)$$

where α is the corresponding particle species, f_α is the distribution function, \mathbf{v}_\parallel is the parallel velocity, \mathbf{v}_D is the drift velocity, and $C_\alpha(f_\alpha)$ is the collision operator. The Drift-Kinetic Equation Solver (DKES) solves a simplified version of eq. (1.41) by reducing the phase-space to only the toroidal angle φ , the poloidal angle θ and the pitch angle $\lambda = v_\parallel/v$. It only considers small deviations from the equilibrium distribution while the background equilibrium is assumed to be Maxwellian. The result is a linearized and radially local kinetic equation that is largely independent of $|\mathbf{v}|$. The solution to this equation leads to transport predictions that may be conventionally expressed in terms of mono-energetic transport coefficients. These describe the neoclassical transport with three dimensionless parameters, namely the

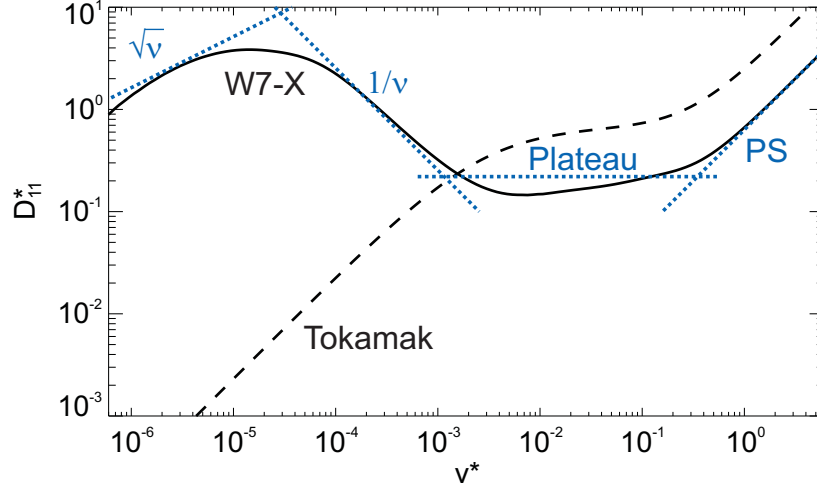


Figure 1.4.: The mono-energetic diffusion coefficient versus collisionality ν^* . The transport of the Wendelstein 7-X (W7-X) standard configuration (solid) is compared to a tokamak (dashed) with similar aspect ratio ($R_0/a = 5.527/0.255$) and an elongation of 1.5. The asymptotic transport regimes are the $\sqrt{\nu}$ -regime, the $1/\nu$ -regime, the plateau regime, and the Pfirsch–Schlüter regime. They are highlighted by dotted straight lines. The radial electric field has been chosen as $E_r/|\mathbf{v}|B = 3 \times 10^{-5}$, and the diffusivity has been normalized to the plateau value in a circular tokamak. Source [18].

toroidal magnetic flux ψ , the collisionality $\nu^* = \nu R_0/|\mathbf{v}|\iota$ and the normalized $\mathbf{E} \times \mathbf{B}$ drift velocity $v_E^* = E_r/|\mathbf{v}|B_0$, where B_0 is the magnetic field strength on the axis. The effective thermal transport coefficients used to describe the neoclassical transport are derived by an energy convolution of the corresponding mono-energetic transport coefficient with the local Maxwell distribution. This transport model depends on the collisionality regimes and the particle species. The collisionality regimes are visualized in figure 1.4. In the core, where the plasma is hot, the collisionality is low and the electrons are in the $1/\nu$ -regime described by the corresponding mono-energetic diffusion coefficient

$$D_e \sim \frac{\epsilon_{eff}^{3/2} v_D^2}{\nu_e}. \quad (1.42)$$

It thus scales as

$$D_e \propto \frac{\epsilon_{eff}^{3/2} T_e^{7/2}}{n_e B^2 R^2}, \quad (1.43)$$

which is highly temperature-dependent $D_e \propto T_e^{7/2}$. Applying the same diffusion coefficient to the ions leads to a much higher diffusion rate violating ambipolarity. Thus, their transport is reduced to the electron level by an arising inward-pointing (depends on signs of n' and T') radial electric field $E_r < 0$. The radial electric field shifts the ions into the even lower collisionality $\sqrt{\nu}$ -regime leading in total to the following diffusion coefficient

$$D_i \sim \frac{\sqrt{\nu} v_D^2}{\Omega_E^{3/2}}. \quad (1.44)$$

Here $\Omega_E \sim E_r/rB$ is the $\mathbf{E} \times \mathbf{B}$ poloidal precession frequency. The ambipolarity equation is highly nonlinear and may have multiple solutions. One is the "ion root" ($E_r < 0$) which is the scenario just described where the electrons are the rate-determining species [32], one is always unstable, and the "electron root" ($E_r > 0$) which is only realized when the electrons are much hotter than the ions.

Bootstrap Current is the terminology applied to the net parallel current flow per unit time arising in toroidal devices due to particle drifts perpendicular to the device's flux surfaces. It appears "naturally" from the solutions of the drift kinetic equation (eq. 1.41), but is entirely absent in a fluid (or MHD) description. The drift-kinetic formulation can be found in the equation for I_3 on page 3 of [32]. The bootstrap current is driven by all off-diagonal thermodynamic forces, i.e. density and temperature gradients as well as the radial electric field. Hence, a description of the bootstrap current lies beyond the scope of this thesis. An extensive description of the bootstrap current in a stellarator can be found in [32].

Turbulent Transport is believed to be the main driver of anomalous transport, a measured transport that cannot be explained with the classical or neoclassical model. Plasma turbulence is driven by micro-instabilities that

dynamically interact with the background field and take advantage of the free energy in the plasma available from the relaxation of density and temperature gradients [33]. These instabilities cause fluctuations to grow in the plasma, which is therefore not in a quiescent state, but the plasma remains in a state close to local thermodynamic equilibrium. Small fluctuations lead to charge separations that are amplified by the corresponding gradients and result in turbulent eddies. There exist a plethora of such instabilities which are generated by different gradients and geometric effects that interact with each other. The most common ones are Ion Temperature Gradient (ITG), Electron Temperature Gradient (ETG) and Trapped Electron Mode (TEM).

A tractable numerical model that is able to globally describe the turbulence of 3D equilibria proceeds from the six-dimensional Vlasov equation, but makes important simplifications. The assumptions that the microinstabilities are anisotropic, have low frequency compared to the gyrofrequency, and only involve small fluctuations is referred to as the gyrokinetic ordering and are used to simplify the equation. Gyrating particles are effectively replaced by charged rings which are subject to forces created by plasma inhomogeneities and electromagnetic fluctuations. The loss of the gyrophase information finally reduces the model to a five-dimensional gyrokinetic Vlasov equation. The current state of the Gyrokinetic Electromagnetic Numerical Experiment-3D (GENE-3D) [34] solves the collisionless gyrokinetic Vlasov equation profiting from allowed larger time steps and lower resolution requirements compared with those pertaining to the six-dimensional Vlasov equation.

GENE-3D is able to solve the gyrokinetic Vlasov equation linearly, so that the dominant instabilities (modes) can be studied. In nonlinear simulations, the modes interact with each other and exchange energy such that the time averages of the saturated state of the turbulence lead to particle and heat transport. Multiple particle species can be simulated. An investigation usually starts by assuming an adiabatic response for the electrons, i.e. neglecting electron inertia and can then subsequently be extended to kinetic electrons.

Confinement of Fast Particles is a necessary requirement in a future fusion reactor, since fast α -particles need to be confined long enough that their kinetic energy is transferred to the background plasma. This energy

is necessary to maintain the burn condition of the fusion reaction, in order that external heating is only necessary for start-up and plasma control. Losing trapped particles before they transfer their kinetic energy reduces the efficiency of the fusion reactor, but more importantly, they have the potential to damage vessel components, especially when these losses are concentrated in "hot spots". The confinement of fast particles, which needs to be comparable to the slowing down time τ_s , has to be considered separately from the rest of the transport since the kinetic energy of the particles is so high that they are not affected by the ambipolar radial electric field \mathbf{E}_r and can only be confined by the magnetic field \mathbf{B} alone. Axisymmetric magnetic fields adequately confine collisionless orbits, but in three-dimensional magnetic fields the situation is not as simple and it was long believed that any reflected particles will quickly leave the confinement region [35]. In so-called quasi-symmetric fields, the majority of the trapped particles are confined, but in other types of fields the deeply trapped particles are usually carried out of the plasma by the ∇B and curvature drifts. Such losses can be reduced by avoiding a stagnation point in the poloidal precession frequency of the particles advected by the ∇B -drift. This can be accomplished by establishing a minimum- B configuration, where

$$\frac{dB_{\min}}{dr} > 0, \quad (1.45)$$

holds over the confinement region. As $\dot{\theta} \propto \frac{\partial B}{\partial r}$, all trapped particles will precess in the same direction. The magnetic mirror is used as a tool to produce vacuum configurations where B_{\min} only slightly decreases radially outward such that the diamagnetic effects of finite- β equilibria can then transform the magnetic field into a minimum- B configuration.

1.2. Stellarator

The stellarator concept was invented by Lyman Spitzer in 1951 who realized that two fundamentally different ways exist to produce the rotational transform necessary for toroidal confinement [36]. Starting with a toroidal magnetic field, the tokamak produces the poloidal field component by an internal plasma current such that the magnetic field is axisymmetric and can thus be described in a two-dimensional poloidal plane. The stellarator,

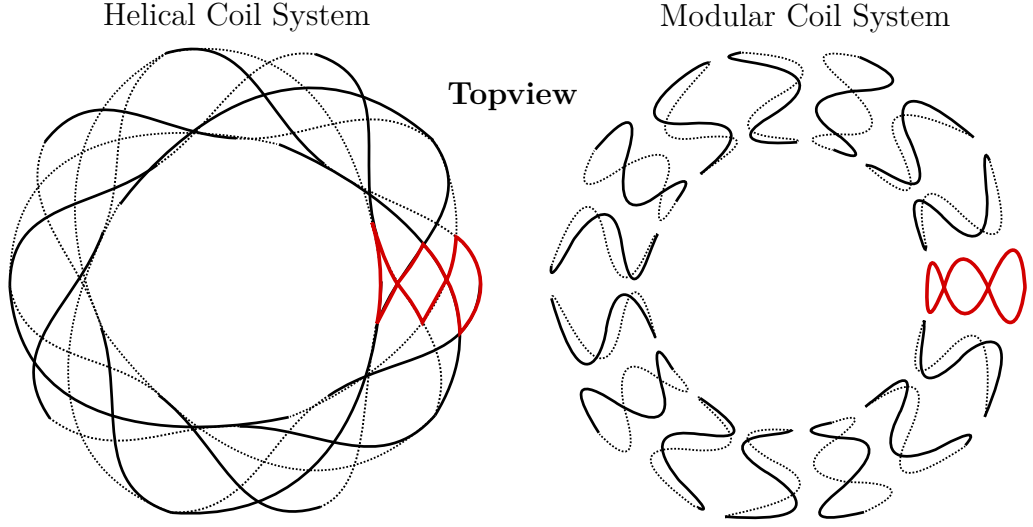


Figure 1.5.: The relation between classic and modular stellarator coil system. The helical coil system is compared with its modular version from the top.

on the other hand, uses three-dimensional shaping of the magnetic field and creates the poloidal field component solely by external currents. By design, the plasma boundary of a stellarator possesses a discrete symmetry in form of N_p identical field periods each being mirror symmetric. This introduces so-called *stellarator symmetry* defined in cylindrical coordinates as

$$\psi(R, \varphi, Z) = \psi(R, -\varphi, -Z). \quad (1.46)$$

A classical stellarator produces the toroidal and poloidal field components with two independent sets of magnetic field coils. The toroidal field coils are accompanied by a set of helically wound coils, which lie between the toroidal field coils and the plasma. The helical coils are arranged in pairs with current flowing in opposite direction in adjacent coils, so that the field cancels out at the magnetic axis but yields a twist of the field lines off-axis. The advantage of the classic design is the experimental flexibility achieved by being able to vary the toroidal and poloidal field components independently. Difficulties arise during the construction since the helical coils are interlocked and need to be wound 'in-situ'. Additionally, forces emerge between the toroidal and helical field coils, which increase with the magnetic field strength. In 1972,

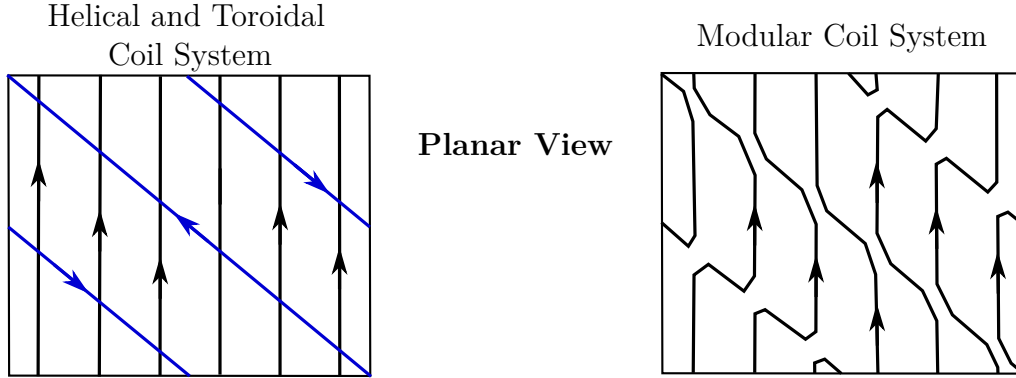


Figure 1.6.: The relation between classic and modular stellarator coil system. The helical coil system and the toroidal coil system are compared with its modular version in the 2-D representation.

the stellarator design of Wendelstein 7 (W7) was presented at a conference in Vienna [37], where exactly these forces were underestimated, leading to a redesign of the machine in form of a reduced minor radius and a name-change to Wendelstein 7-A (W7-A) [38]. Interestingly, during the same conference in 1972, Wobig and Rehker already presented the solution to the problem, a modular stellarator without helical windings [39] (Russian scientists had originally invented the modular coil system [40]). One coil system produces the whole magnetic field such that each coil is poloidally closed, nonplanar, can be manufactured separately, and, in theory, be replaced separately. The inhomogeneous forces on the coils that complicate the support structure are its only major disadvantage. The modular coil system was used to upgrade W7-A to Wendelstein 7-AS (W7-AS) [41] reaching the original machine parameters of W7. The connection between the classic and modular stellarator coil system is shown in figure 1.5 and figure 1.6.

The greatest advantage of the modular coil system is the possibility to think about the plasma and its properties first and then about the design of the corresponding coil configuration in a second step. Designing the equilibrium w.r.t. finite- β effects introduced the field of stellarator optimization, which led to the design of W7-AS being the first optimized stellarator.

1.3. Stellarator Optimization

Stellarator optimization is used to find an equilibrium that is most suitable for a future fusion reactor. The key requirements for such an equilibrium are MHD stability at high values of β , good energy confinement and a sufficient confinement of fast particles. All of these properties are described in more detail in section 1.1.3 and are referred to as finite- β effects or performance criteria throughout this thesis. Stellarator optimization essentially exploits the stellarator configuration space to find an equilibrium that complies best with the aforementioned requirements. The object of interest is the plasma boundary ∂M since it largely defines the magnetic field \mathbf{B} in its interior. Once the corresponding pressure p and current density \mathbf{J} are also known, an equilibrium is uniquely defined and its fitness w.r.t the performance criteria can be calculated. The magnetic field in turn defines the coil configuration, which can be derived using the boundary condition $\mathbf{B} \cdot \mathbf{n} = 0$ on ∂M . Here, \mathbf{n} is the corresponding normal on the plasma boundary.

The plasma boundary and the corresponding magnetic field are described by harmonic functions and the stellarator symmetry simplifies the description. During the design of W7-AS, Dommaschk potentials [42] were used that facilitated the design of the coil system by extending the magnetic field into the outer domain. The optimization principle was demonstrated in W7-AS, a configuration where the parallel current density was reduced which led to good equilibrium properties including a reduced Shafranov shift and improved stability properties [43].

The emerging technology of mainframe computers facilitated the design process of new optimized stellarator concepts and allowed the optimization targets to be extended and ultimately led to the design of W7-X, the first fully optimized stellarator. During the design process, the plasma boundary is described by a Fourier representation in cylindrical coordinates

$$R(u, v) = \sum_{m,n} r_{m,n} \cos(2\pi(mu + nv)), \quad (1.47)$$

$$Z(u, v) = \sum_{m,n} z_{m,n} \sin(2\pi(mu + nv)), \quad (1.48)$$

$$\varphi(v) = 2\pi v/N_p, \quad (1.49)$$

yielding a natural discretization in form of Fourier harmonics. Here u, v are poloidal and toroidal coordinates, each ranging from 0 to 1 in one period of

the machine. From this representation, coils can be easily computed on a surface outside the plasma boundary with the NESCOIL [44] algorithm.

The discovery of stellarator configurations that are quasi-helically symmetric (QH) in 1986 [45] was a breakthrough in stellarator optimization due to its capability of drastically reducing the neoclassical transport. The concept was first realized in the Helical Symmetric Experiment (HSX) in Wisconsin, which went into operation in 1999 [46]. The bootstrap current, which generally occurs in toroidal devices, is a source of free energy in the plasma that facilitates instabilities. Thus, its minimization was the main target after a form of quasi-symmetry could be obtained. The bootstrap current is negative in QH configurations and positive in quasi-axisymmetric (QA) configurations [47], but in absolute values, the bootstrap current was reduced in QH configurations compared to QA configurations. A further reduction was obtained by introducing linked mirror configurations, which in some sense combine aspects of QH and QA configurations [48]. The reduction of the bootstrap current aligned the drift surfaces with the magnetic surfaces and was later referred to as quasi-isodynamicity [49]. In this type of configuration, the contours of constant magnetic field B close poloidally and not toroidally. Similarly to quasi-symmetry, it is impossible to achieve exact quasi-isodynamicity in the whole confinement domain [50]. W7-X is essentially a quasi-isodynamic (QI) stellarator. Its optimization targets were later summarized in the W7-X objectives:

1. Good quality of the vacuum magnetic field in form of nested magnetic flux surfaces. The design omits low-order values of the rotational transform and avoids stochastic regions due to their poor confinement properties.
2. Good equilibrium properties including a small Shafranov shift. The plasma configuration essentially remains close to the optimized vacuum configuration when a plasma pressure is applied.
3. Good MHD stability properties up to an average plasma- β value of 5%.
4. Small neoclassical transport in the $1/\nu$ -regime leading to good energy confinement properties.

5. Small bootstrap current that, besides the isodynamic properties, reduces the availability of free energy in the plasma.
6. Good α -particle confinement at reactor relevant regimes of $\langle\beta\rangle = 5\%$.
7. Good modular coil feasibility that facilitates the manufacturing and assembly process.

The project W7-X began officially with a design study that was presented in 1988 at the IAEA conference in Nice [23], in which the name "Wendelstein VII-X" appeared for the first time. The 'X' was originally used as a placeholder without ever being replaced. In this study, many configurations were presented as a candidate for a possible follow-on of the W7-AS experiment, including the newly developed QH and QI concepts. A QI configuration was eventually chosen, since its reduced bootstrap current made the configuration similar to W7-AS and one intended to use synergistic effects. The disadvantage of the design of W7-AS was its initial lack of experimental flexibility caused by the modular coil system. An increased flexibility could later be established, which influenced the design process of W7-X and lead to an extended configuration space [51]. The primary coil system, consisting only of nonplanar coils, was extended by a secondary coil system in the form of planar coils. The final design possesses 5 different nonplanar and 2 different planar coil types. The original W7-X plasma boundary was slightly changed and named the 'High-Mirror' configuration. The ability to set different currents for each coil type led to a total of 9 canonical magnetic configurations where the rotational transform, the magnetic mirror, the magnetic shear and the position of the magnetic field was varied. Since its first introduction in [51], the W7-X configuration space changed multiple times to comply with the evolving requirements of the support structure and the port designs. This last step of the design process is similar to the first design step since the performance criteria are again optimized, but now the coil configuration is modified to comply with the updated geometric constraints. Consequently, the 'High-mirror' configuration available in the as-built design of W7-X has no target magnetic field and is different from the original W7-X plasma boundary, which is best described in [52].

1.4. Stellarator Coil Optimization

Stellarator coil optimization is the second step in the design process of a stellarator, after an optimal plasma boundary ∂M has been found that uniquely describes the target magnetic field \mathbf{B} . Deriving external currents on a surface outside the plasma boundary W that produce the given target magnetic field is an ill-posed inverse problem, which can be described as a 3D Neumann boundary value problem [53] requiring $\mathbf{B} \cdot \mathbf{n} = 0$ on ∂M . Here,

$$\mathbf{B} = \mathbf{B}_v + \mathbf{B}_p \quad (1.50)$$

is the superposition of the vacuum magnetic field \mathbf{B}_v and the magnetic field produced by internal plasma currents \mathbf{B}_p , and \mathbf{n} is the normal on the plasma boundary. The boundary condition can be translated into the following minimization problem

$$\min \int_{\partial M} (B \cdot n)^2 dS, \quad (1.51)$$

which aims to find an optimal current distribution on a "winding" surface W surrounding the plasma. Historically, this problem was first solved by extending the target magnetic field into the vacuum region in such a way that the external field can be represented by a superposition of harmonic functions [42]. This technique was used to design the coil configuration of W7-AS, the first modular stellarator. In general, coil optimization is based on the following theorem:

"Any harmonic vector field can be written in terms of its boundary values on a surface"[53].

The minimization problem (eq. 1.51) can be approached directly when the target magnetic field produced by the current distribution is described by the Biot-Savart formula

$$\mathbf{B}(\mathbf{r}) = \frac{\mu_0}{4\pi} \int_V \mathbf{J}_W \times \frac{\mathbf{r} - \mathbf{r}'}{|\mathbf{r} - \mathbf{r}'|^3} dV, \quad (1.52)$$

and the surface current \mathbf{J}_W on the winding surface is expressed by a current potential Φ :

$$\mathbf{J}_W = \mathbf{n} \times \nabla \Phi. \quad (1.53)$$

The NESCOIL code [44] describes Φ by a finite set of Fourier harmonics and after differentiating eq. (1.51) it solves the corresponding least squares problem. The result is a continuous and smooth current distribution on the winding surface W , which, in the absence of local minima of Φ , can be discretized into a finite set of poloidally closed filaments when a vanishing net toroidal current is assumed. NESCOIL was used to design the coil system of W7-X and its method was later extended by REGCOIL [54], which uses an additional regularization constraint on the current distribution to produce more practical coils in the sense that their average curvature is reduced.

Once a starting coil configuration in the Euclidean space is given, its shape and approximation of the target magnetic field can be further improved using nonlinear coil optimization as done with code suites such as optimization of heterogeneous magnet systems (ONSET) [55], COILOPT [56], COILOPT⁺⁺ [57] and Flexible Optimized Coils Using Space curves (FOCUS) [58]. They translate the original problem, “Approximation of a given magnetic field with a finite set of constructable coils”, into the minimization of a nonlinear objective function f

$$\min_{x \in X} f(x). \quad (1.54)$$

The structure of the objective function is visualized in figure 1.7. The input to the objective function f is a set of parameters $x \in X \subset \mathbb{R}^n$ describing the coil set in the parameter space X . The output is the penalty value $y \in \mathbb{R}$ describing the fitness of the configuration based on several quality criteria. Using the stellarator symmetry (eq. 1.46), one can reduce the full coil configuration to its unique building block, which is a half-module in W7-X, i.e. 1/10 of the torus. This reduction of the parameter space is extensively used by ONSET. FOCUS, on the other hand, uses the full coil configuration and consequently minimizes in the full parameter space.

The objective function f consists of a parametrization h that unfolds the coil configuration to a filament representation in Euclidean space from which the penalty function g calculates its fitness. The penalty function g computes the magnetic field \mathbf{B} produced by the coils and subsequently calculates the quality criteria $\{q_i(x)\}_{i=1,\dots,k}$ that measure the differences between the magnetic field produced by the coils and the target magnetic field defined by the plasma boundary. Additionally, geometric properties that describe the shape of the coil set are included. The last part in the

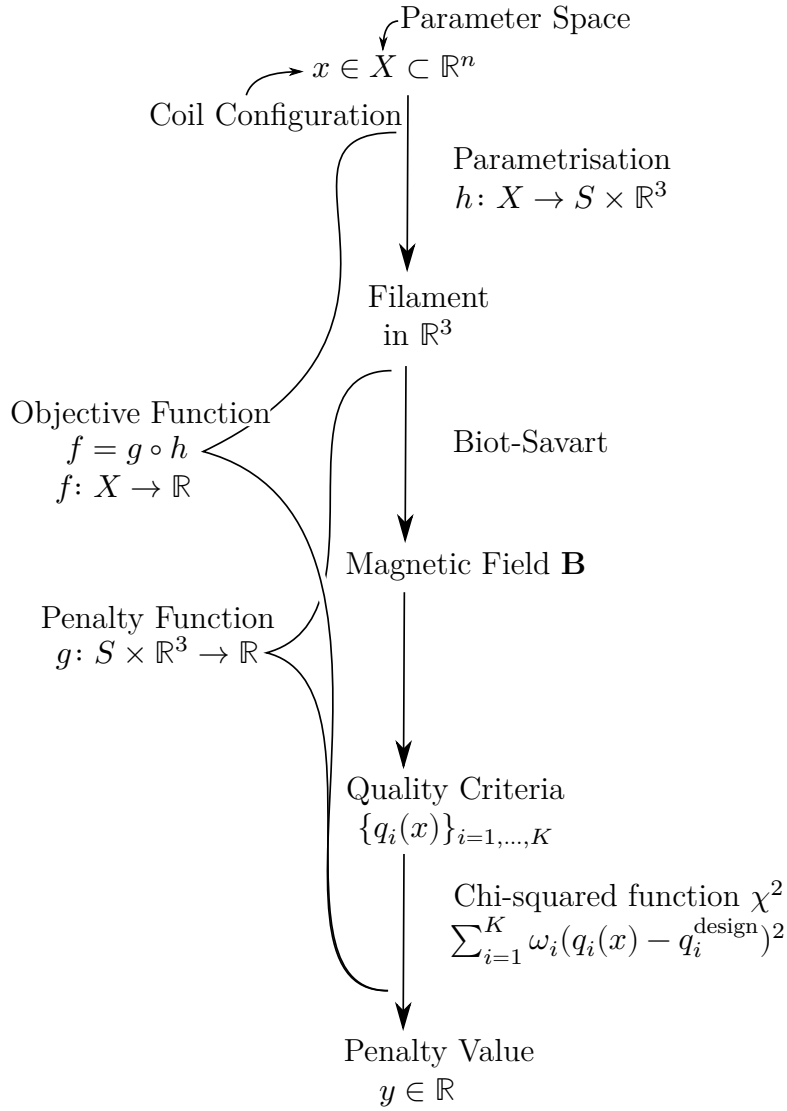


Figure 1.7.: The structure of the objective function f is visualized. It consists of the parametrization h and the penalty function g .

calculation of the penalty function is the $\chi^2(x)$ function that summarizes all the information in the following form

$$\chi^2(x) = \sum_{i=1}^k \omega_i \cdot \left(q_i(x) - q_i^{\text{design}} \right)^2. \quad (1.55)$$

The value of the quality criterion $q_i(x)$ is subtracted by its design value q_i^{design} (obtained from the target magnet field) and yields, factorized by its weight constant ω_i , the specific contribution to the penalty function.

The coil design process consists of a design sequence which describes the focus of each optimization run in form of weight constants $\{\omega_i\}_{i=1\dots k}$ and thresholds. In other words, the weight constants are constant within each optimization but may change throughout the design process, essentially defining the design sequence. The design sequence is divided into phases in which general aspects of the coil optimization problem are targeted. The coil design process is structured in such a way that the result of the previous optimization is used as a new starting coil configuration of the next optimization.

A specific order exists in which one ought to apply the quality criteria. This hierarchy is defined by their dominance and their effect on the parameter space. The most dominant quality criterion is the field error. FOCUS concentrates on the average squared error (eq. 1.51) while ONSET quantifies it with two different values, the maximum local field error

$$\max q_{le}(x) = \max \frac{|\mathbf{B} \cdot \mathbf{n}|}{|\mathbf{B}|}, \quad (1.56)$$

and the average global field error

$$q_{ae}(x) = \frac{\int_A q_{le} dA}{A}, \quad (1.57)$$

where A is the area of the plasma boundary. The hierarchy means that one is still able to optimize the other quality criteria, once the field error arrives at an acceptable value.

The filament structure of the coil configuration unfolded in 3D Euclidean space needs to comply with certain geometric properties that guarantee possible construction of the stellarator. The material that is used for the coils

in combination with the design current of the machine defines the lateral width of the coils, which in turn defines the required clearance between adjacent coils. The clearance must always be larger than the lateral width and needs to include the deformation during usage. There is a minimum distance between the coils and the plasma that needs to be met since the coils have to be sufficiently shielded from fusion-produced neutrons and a blanket has to be present in which tritium can be bred. This can be achieved by a constraint on the coil-to-plasma separation or by defining two limiting surfaces, which guarantee that the coils do not get too close or too far away from the plasma boundary. The material used for the coils, additionally, defines current density and thus the maximal allowed coil curvature. It is defined as

$$\kappa = \frac{1}{r_c}, \quad (1.58)$$

where r_c is the radius of the smallest circle defined by 3 points of two consecutive coil segments. In addition to the maximal curvature, unnecessary undulations need to be avoided, which is enforced by a second measure of curvature in ONSET. It is a weighted integral of κ over the coil length L

$$K = \frac{1}{2\pi} \int_0^L c(\kappa) \kappa(s) \, ds. \quad (1.59)$$

The curvature weight c is defined as

$$c(\kappa) = \begin{cases} \frac{\kappa - \kappa_{\min}}{\kappa_{\max} - \kappa_{\min}} & \kappa \geq \kappa_{\min} \\ 0 & \text{otherwise} \end{cases}. \quad (1.60)$$

It is desired to keep the weighted curvature of the coil as small as possible. In the design process documented in **Article I & III** the parameters κ_{\max} and κ_{\min} were set to the following values

$$\kappa_{\max} = 4/3 \, \text{m}^{-1} \quad (1.61)$$

$$\kappa_{\min} = 1/3 \, \text{m}^{-1}. \quad (1.62)$$

The weighted curvature was originally described in [59]. All of these geometric properties can simultaneously be targeted when penalizing the length of

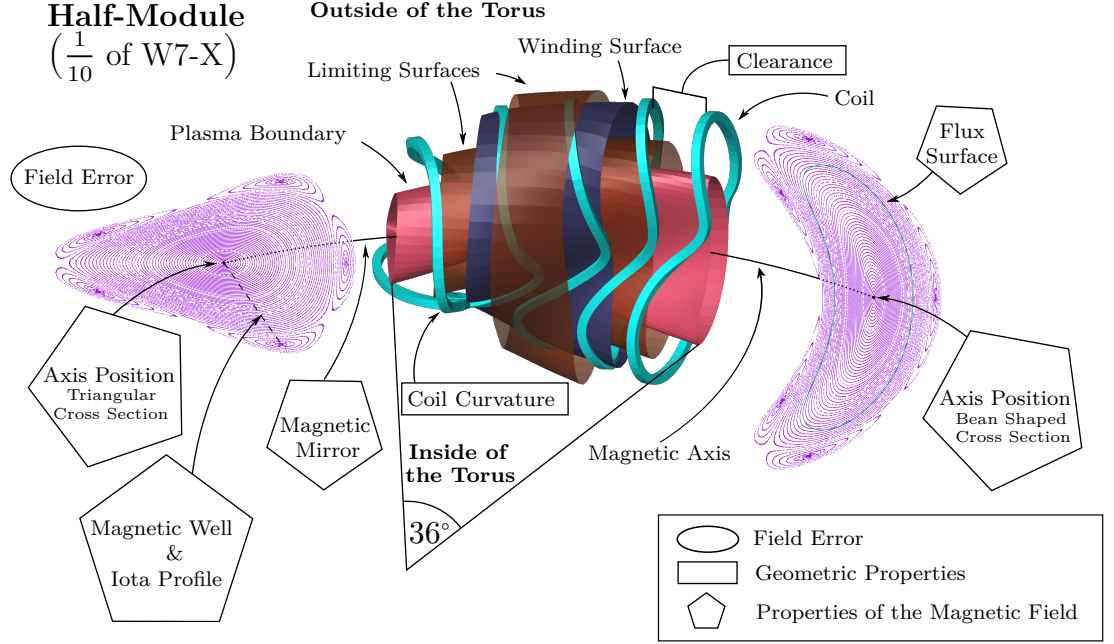


Figure 1.8.: The half-module of W7-X is visualized with the quality criteria.

the coil L . It is a geometric constraint that is simple to implement, but not as effective as the use of the individual geometric constraints (see **Article III**).

After the field error is reduced to an acceptable level and the coil configuration meets the geometric restrictions, properties of the vacuum magnetic field can be optimized. They are necessary for the performance of the magnetic field and facilitate a further field error reduction. The properties of the magnetic field are described in section 1.1.2 and can be calculated by following magnetic field lines allowing the existence and shape of the magnetic flux surfaces to be determined. The calculation in ONSET uses a magnetic field that is reduced to one half-module. The beginning of the half-module is sometimes referred to as the *bean-shaped cross section* and the end as the *triangular cross section* (see figure 1.8). The magnetic field properties are characterized by seven quality criteria used during the design process of **Article I & III**:

- The field line map has a fixed point at the inner limit of the nested magnetic flux surface called the *magnetic axis*. The position at the

beginning and at the end of the half-module of the magnetic axis are evaluated.

- The difference between the magnetic field strength B on the axis at the beginning and at the end of the half-module is referred to as the *magnetic mirror*

$$m = \frac{B_{\text{begin}} - B_{\text{end}}}{B_{\text{begin}} + B_{\text{end}}}. \quad (1.63)$$

The magnetic mirror is important for the confinement of fast particles.

- The value of the *rotational transform* ι on the axis is derived by following the magnetic axis over one half-period.
- The ι value on the axis together with a second ι value off axis allows an approximation of the *magnetic shear* to be derived.
- The *magnetic well* is defined in terms of how quickly the volume enclosed by the magnetic field increases with radius. Similarly to the magnetic mirror, the magnetic well is computed as the difference between two distinct volume increases evaluated in radial direction. The magnetic well is indicative of global MHD stability [17].
- Apart from the field error that quantifies the alignment of the surfaces, the latter can be characterized in Fourier space by computing the Fourier coefficients of inner flux surfaces. They are optimized towards the coefficients of the corresponding surfaces of the target magnetic field. The derivation in ONSET uses PEST coordinates [12].

During the design process, the objective function f is minimized by an optimizer that uses derivative information of f . The studies in **Article I & III** use Brent's PRinxipal AXIS method [60] in ONSET, which approximates the Hessian of f in an iterative process and optimizes along its principal axes. FOCUS uses analytically derived derivatives of its objective function, and in **Article III** we employed the conjugate gradient method to minimize the objective function.

1.5. Construction of Stellarators

The challenges in construction of stellarators lie primarily in the manufacturing of the coils and the assembly of the central coil system. The magnetic field defined by the coil system is the crucial part of a stellarator because it largely defines its performance. During construction, coil shape and position errors occur that can be either systematic or stochastic. What we mean by systematic errors are errors that are equal for the same construction process such that they are equal for the coils of the same type during the manufacturing and are equal for the assembly of the same half-module and module. Stochastic errors do not follow a predictable pattern. They break stellarator symmetry, since they are unique for the corresponding part of the coil system. Depending on the construction step, systematic errors either maintain or break stellarator symmetry. During the manufacturing process, systematic errors maintain stellarator symmetry whereas they can break it during the assembly process. The construction of W7-X was dominated by systematic errors in the manufacturing process and by stochastic errors in the assembly process [61]. The construction tolerances for the individual parts of the coil system are deduced by analyzing the individual effect of the displacement on the allowed magnetic field error which in turn is deduced from a perturbation analysis after the final coil system has been designed. Construction tolerances define the precision requirements during the manufacturing process and the engineering requirements during the assembly. Dividing the average allowed displacement per coil by the average coil diameter yields the *relative construction tolerance*.

1.5.1. Construction of Wendelstein 7-X

W7-X is a magnetic fusion experiment at the Greifswald site of the Max-Planck Institute for Plasma Physics (IPP) in Germany. It is the largest stellarator in the world (by major radius) and was put successfully into operation in 2015 with a remarkable confirmation of its magnetic field topology [62]. W7-X aims to investigate major physics and engineering issues for future fusion power plants, including 30 min continuous plasma discharges at 10 MW of heating power. It is equipped with superconducting coils allowing for steady-state operation. W7-X is a QI stellarator (see section 1.3) with a five period symmetry and an aspect ratio R_0/r_0 of 10.

The construction of W7-X required relative coil tolerances between 0.1% - 0.17% [61]. These strict tolerances led to precision requirements necessary for the construction of the central coil system that were a major challenge and affected both cost and schedule negatively, as stated in [63]: “The assembly process which took about 1 000 000 man-hours up to March 2014, was essentially dominated by the high demands on tolerances for the position of the superconducting coils”.

1.5.2. Construction of NCSX

The National Compact Stellarator Experiment (NCSX) [64] is a compact stellarator experiment designed by the Princeton Plasma Physics Laboratory (PPPL) in New Jersey, USA. It is a QA device (see section 1.3) with a three-period symmetry and a low aspect ratio of 4.4. Its plasma boundary was designed with STELLOPT [65] and the corresponding magnetic field was produced by 18 modular nonplanar coils designed with COILOPT [56]. Both design steps used massively parallel computers. NCSX was difficult to build and required tight manufacturing and assembly tolerances leading to relative constructions tolerances of around 0.08%. The associated difficulty and risk “was recognized but under-appreciated at the project outset”. [66] The construction, which began in 2003, could not meet the required tolerances. Fixes were worked out but the project repeatedly exceeded its budget and time limits, which eventually resulted in the cancellation of the whole project on May 22nd 2008 [67].

1.5.3. Construction of CNT

The Columbia Non-neutral Torus (CNT) is a plasma experiment that began operation in 2004 and concentrated on the investigation of non-neutral plasmas confined on magnetic surfaces. It is unique in its simple design consisting of only four circular coils: two interlocked coils inside the vacuum chamber and a pair of Helmholtz coils outside. CNT has an aspect ratio of 1.9, the lowest of any stellarator ever built. During the design of CNT, a Monte-Carlo type perturbation analysis was performed to determine the coil currents and the angle between the interlocked coils [68]. It is essentially a simpler version of stochastic stellarator coil optimization described in section 1.6. Instead of selecting the configuration with the largest magnetic volume,

the configuration most resilient to coil displacements and current variations was chosen. This led to an increase of the relative coil tolerances to values between 0.5% and 1%. [69], i.e. about an order of magnitude higher than W7-X and NCSX. This allowed a swift and inexpensive construction where several discrepancies could be accepted. The coil displacements were later confirmed [70] together with the robustness of the magnetic surfaces [71]. This proves that the chosen configuration was indeed robust against coil manufacturing and installation errors. The Hessian approach that determined the error fields of CNT [72] as well confirmed the resilience.

1.5.4. Final Remarks

During the construction, deviations of the central coil system in form of coil shape or position errors cannot be avoided. They can only be reduced which is highly complicated and thus expensive and time consuming. A reliable method that increases construction tolerances without compromising the performance of the magnetic field would be highly beneficial.

1.6. Stochastic Stellarator Coil Optimization

Stochastic stellarator coil optimization uses random numbers to model uncertainties that are absent in traditional deterministic coil optimization. These uncertainties describe deviations during the construction that are unknown at the time of the design process. The procedure is wrapped around the deterministic version of coil optimization (see figure 1.7) and begins with the generation of pseudo-random numbers [73] with a Gaussian distribution. A normal distribution is chosen to model the deviations in a way naturally occurring during subsequent construction. The random numbers are used to change the input parameters $x \in X$ of the objective function f that describe the coil set in the parameter space X . In order to reduce the computational cost, the optimization in ONSET concentrates on the coils of one half-module. The Monte-Carlo type perturbation of the parameters $x \in X$ then leads to coil displacements that are stellarator symmetric. The coil displacements in Euclidean space include changes of the shape and position of the coil configuration such that the stochastic approach covers systematic errors in the coil manufacturing process. The perturbation process creates

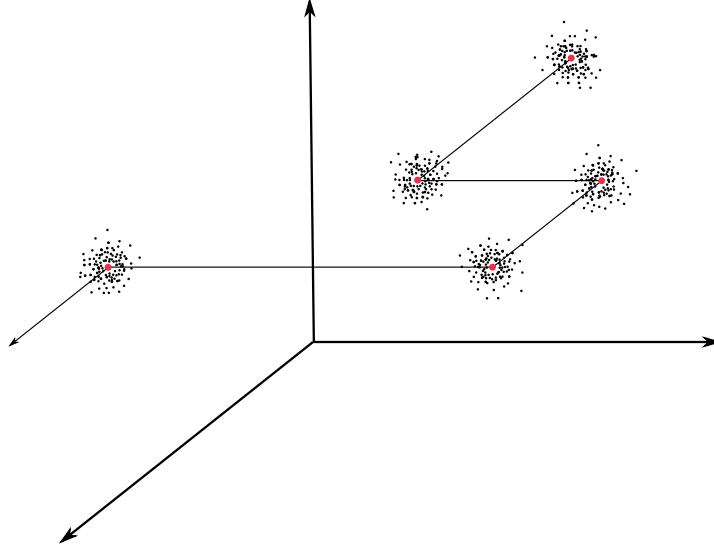


Figure 1.9.: Schematic drawing of the sample cloud moving through the parameter space X during the optimization. The red dots are the unperturbed coil configuration and each cloud is an independent evaluation of $F_{N_s}(x)$.

N_s samples that can be described as a sample cloud $\{\xi_i(x)\}_{i=0,\dots,N_s}$ covering an n -dimensional region of the parameter space around the unperturbed configuration $x \in X$ (see figure 1.9). It holds for $i \in \{0, \dots, N_s\}$

$$\xi_i(x) = x + \epsilon_i \quad \text{with} \quad |\epsilon_i| \ll |x|. \quad (1.64)$$

Subsequently, each element of the sample cloud is analyzed by the objective function f yielding N_s penalty values. The average of the set of penalty values $\{f(\xi_i(x))\}_{i=0,\dots,N_s}$ defines the fitness of the coil configuration in the stochastic sense by taking information about the vicinity of the coil set in the parameter space into account. This risk-averse objective function yields the penalty value $y \in \mathbb{R}$ and ends the stochastic part of the optimization. The described optimization loop visualized in figure 1.10 arrives at the optimizer, which uses the information of the penalty value to chose the next point in parameter space such that the optimization loop can start over.

The sample cloud $\{\xi_i(x)\}_{i=0,\dots,N_s}$ is characterized by the number of samples N_s , their distribution around the unperturbed configuration, and

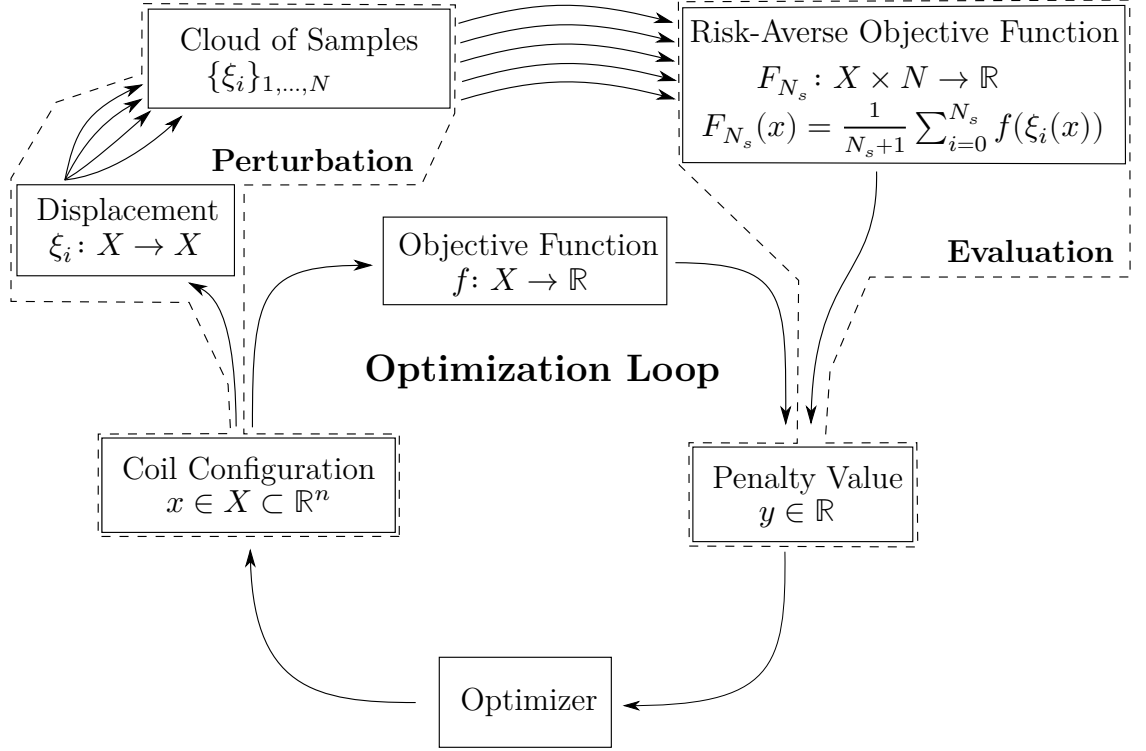


Figure 1.10.: The optimization loop of coil optimization is visualized which highlights the differences between the classic deterministic optimization and the newly introduced stochastic non-deterministic approach.

the extent of the cloud. The latter is quantified by the average perturbation amplitude

$$\mathcal{R} = \frac{1}{N_s} \frac{1}{N_{fp}} \cdot \sum_{i=1}^{N_s} \sum_{j=1}^{N_f} \overline{p_{ij} p_{ij}^u}, \quad (1.65)$$

where $\overline{p_{ij} p_{ij}^u}$ is the distance between the perturbed p_{ij} and unperturbed p_{ij}^u filament point. The sum is taken over all the filament points N_f that describe the coil set, and over all the coil sets in the cloud except the unperturbed one.

Stochastic coil optimization shifts the optimization of a single coil configuration (see eq. 1.54) to the optimization of a cloud of coil configurations

$$\min_{x \in X} F_{N_s}(x), \quad (1.66)$$

with

$$F_{N_s}(x) := \frac{1}{N_s + 1} \sum_{i=0}^{N_s} f_i(x) = \frac{1}{N_s + 1} \sum_{i=0}^{N_s} f(\xi_i(x)). \quad (1.67)$$

For a given coil configuration $x \in X$ the value $F_{N_s}(x)$ is the sample average of $f(x)$ which is an unbiased and consistent estimator [74] of the expected value

$$\mathbb{E}(f(x)) := \int_X d(u) f(x - u) du = [f * d](x). \quad (1.68)$$

The integral is taken over the whole parameter space X such that the perturbation function ξ is replaced by a density function $d : X \rightarrow [0, 1]$. In our case, it is the n -dimensional Gaussian distribution around the point $x \in X$. The expected value $\mathbb{E}(f(x))$ yields the average fitness of the coil configuration when every possible perturbation is considered and is essentially the convolution of the objective function with the chosen density function.

A coil configuration is more robust than a reference configuration, when under perturbation the quality of its magnetic field decreases less on average than the quality of the magnetic field of the reference configuration. The robustness is investigated by a perturbation analysis. The quality of the corresponding magnetic field is measured by the quality criteria leading to the penalty value $y \in \mathbb{R}$ describing the fitness of the coil configuration. The penalty value distribution obtained by multiple perturbations yields the robustness information of the coil configuration w.r.t. f in terms of its height and width.

The stochastic optimization model (eq. 1.67) optimizes the objective function f on average without having a direct penalty on the robustness of the outcome. This is achieved by a weight ω_σ that is multiplied with the standard deviation σ of the distribution, and added to the objective function $F_{N_s}(x)$

$$F_{N_s, \sigma}(x) := \frac{1}{N_s + 1} \sum_{i=0}^{N_s} f_i(x) + \omega_\sigma \sigma. \quad (1.69)$$

The penalty on the standard deviation that targets the width of the penalty distribution is a tool of risk-averse programming that aims to optimize worst-case scenarios.

Summary of Articles

We tested the stochastic stellarator coil optimization approach in **Article I & III** following a compact design sequence for the original W7-X plasma boundary. The design sequence concentrates on three general targets:

- Field Error,
- Geometric Properties,
- Properties of the Magnetic Field.

The main difference between the design sequence in **Article I & III** are the phases which divide the aforementioned targets and define their order. Coil configurations that were optimized stochastically differ by the

- number of samples N ,
- average perturbation amplitude \mathcal{T} ,
- degree of coil displacement used during the perturbations.

The degree of coil displacement describes the structure of the manifold on which the displacements occur and its corresponding dimension. We differentiate between

- two-dimensional displacements of the coils along the winding surface,
- first stage of three-dimensional displacements, where additionally the winding surface is perturbed,

- extended three-dimensional perturbation, where each coil is independently interpolated between the two limiting surfaces.

All perturbations preserve the five-period symmetry of the magnetic field defined by the original W7-X plasma boundary. The results of the stochastic coil optimization are compared to the single sample version of ONSET and FOCUS. Their average perturbation amplitude is essentially 0 mm and the optimization is deterministic. All optimizations with the deterministic or non-deterministic version of ONSET agree on the same starting coil configuration and use Brent’s principal axis method to minimize their individual objective function. The optimizations with FOCUS started with circular coils and its objective function was minimized by the conjugate gradient method.

In **Article II** we used the coil configurations optimized in **Article I** and extended the investigation of their fitness. We computed their magnetic fields and derived $\langle\beta\rangle = 5\%$ equilibria with VMEC [20], in which the density and temperature profiles are in agreement with the results of the latest experimental campaign of the W7-X experiment (OP1.2a and OP1.2b [75–77]). Then, we analyzed their fitness w.r.t. to the performance criteria (W7-X objectives, see section 1.3) that originally led to the shape of the target magnetic field used during the optimization process. Additionally, we analyzed the gyrokinetic behavior of a subset of three cases.

2.1. Article I: Stellarator coil optimization towards higher engineering tolerances

The first stochastic stellarator coil design study used two-dimensional perturbations, where each coil was independently displaced along the winding surface. The perturbations of the coil configuration used an average perturbation amplitude of approximately 2 mm. The test included six different sample sizes $N = 1, 100, 1000, 2000, 4000, 8000$. The case with one sample reduces to the deterministic stellarator coil optimization case called the *reference case*. We refer to the rest as *stochastic case N*. The design sequence used in this study divides the general targets into two phases. The 1st phase concentrates on the field error while simultaneously implementing the geometric properties. The 2nd phase focuses on the properties of the vacuum

magnetic field.

We evaluated the fitness of the coil configurations after the first optimization run, where the majority of the penalty value is reduced. We then concluded the design process and analyzed their final robustness w.r.t. the objective function f in a perturbation analysis that perturbed the coil configurations 100 000 times with the same technique and average perturbation amplitude as used during the optimization. The results are presented in form of penalty value histograms that are extended by the fitness of the unperturbed coil configuration in form of a straight line. To capture the change in robustness when the average perturbation amplitude is increased, we measured the change of the histograms with four percentiles that correspond to the 90%, 95%, 98% and 99% confidence interval.

The coil design study in **Article I** demonstrated the advantage of stochastic stellarator coil optimization compared to the classic deterministic coil optimization. Following the same design sequence, we could increase the performance of the design process by lowering the penalty value by 20% while simultaneously increasing the robustness w.r.t. the objective function f . The new optimization technique found differently shaped minima with higher peaks and smaller widths that showed better performance at an average perturbation amplitude of 2 mm and beyond. Comparing the behavior of the stochastic case 8000 directly to the reference case at the 99% confidence interval, we could relax the average perturbation amplitude by more than a factor of two for the same risk taken. The same comparison yields nearly a factor of three at the 90% confidence interval. We point out that the increased robustness w.r.t. the objective function f was obtained without a penalty on the penalty value distribution, e.g. on the standard deviation, only by using stochastic optimization. The technique of stochastic optimization changes the parameter space, which has a beneficial effect when the sample size is large. The optimization space is smoothed, which prevents the optimizer from getting stuck in local minima. The stochastic optimization loses the ability to capture the general structure of the original optimization space $f(X)$ when the sample size is low. This means that the parameter space of the stochastic optimization $F_{N_S}(X)$ is flattened out too much, which halts the optimization process.

2.2. Article II: Physics analysis of results of stochastic and classic stellarator coil optimization

During conventional coil design, the fitness of the coil configurations is set by the objective function f that measures it by means of chosen quality criteria. They quantify the difference between the target magnetic field and the magnetic field produced by the coil configuration, and additionally restrict the shape of the coil configuration in such a way that it is feasible for a subsequent construction. Hence, the quality of the underlying magnetic field is only measured w.r.t the target magnetic field. The actual fitness of the underlying magnetic field is unknown during the coil design process. Therefore, we changed the perspective in **Article II** and analyzed the fitness of magnetic fields produced by the coil configurations optimized in **Article I**, by means of the performance criteria that led to the shape of the original W7-X plasma boundary. The results are ranked by the target magnetic field. The magnetic fields are used to calculate $\langle\beta\rangle = 5\%$ equilibria with VMEC [20]. The $\langle\beta\rangle = 5\%$ equilibrium is one of the design goals of W7-X and a reactor-relevant regime. The analysis of the W7-X objectives includes an investigation of the Shafranov shift, global MHD stability, neoclassical transport and confinement of fast particles. We extended this list by an investigation of gyrokinetic behavior.

All candidates have quite good agreement on the values of the quality criteria used during the optimization. This guarantees that they are all valid approximations of the target magnetic field. The performance difference between the stochastic case 8000 and the reference case remains when analyzing the finite- β effects of the two magnetic fields. Hence, the situation is well captured by the penalty function. We found a surprisingly good performance of the stochastic cases $N = 100, 1000$, which have a higher penalty value than the reference case. Especially the fitness of the stochastic case 100 is not well represented by its large penalty value. We conclude that stochastic coil optimization outperforms deterministic coil optimization irrespectively of the number of samples ($N \geq 100$). The investigation shows that the penalty function does not represent the physics performance of the optimum perfectly and that better proxies for MHD stability are necessary. The investigation of gyrokinetic behavior showed no significant difference

between the stochastic case 8000, the reference case and the target magnetic field, suggesting that the differences in the magnetic field are too small to capture any turbulent transport differences.

2.3. Article III: Improved performance of stellarator coil design optimization

We extended the first stochastic stellarator coil design study (**Article I**) by switching to three-dimensional perturbations, increasing the number of samples N to 20 000, and using a risk-averse penalty on the standard deviation. We additionally changed the focus of the design sequence to concentrate on each general target separately by dividing it into three phases. The 1st phase solely concentrates on the reduction of the field error, the 2nd phase aims to fix the geometric properties of the coil configuration, while the 3rd phase focuses on optimizing the properties of the vacuum magnetic field. We chose three candidates with varying average perturbation amplitude: 0 mm, 2 mm, and 5 mm. The case with 0 mm again reduces to the deterministic coil optimization case called the *reference case* *ONSET*. With the aim to put our results into a broader perspective, an additional *reference case* *HYBRID* uses the FOCUS suite to reduce the field error in phase I and concludes the design phase II and III with the deterministic version of *ONSET*.

The stochastic cases use the simple three-dimensional perturbation in phase I and II, which compared to the deviation technique used in **Article I** additionally perturbs the winding surface. Unfortunately, it was not possible to fix the geometric properties of the reference case in phase II. The geometric penalties used in *ONSET* were not able to rectify the kink in one of the coils. All other cases concluded the design process. In phase III, the parametrization of the stochastic cases is changed in such a way that each coil is individually interpolated between the two limiting surfaces. This change of parametrization increases the three-dimensional flexibility of the coil configuration and makes a comparison with the coil flexibility in *FOCUS* possible. The reference case *HYBRID* uses the extended three-dimensional parametrisation throughout phase II and III.

The investigation concentrated on the development of the field error

throughout the three phases of the design sequence. A direct comparison to the results of the coil optimization study in **Article I** shows a significant reduction of the field error. This is caused by the increase of the number of samples, the additional perturbation of the winding surface, and most importantly by omitting the geometric constraints in the first phase of the design sequence. Similarly to the robustness increase in the previous study (**Article I**), where no penalty on the penalty value distribution was used, stochastic coil optimization reduces the maximal and average coil curvature when no geometric constraints are present in the penalty function. In this situation, the stochastic approach prevents the optimizer from getting stuck in local, non-optimal, minima in contrast to the situation of the reference case ONSET. Hence, geometric constraints are necessary to avoid local minima, but if chosen too tight, they can just as well halt the optimization. The final fitness of the coil configurations could be significantly increased with the stochastic version of ONSET, which is closely followed by the fitness of the reference case HYBRID. In the final perturbation analysis the number of samples is increased to $N = 200\,000$ and the extended three-dimensional displacement is used while the average perturbation amplitude is kept again fixed at 2 mm. The stochastic coil optimization showed, similarly to the first study (**Article I**), an increased robustness compared to the reference case HYBRID. The robustness increase is caused partly by the risk-averse tool and the stochastic technique itself. The comparison with FOCUS demonstrated the advantage of optimizing with derivatives while the comparison between the two stochastic cases showed that fewer evaluations are necessary to converge to a minimum when the average perturbation amplitude is higher.

Near Term Objectives

A natural way to extent the investigation of stochastic stellarator coil optimization is to refine the various aspects of the optimization procedure while applying it to new state-of-the-art optimization problems. Emerging coil optimization problems are a new quasi-axisymmetric configuration [78] that has the potential in becoming the predecessor to the ASDEX Upgrade (AUG) project at IPP Garching, and the present stellarator DEMOnstration power plant (DEMO) design developed by M. Drevlak at IPP Greifswald. The refinement should concentrate on the three main aspects used in the stochastic stellarator coil optimization loop (see figure 1.10):

- Perturbation,
- Evaluation,
- Optimizer.

Additionally, one can improve the objective function f of deterministic coil optimization (in particular the quality criteria) and refine the mathematical description of this special type of stochastic optimization.

The perturbation of the coil configuration is the crucial element of stochastic stellarator coil optimization, since by defining the variations of the coil configuration it dictates what the latter is optimized for. A shift of the perturbation from parameter space to Euclidean space allows the coil shape and coil position uncertainties be optimized separately. By extending the perturbations to half-modules and modules, including perturbations that

break the symmetry of the device, one is able to model the whole construction process of a stellarator. The question if one can optimize for stellarator asymmetric perturbations is unanswered, but highly desired, since they were the dominant errors during the assembly of W7-X [61]. Ultimately, different random number generators should be tested, e.g. Quasi-Monte Carlo. They have the potential to better cover the vicinity of the coil configuration in the sense that clustering, which naturally occurs in pure random distributions, can be diminished. Also a change of the distribution function should be tested to better understand their effect on the minimization process and the subsequent perturbation analysis.

The evaluation of the penalty values of the sample cloud $\{f_i(x)\}_{i=0,\dots,N_s}$ summarizes the information into a single penalty value $y \in \mathbb{R}$. For a given coil set $x \in X$ the evaluation can be refined by switching from an Arithmetic Mean (AM) applied to the sample cloud $\{f_i(x)\}_{i=0,\dots,N_s}$ during the optimizations in **Article I & III** to a Geometric Mean (GM)

$$\bar{f} = \left(\prod_{i=0}^{N_s} f_i \right)^{\frac{1}{N_s}}, \quad (3.1)$$

or to a Harmonic Mean (HM)

$$\bar{f} = N_s \left(\sum_{i=0}^{N_s} \frac{1}{f_i} \right)^{-1}. \quad (3.2)$$

They are related via the following inequality

$$\text{AM} \geq \text{GM} \geq \text{HM}, \quad (3.3)$$

and the GM and HM concentrate more on the lower part of the distribution function. This may have an effect on the final robustness of the configuration and the performance of the optimization. Fitting functions to the penalty value distributions can lead to a deeper understanding of the various forms of robustness and could lead to a better distinction between coils optimized stochastically or deterministically. Risk-averse programming was already used in **Article III**, but the method used penalized the standard deviation,

which includes a penalty on the worse performing as well as the better performing coil configurations. In the future, different segments of the penalty value distribution should be constrained with the aim to increase the final robustness of the coil configurations w.r.t. the objective function f .

The optimizer used during the stochastic optimization study is Brent’s PRincipal AXIS method called PRAXIS [60]. It uses the given points in the parameter space to approximate the Hessian of the objective function and optimizes along its principal axes. Optimization without derivatives needs in general many more function evaluations to converge compared to optimizations with derivative information (see **Article III**). The penalty values of the sample cloud $\{f_i(x)\}_{i=0,\dots,N_s}$ can additionally be used to derive derivative information of the objective function f that can be used to facilitate the optimization process.

Unfortunately, it is not possible to obtain analytic derivatives from the part of the objective function f that calculates properties of the magnetic field by field line tracing such that derivative-based optimizers cannot be used in ONSET. A possible solution are surrogate models that use a set of expensive function evaluations to model the objective function f . The surrogate framework directly quantifies the uncertainties and noise between its model and the image of the parameter space mapped by the objective function, and can direct the optimization into areas where the system needs to be improved. The surrogate model may yield derivative information and makes it less expensive to evaluate the objective function. The relative advantage of the surrogate model depends on its accuracy, which in turn depends on the number of points used to build it.

The objective function f used in coil optimization measures the difference between the magnetic field produced by the coil configuration and the target magnetic field, and additionally ensures certain geometric properties of the coil structure. General coil optimization can be refined by developing faster and more reliable proxies for the MHD stability and the confinement of fast particles as suggested in **Article II**.

New parametrizations from discrete differential geometry could lead to a discrete description (not based on Fourier harmonics) that relate the coil configuration more easily to the plasma boundary. The idea is to discretize

the underlying differential equations such that, instead of describing the magnetic field with smooth curves and surfaces, one would use polygons, meshes and simplicial complexes. The discrete points are then chosen in a specific way yielding an exact solution of the discrete difference equations which mimic properties of the governing differential equations, but with less computational cost.

The mathematical formulation of stochastic stellarator coil optimization was briefly introduced in section 1.6. From the minimization of the analytic description of the expected value (eq. 1.68) one should be able to extract a penalty of the curvature as well as a penalty on the standard deviation. Both constraints were found numerically in the finite version of stochastic stellarator coil optimization, documented in the studies in **Article I & III**.

3.1. Stochastic Version of FOCUS

The FOCUS suite [58] was used in **Article III** to optimize coils for the original plasma boundary of W7-X. The results were compared to the results of ONSET [55] and its stochastic version [79]. Its speed measured by the number of function evaluations was significantly higher than both versions of ONSET, whereas its final coil configuration was slightly worse than the final coil configuration of the stochastic version of ONSET. Applying stochastic optimization to the coil optimization process in FOCUS allows a direct comparison between the two stochastic coil optimization tools on the basis of fitness and robustness of the resulting coil configurations and might demonstrate once again that stochastic coil optimization gives better results than its deterministic counterpart [79].

The FOCUS suite considers the full coil set during the optimization so that perturbations that break the stellarator symmetry (eq. 1.46) can be studied. We mention again that the question if stellarators can be optimized to be robust against asymmetric errors is of great interest since the errors during the assembly of W7-X were mostly stochastic [61].

In FOCUS, the objective function is minimized using derivative information in the form of the Jacobian and Hessian of f . The corresponding eigenspectrum of the Hessian yields, together with the eigenvectors, the deformations of the coil configuration with the severest effect on its fitness.

A perturbation analysis that visualizes the development of these deformations gives information valuable for the optimizer such that the robustness can be targeted in more detail. The coils are parametrized using a Fourier description in FOCUS. The deformations obtained from the Hessian are consequently in the fourier space and not in the Euclidean space. A switch to a spline representation (used in ONSET) would yield robustness information that is more practical and can describe the construction tolerances more realistically.

3.2. Stochastic Stellarator Optimization

Article I & III showed that stochastic stellarator coil optimization increases the resilience of the coil configuration w.r.t. the objective function f . The objective function in turn measures the difference between the magnetic field produced by the coil configuration and the target magnetic field. Consequently, stochastic stellarator coil optimization can only achieve resilience w.r.t. to the approximation of the target magnetic field. When building a fusion reactor in form of a stellarator, one is interested in a resilience coil configuration w.r.t finite- β effects, so that deviations during the construction only inconsiderably affect the performance of the reactor. Therefore, it is natural to apply stochastic optimization directly to stellarator optimization as suggested in **Article II**. Unfortunately, the computational cost of the objective function in stellarator optimization is much higher than that for stellarator coil optimization due to the necessity of calculating MHD equilibria and target values. This situation requires a careful choice of the stellarator optimization problem and the corresponding design sequence. This includes an investigation of the hierarchy of performance criteria used during the optimization.

3.3. United Stochastic Stellarator and Coil Optimization

Once the stochastic approach is successfully tested in stellarator optimization in the sense that it reduces the computational time by using fewer function evaluations until the process converges, one is able to go one step

further and combine coil optimization with stellarator optimization. Thus, the equilibrium is designed by changing the coil configuration instead of the plasma boundary. This design process is already used in the 3rd step of the stellarator design process where the coil configuration is adjusted to design and engineering requirements that were unknown at the outset. The only difference is that the optimization starts at the beginning, but similarly eliminates the need for a plasma boundary that connects stellarator optimization with stellarator coil optimization. The advantage of this approach is that one only considers magnetic fields that can be realized by reasonable coils and that the quality of the magnetic field is measured directly by performance criteria.

Bibliography

- [1] H. A. (COORDINATION) et al. *BGR Energy Study 2018 – Data and Developments Concerning German and Global Energy Supplies*. Technical report 22. Data status 2017. Stilleweg 2, 30655 Hannover, Germany: The Federal Institute for Geoscience and Natural Resources (BGR) in Hanover, 2018.
- [2] D. J. MACKAY. *Sustainable Energy – without the hot air*. ISBN 978-0-9544529-3-3. Available free online from www.withouthotair.com. UIT Cambridge, 2008.
- [3] J. P. FREIDBERG. *Plasma Physics and Fusion Energy*. Cambridge University Press, 2007. DOI: 10.1017/CB09780511755705.
- [4] D. BÖCKENHOFF. *En Route Towards Heat Load Control for Wendelstein 7-X with Machine Learning Approaches*. PhD thesis. Universität Greifswald, 2020.
- [5] J. N. BAHCALL. »NEUTRINOS FROM THE SUN«. In: *Scientific American*, Vol. 221.1 (1969), pages 28–37. URL: <http://www.jstor.org/stable/24926407>.
- [6] J. D. LAWSON. »Some Criteria for a Power Producing Thermo-nuclear Reactor«. In: *Proceedings of the Physical Society. Section B*, Vol. 70.1 (Jan. 1957), pages 6–10. DOI: 10.1088/0370-1301/70/1/303.
- [7] F. CHEN. *Introduction to Plasma Physics and Controlled Fusion*. Introduction to Plasma Physics and Controlled Fusion Bd. 1. Springer, 1984. URL: <https://books.google.de/books?id=ToAtqznznr80C>.
- [8] L. TONKS and I. LANGMUIR. »Oscillations in Ionized Gases«. In: *Phys. Rev.*, Vol. 33 (2 Feb. 1929), pages 195–210. DOI: 10.1103/PhysRev.33.195.

- [9] K. NISHIKAWA, M. WAKATANI and M. WAKATANI. *Plasma Physics: Third Edition*. Springer Nature Book Archives Millennium. Springer, 2000. URL: <https://books.google.de/books?id=4cHkd77TSHcC>.
- [10] T. JARVIS and J. TANTON. »The Hairy Ball Theorem via Sperner's Lemma«. In: *The American Mathematical Monthly*, Vol. 111.7 (2004), pages 599–603. DOI: 10.1080/00029890.2004.11920120. eprint: <https://doi.org/10.1080/00029890.2004.11920120>.
- [11] P. HELANDER. »Theory of plasma confinement in non-axisymmetric magnetic fields«. In: *Reports on Progress in Physics*, Vol. 77.8 (July 2014), page 087001. DOI: 10.1088/0034-4885/77/8/087001.
- [12] R. C. GRIMM, J. M. GREENE and J. L. JOHNSON. »Computation of the Magnetohydrodynamic Spectrum in Axisymmetric Toroidal Confinement Systems«. In: *Controlled Fusion*. Edited by J. KILLEEN. Vol. 16. Methods in Computational Physics: Advances in Research and Applications. Elsevier, 1976, pages 253–280. DOI: <https://doi.org/10.1016/B978-0-12-460816-0.50012-9>.
- [13] A. H. BOOZER. »Plasma equilibrium with rational magnetic surfaces«. In: *The Physics of Fluids*, Vol. 24.11 (1981), pages 1999–2003. DOI: 10.1063/1.863297. eprint: <https://aip.scitation.org/doi/pdf/10.1063/1.863297>.
- [14] S. HAMADA. »Hydromagnetic equilibria and their proper coordinates«. In: *Nuclear Fusion*, Vol. 2.1-2 (Jan. 1962), pages 23–37. DOI: 10.1088/0029-5515/2/1-2/005.
- [15] J. P. FREIDBERG. *Ideal MHD*. Cambridge University Press, 2014. DOI: 10.1017/CB09780511795046.
- [16] B.B.KADOMTSEV. »Hydromagnetic stability of a plasma«. In: *Reviews of plasma physics*, Vol. 2 (1966), page 153.
- [17] I. B. BERNSTEIN et al. »An energy principle for hydromagnetic stability problems«. In: *Proceedings of the Royal Society of London. Series A. Mathematical and Physical Sciences*, Vol. 244.1236 (1958), pages 17–40. DOI: 10.1098/rspa.1958.0023. eprint: <https://royalsocietypublishing.org/doi/pdf/10.1098/rspa.1958.0023>.

-
- [18] P. HELANDER et al. »Stellarator and tokamak plasmas: a comparison«. In: *Plasma Physics and Controlled Fusion*, Vol. 54.12 (Nov. 2012), page 124009. DOI: 10.1088/0741-3335/54/12/124009.
- [19] D. A. GARREN and A. H. BOOZER. »Existence of quasihelically symmetric stellarators«. In: *Physics of Fluids B: Plasma Physics*, Vol. 3.10 (1991), pages 2822–2834. DOI: 10.1063/1.859916. eprint: <https://doi.org/10.1063/1.859916>.
- [20] S. P. HIRSHMAN and J. C. WHITSON. »Steepest-descent moment method for three-dimensional magnetohydrodynamic equilibria«. In: *The Physics of Fluids*, Vol. 26.12 (1983), pages 3553–3568. DOI: 10.1063/1.864116. eprint: <https://aip.scitation.org/doi/pdf/10.1063/1.864116>.
- [21] S. HIRSHMAN, W. VAN RIJ and P. MERKEL. »Three-dimensional free boundary calculations using a spectral Green’s function method«. In: *Computer Physics Communications*, Vol. 43.1 (1986), pages 143–155. DOI: [https://doi.org/10.1016/0010-4655\(86\)90058-5](https://doi.org/10.1016/0010-4655(86)90058-5).
- [22] H. YAMADA et al. »Characterization of energy confinement in net-current free plasmas using the extended International Stellarator Database«. In: *Nuclear Fusion*, Vol. 45.12 (Nov. 2005), pages 1684–1693. DOI: 10.1088/0029-5515/45/12/024.
- [23] G. GRIEGER, C. BEIDLER and E. HARMEYER. »Physics studies for helical-axis advanced stellarators«. In: *Plasma physics and controlled nuclear fusion research 1988*. 2. IAEA. Nizza, 1989, pages 369–387.
- [24] I. BERNSTEIN et al. »Energy Principle for Hydromagnetic Stability Problems«. In: *Proceedings of the Royal Society of London. Series A, Mathematical and Physical Sciences*, Vol. 244.1236 (1989), pages 17–40.
- [25] C. N. GEB. SCHWAB. *Numerische Verfahren zur Untersuchung der magnetohydrodynamischen Stabilität dreidimensionaler Plasmagleichgewichte*. PhD thesis. Technische Hochschule Darmstadt, 1991.
- [26] C. MERCIER. »Critère de Stabilité d’un Système toroidal Hydro-magnetique en Pression Scalaire«. In: *Plasma Physics and Controlled Fusion Research*. 2. IAEA. Wien: Nuclear Fusion, 1962, page 801.

- [27] A. H. GLASSER, J. M. GREENE and J. L. JOHNSON. »Resistive instabilities in general toroidal plasma configurations«. In: *The Physics of Fluids*, Vol. 18.7 (1975), pages 875–888. DOI: 10.1063/1.861224. eprint: <https://aip.scitation.org/doi/pdf/10.1063/1.861224>.
- [28] D. LORTZ. »Sufficient stability criteria for general MHD-equilibria«. In: *Nuclear Fusion*, Vol. 13.6 (Dec. 1973), pages 817–819. DOI: 10.1088/0029-5515/13/6/005.
- [29] J. NÜHRENBURG and R. ZILLE. »Equilibrium and stability of low-shear stellarators«. In: *Proceedings of Workshop on theory of fusion plasmas*. Edited by B. COMPOSITORI. EUR11336EN. 1987.
- [30] R. DUX. *Plasmaphysik und Fusionsforschung, Teil I: Plasmaphysik*. Universität Augsburg, 2001.
- [31] R. D. HAZELTINE. »Recursive derivation of drift-kinetic equation«. In: *Plasma Physics*, Vol. 15.1 (Jan. 1973), pages 77–80. DOI: 10.1088/0032-1028/15/1/009.
- [32] C. BEIDLER et al. »Benchmarking of the mono-energetic transport coefficients—results from the International Collaboration on Neoclassical Transport in Stellarators (ICNTS)«. In: *Nuclear Fusion*, Vol. 51.7 (June 2011), page 076001. DOI: 10.1088/0029-5515/51/7/076001.
- [33] *Turbulent Transport*. In: *Fusion Plasma Physics*. John Wiley and Sons, Ltd, 2013. Chapter 11, pages 293–322. DOI: 10.1002/9783527669516.ch11. eprint: <https://onlinelibrary.wiley.com/doi/pdf/10.1002/9783527669516.ch11>.
- [34] M. MAURICE. »The 3D global version of the gyrokinetic turbulence code GENE«. In: *Plasma Physics and Controlled Fusion Research*, (2019). submitted to Journal of Computational Physics.
- [35] W. LOTZ et al. »Collisionless alpha -particle confinement in stellarators«. In: *Plasma Physics and Controlled Fusion*, Vol. 34.6 (June 1992), pages 1037–1052. DOI: 10.1088/0741-3335/34/6/010.
- [36] L. SPITZER. »The Stellarator Concept«. In: *The Physics of Fluids*, Vol. 1.4 (1958), pages 253–264. DOI: 10.1063/1.1705883. eprint: <https://aip.scitation.org/doi/pdf/10.1063/1.1705883>.

-
- [37] M. BLAUMOSER et al. »Status and technical concept of the Garching stellarator Wendelstein VII«. In: *Proceedings of the 7th Symposium on Fusion Technology. Grenoble, France, (1972)*, pages 239–249.
- [38] M. BLAUMOSER et al. »Ohmic Heating in the W VII A-Stellarator«. In: *Eighth European conference on controlled fusion and plasma physics, Prag, Czechoslovakia, Vol. 2 (1977)*, pages 73–92.
- [39] H. WOBIG and S. REHKER. »A Stellarator coil system without helical windings«. In: *Proceedings of the 7th Symposium on Fusion Technology. Grenoble, France, (1972)*, pages 345–353.
- [40] M. IVANOVSKII, S. POPOV and A. POPRYADUKHIN. »Tor-2-Stellarator«. In: *P.N. Lebedev Physics Institute, Academy of Science of the USSR, Preprint No. 94 (1968)*, page 42.
- [41] F. RAU, J. KISSLINGER and H. WOBIG. »Vacuum Magnetic Field and Modular Coil System of the Advanced Stellarator Wendelstein VII-AS«. In: *IPP Report 2/259, (1982)*.
- [42] W. DOMMASCHK. »Solution to Stellarator Boundary Value Problems with a new Set of Simple Toroidal Harmonic Functions«. English. In: *Zeitschrift für Naturforschung - Section A Journal of Physical Sciences, Vol. 36.3 (1981)*. cited By 19, pages 251–260. DOI: 10.1515/zna-1981-0307.
- [43] M. HIRSCH et al. »Major results from the stellarator Wendelstein 7-AS«. In: *Plasma Physics and Controlled Fusion, Vol. 50.5 (Mar. 2008)*, page 053001. DOI: 10.1088/0741-3335/50/5/053001.
- [44] P. MERKEL. »Solution of stellarator boundary value problems with external currents«. In: *Nuclear Fusion, Vol. 27.5 (May 1987)*, pages 867–871. DOI: 10.1088/0029-5515/27/5/018.
- [45] J. NÜHRENBERG and R. ZILLE. »Quasi-helically symmetric toroidal stellarators«. In: *Physics Letters A, Vol. 129.2 (1988)*, pages 113–117. DOI: [https://doi.org/10.1016/0375-9601\(88\)90080-1](https://doi.org/10.1016/0375-9601(88)90080-1).
- [46] F. S. B. ANDERSON et al. »The Helically Symmetric Experiment, (HSX) Goals, Design and Status«. In: *Fusion Technology, Vol. 27.3T (1995)*, pages 273–277. DOI: 10.13182/FST95-A11947086. eprint: <https://doi.org/10.13182/FST95-A11947086>.

- [47] J. NÜHRENBURG, W. LOTZ and S. GORI. »Quasi-Axisymmetric Tokamaks«. In: *Theory of Fusion Plasmas*, (1994).
- [48] E. H. ET AL. »Modular stellarators with improved confinement«. In: *Controlled Fusion and Plasma Physics (Proc. 14th Eur. Conf. Madrid) Vol. 11D, Part I*, (1987), page 411.
- [49] S. GORI, W. LOTZ and J. NÜHRENBURG. »Theory of Fusion Plasmas«. In: *Proc. Workshop Varenna, 1996*, Vol. 335 (1997).
- [50] J. R. CARY and S. G. SHASHARINA. »Omnigenity and quasihelicity in helical plasma confinement systems«. In: *Physics of Plasmas*, Vol. 4.9 (1997), pages 3323–3333. DOI: 10.1063/1.872473. eprint: <https://doi.org/10.1063/1.872473>.
- [51] J. .KISSLINGER et al. »Magnetic Field and Coil Systems of the Modular Helias Configurations HS 5-10«. In: *Fusion Technology 1990*, Vol. 2. 1991, pages 1520–1524.
- [52] C. NÜHRENBURG. »Global ideal magnetohydrodynamic stability analysis for the configurational space of Wendelstein 7–X«. In: *Physics of Plasmas*, Vol. 3.6 (1996), pages 2401–2410. DOI: 10.1063/1.871924. eprint: <https://doi.org/10.1063/1.871924>.
- [53] E. MARTENSEN. »Über eine Methode zum räumlichen Neumannschen Problem mit einer Anwendung für torusartige Berandungen«. In: *Acta Mathematica*, Vol. 109 (1963), pages 75–135. DOI: <https://doi.org/10.1007/BF02391810>.
- [54] M. LANDREMAN. »An improved current potential method for fast computation of stellarator coil shapes«. In: *Nuclear Fusion*, Vol. 57.4 (Feb. 2017), page 046003. DOI: 10.1088/1741-4326/aa57d4.
- [55] M. DREVLAK. »Coil Designs for a Quasi-Axially Symmetric Stellarator«. In: *20th Symposium on Fusion Technology Mareseille France*, (1998), page 883.
- [56] D. J. STRICKLER, L. A. BERRY and S. P. HIRSHMAN. »Designing Coils for Compact Stellarators«. In: *Fusion Science and Technology*, Vol. 41.2 (2002), pages 107–115. DOI: 10.13182/FST02-A206. eprint: <https://doi.org/10.13182/FST02-A206>.

- [57] T. BROWN et al. »Engineering optimization of stellarator coils lead to improvements in device maintenance«. In: *2015 IEEE 26th Symposium on Fusion Engineering (SOFE)*. May 2015, pages 1–6. DOI: 10.1109/SOFE.2015.7482426.
- [58] C. ZHU et al. »New method to design stellarator coils without the winding surface«. In: *Nuclear Fusion*, Vol. 58.1 (Nov. 2017), page 016008. DOI: 10.1088/1741-4326/aa8e0a.
- [59] M. DREVLAK. »Automated Optimization of Stellarator Coils«. In: *Fusion Technology*, Vol. 33.2 (1998), pages 106–117. DOI: 10.13182/FST98-A21. eprint: <https://doi.org/10.13182/FST98-A21>.
- [60] K. R. GEGENFURTNER. »PRAXIS: Brent’s algorithm for function minimization«. In: *Behavior Research Methods, Instruments, & Computers*, Vol. 24 (1992), pages 560–564.
- [61] T. RUMMEL et al. »Accuracy of the construction of the superconducting coils for WENDELSTEIN 7-X«. In: *IEEE Transactions on Applied Superconductivity*, Vol. 14.2 (June 2004), pages 1394–1398. DOI: 10.1109/TASC.2004.830584.
- [62] T. PEDERSEN, M. OTTE and S. LAZERSON. »Confirmation of the topology of the Wendelstein 7-X magnetic field to better than 1:100,000«. In: *Nature Communication*, Vol. 7 (Nov. 2016), page 13493. DOI: 10.1038/ncomms13493.
- [63] H.-S. BOSCH et al. »Final integration, commissioning and start of the Wendelstein 7-X stellarator operation«. In: *Nuclear Fusion*, Vol. 57.11 (Aug. 2017), page 116015. DOI: 10.1088/1741-4326/aa7cbb.
- [64] A. REIMAN et al. »Physics design of a high-bbeta quasi-axisymmetric stellarator«. In: *Plasma Physics and Controlled Fusion*, Vol. 41.12B (Dec. 1999), B273–B283. DOI: 10.1088/0741-3335/41/12b/320.
- [65] D. A. SPONG et al. »J* optimization of small aspect ratio stellarator/tokamak hybrid devices«. In: *Physics of Plasmas*, Vol. 5.5 (1998), pages 1752–1758. DOI: 10.1063/1.872844. eprint: <https://doi.org/10.1063/1.872844>.

- [66] G. H. NEILSON et al. »Lessons Learned in Risk Management on NCSX«. In: *IEEE Transactions on Plasma Science*, Vol. 38.3 (Mar. 2010), pages 320–327. DOI: 10.1109/TPS.2009.2037889.
- [67] R.L. ORBACH. »Statement about the Future of the Princeton Plasma Physics Laboratory«. In: *Under Secretary for Science and Director, Office of Science, U.S. Department of Energy*, (May 2008).
- [68] J. P. KREMER. *The Creation and First Studies of Electron Plasmas in the Columbia Non-neutral Torus*. PhD thesis. Columbia University, 2006.
- [69] T. S. PEDERSEN et al. »Construction and Initial Operation of the Columbia Nonneutral Torus«. In: *Fusion Science and Technology*, Vol. 50.3 (2006), pages 372–381. DOI: 10.13182/FST06-A1258. eprint: <https://doi.org/10.13182/FST06-A1258>.
- [70] K. C. HAMMOND et al. »Experimental and numerical study of error fields in the CNT stellarator«. In: *Plasma Physics and Controlled Fusion*, Vol. 58.7 (May 2016), page 074002. DOI: 10.1088/0741-3335/58/7/074002.
- [71] T. S. PEDERSEN et al. »Experimental demonstration of a compact stellarator magnetic trap using four circular coils«. In: *Physics of Plasmas*, Vol. 13.1 (2006), page 012502. DOI: 10.1063/1.2149313. eprint: <https://doi.org/10.1063/1.2149313>.
- [72] C. ZHU et al. »Hessian matrix approach for determining error field sensitivity to coil deviations«. In: *Plasma Physics and Controlled Fusion*, Vol. 60.5 (Apr. 2018), page 054016. DOI: 10.1088/1361-6587/aab6cb.
- [73] M. MATSUMOTO and T. NISHIMURA. »Mersenne Twister: A 623-Dimensionally Equidistributed Uniform Pseudo-Random Number Generator«. In: *ACM Trans. Model. Comput. Simul.*, Vol. 8.1 (Jan. 1998), pages 3–30. DOI: 10.1145/272991.272995.
- [74] SHAPIRO, A. »Monte Carlo sampling approach to stochastic programming«. In: *ESAIM: Proc.*, Vol. 13 (2003), pages 65–73. DOI: 10.1051/proc:2003003.

- [75] T. S. PEDERSEN et al. »First results from divertor operation in Wendelstein 7-X«. In: *Plasma Physics and Controlled Fusion*, Vol. 61.1 (Nov. 2018), page 014035. DOI: 10.1088/1361-6587/aaec25.
- [76] R. C. WOLF et al. »Performance of Wendelstein 7-X stellarator plasmas during the first divertor operation phase«. In: *Physics of Plasmas*, Vol. 26.8 (2019), page 082504. DOI: 10.1063/1.5098761. eprint: <https://doi.org/10.1063/1.5098761>.
- [77] T. KLINGER et al. »Overview of first Wendelstein 7-X high-performance operation«. In: *Nuclear Fusion*, Vol. 59.11 (June 2019), page 112004. DOI: 10.1088/1741-4326/ab03a7.
- [78] S. HENNEBERG et al. »Properties of a new quasi-axisymmetric configuration«. In: *Nuclear Fusion*, Vol. 59.2 (Jan. 2019), page 026014. DOI: 10.1088/1741-4326/aaf604.
- [79] J.-F. LOBSIEN, M. DREVLAK and T. S. PEDERSEN. »Stellarator coil optimization towards higher engineering tolerances«. In: *Nuclear Fusion*, Vol. 58.10 (Aug. 2018), page 106013. DOI: 10.1088/1741-4326/aad431.
- [80] J.-F. LOBSIEN et al. »Physics analysis of results of stochastic and classic stellarator coil optimization«. In: *Nuclear Fusion*, Vol. 60.4 (Feb. 2020), page 046012. DOI: 10.1088/1741-4326/ab7211.
- [81] J.-F. LOBSIEN et al. »Improved performance of stellarator coil design optimization«. In: *Journal of Plasma Physics*, Vol. 86.2 (2020), page 815860202. DOI: 10.1017/S0022377820000227.

Acronyms

AM Arithmetic Mean

AUG ASDEX Upgrade

CAS3D Code for the Analysis of the
MHD Stability of 3D Equilibria

CNT Columbia Non-neutral Torus

DEMO DEMOnstration power plant

DKE Drift-Kinetic Equation

DKES Drift-Kinetic Equation Solver

ETG Electron Temperature Gradient

FOCUS Flexible Optimized Coils Us-
ing Space curves

GENE-3D Gyrokinetic Electromag-
netic Numerical Experiment-3D

GM Geometric Mean

HM Harmonic Mean

HSX Helical Symmetric Experiment

IPP the Max-Planck Institute for
Plasma Physics

ITG Ion Temperature Gradient

MHD magnetohydrodynamics

NCSX National Compact Stellarator
Experiment

ONSET optimizatiON of heterogen-
eouS magnET systems

PPPL Princeton Plasma Physics
Laporatory

QA quasi-axisymmetric

QH quasi-helically symmetric

QI quasi-isodynamic

TEM Trapped Electron Mode

VMEC variational moments equilib-
rium code

W7 Wendelstein 7

W7-A Wendelstein 7-A

W7-AS Wendelstein 7-AS

W7-X Wendelstein 7-X

List of Symbols

Symbol	Description	Unit
T_e	Electron temperature.	eV
T_i	Ion temperature.	eV
n_e	Electron density.	m^{-3}
n	Particle density, $n = N/V$.	m^{-3}
τ_E	Energy confinement time.	s
τ_s	Slowing-down time.	s
λ	Pitch angle.	
θ	Poloidal angle.	
φ	Toroidal angle.	
ϑ	Poloidal angle.	
q	Electric charge.	C
B_{\max}	Maximum magnetic field strength.	T = $\text{kg A}^{-1} \text{s}^{-2}$
B_{\min}	Minimum magnetic field strength.	T = $\text{kg A}^{-1} \text{s}^{-2}$
\mathbf{B}	Magnetic field.	T = $\text{kg A}^{-1} \text{s}^{-2}$
\mathbf{E}	Electric field.	$\text{kg m A}^{-1} \text{s}^{-3}$
\mathbf{J}_{\parallel}	Parallel electric current density.	A m^{-2}

List of Symbols

Symbol	Description	Unit
\mathbf{J}_\perp	Perpendicular electric current density.	A m^{-2}
\mathbf{J}	Electric current density.	A m^{-2}
E_r	Radial electric field strength.	$\text{kg m A}^{-1} \text{s}^{-3}$
\mathbf{E}_r	Radial electric field.	$\text{kg m A}^{-1} \text{s}^{-3}$
ϱ	Electric charge density.	A s m^{-3}
B	Magnetic field strength.	$\text{T} = \text{kg A}^{-1} \text{s}^{-2}$
p	Plasma pressure.	$\text{kg m}^{-1} \text{s}^{-2}$
μ_0	Vacuum permeability.	$\text{N}^2 \text{A}^{-1}$
ϵ_0	Vacuum permittivity.	F m^{-1}
W	Plasma thermal and magnetic energy.	$\text{J} = \text{kg m}^2 \text{s}^{-2}$
Ω_E	$\mathbf{E} \times \mathbf{B}$ poloidal precession frequency.	s^{-1}
ν^*	Collisionality.	s^{-1}
ν_c	Collision frequency.	s^{-1}
ω_c	Gyrofrequency.	s^{-1}
m	Mass.	g
D_e	Mono-energetic diffusion coefficient for electrons.	
D_i	Mono-energetic diffusion coefficient for ions.	
$C_\alpha(f_\alpha)$	Collision operator.	
q_{ae}	Average global field error.	
L	Length of the coil.	

Symbol	Description	Unit
c	Curvature weight.	
κ	Coil curvature.	
q_i^{design}	Design value.	
q_{le}	Local field error.	
q_i	Quality criterium.	
K	Weighted coil curvature.	
ω_i	Weight constant.	
m	Magnetic mirror.	
R_0	Major radius to the magnetic axis.	m
R_c	Radius of magnetic field line curvature.	m
R	Major radius.	m
A	Aspect ratio.	
ρ_L	Gyro (Lamor) radius.	m
χ	Poloidal magnetic flux.	Wb
r_0	Minor radius of the last closed flux surface.	m
ρ	Normalized minor radius.	
r	Minor radius.	m
s	Normalized toroidal flux.	
ψ	Toroidal magnetic flux.	Wb
A	Area of the plasma boundary.	
B_p	Magnetic field produced by internal plasma currents.	T
B_v	Vacuum magnetic field.	T
J_W	Current density on the plasma boundary.	A m ⁻²
Φ	Vector potential.	V

List of Symbols

Symbol	Description	Unit
∂M	Plasma boundary.	
W	Winding surface.	
\mathbf{n}	Normal vector on the plasma boundary.	
χ^2	Function that summarizes all the information.	
\mathbb{R}^n	N-dimensional Euclidean Space.	
N_p	Number of field periods.	
f	Objective function.	
X	Parameter space.	
h	Parametrisation.	
g	Penalty function.	
V	Plasma volume.	m^3
f_α	Distribution function.	
ι	Rotational transform.	
ς	Magnetic shear.	
β	Plasma beta.	
\mathbb{E}	Expected value.	
N_s	Number of samples.	
N_f	Number of filament points.	
f_i	Sample cloud.	
ξ_i	Sample.	
$F_{N_s, \sigma}$	Objective function of stochastic optimization with risk-averse penalty.	
F_{N_s}	Objective function of stochastic optimization.	
\mathbf{v}_D	Drift velocity.	m s^{-1}

Symbol	Description	Unit
v_E^*	Normalized $\mathbf{E} \times \mathbf{B}$ -drift velocity.	
\mathbf{v}_E	$\mathbf{E} \times \mathbf{B}$ -drift.	m s^{-1}
$\mathbf{v}_{\nabla B}$	∇B -drift.	m s^{-1}
\mathbf{v}_R	Curvature drift.	m s^{-1}
\mathbf{v}	Plasma flow velocity.	m s^{-1}

List of Figures

1.1. Cross sections of various nuclear reactions as a function of the center of mass energy of the two particles.	2
1.2. Field lines generating nested magnetic flux surfaces.	6
1.3. Charged particles in a magnetic field	11
1.4. Mono-energetic diffusion coefficient versus collisionality ν^* .	14
1.5. Relation between classic and modular stellarator coil system I	18
1.6. Relation between classic and modular stellarator coil system II	19
1.7. Structure of the objective function f	25
1.8. Half-module of W7-X	28
1.9. Picture of the sample cloud	33
1.10. Structure of stochastic stellarator coil optimization	34



Thesis Articles

Authors contributions:

Michael Drevlak wrote the ONSET suite [55]. The implementation of the stochastic framework into the ONSET suite was done by J.-F. Lobsien [79]. Caixiang Zhu wrote the FOCUS suite [58].

Article I

»Stellarator coil optimization towards higher engineering tolerances«

J.-F. LOBSIEN, M. DREVLAK and T. S. PEDERSEN

Nuclear Fusion, Vol. 58.10 (Aug. 2018)

The stellarator design sequence was developed by M. Drevlak and J.-F. Lobsien. The stellarator design study was done by J.-F. Lobsien. Key ideas concerning the evaluation of the results were developed by T. Sunn Pedersen and J.-F. Lobsien. J.-F. Lobsien wrote the manuscript. The work was edited by M. Drevlak and T. Sunn Pedersen.

Article II

»Physics analysis of results of stochastic and classic stellarator coil optimization«

J.-F. LOBSIEN et al.

Nuclear Fusion, Vol. 60.4 (Feb. 2020)

The equilibrium calculations were done by J.-F. Lobsien. The stability calculations with CAS3D were done by C. Nührenberg. The density and temperature profiles used in the neoclassical section were developed in collaboration with H.M. Smith and Y. Turkin. The neoclassical transport calculations with DKES were done by H.M. Smith.

The fast particle losses with ANTS were calculated by J.-F. Lobsien. The gyrokinetic calculations were done by M. Maurer in consultation with A.B. Navarro. M. Maurer wrote the gyrokinetic part of the manuscript which was edited by F. Jenko and J.-F. Lobsien. J.-F. Lobsien wrote the rest of the manuscript which was edited by M. Drevlak, C. Nührenberg, H.M. Smith, Y. Turkin and T. Sunn Pedersen.

Article III

»Improved performance of stellarator coil design optimization«

J.-F. LOBSIEN et al.

Journal of Plasma Physics, Vol. 86.2 (2020)

T. Kruger extended the FOCUS suite by the curvature penalty. The stellarator design study was done by J.-F. Lobsien. The scope of the manuscript was developed by J.-F. Lobsien, S. Lazerson and T. Sunn Pedersen. The manuscript was written by J.-F. Lobsien. The work was edited by M. Drevlak, T. Kruger, S. Lazerson, C. Zhu and T. Sunn Pedersen.

Confirmed by Supervisor,
Greifswald, 09.09.2020

PROF. DR. THOMAS SUNN PEDERSEN

Confirmed by doctoral candidate,

Greifswald, 09.09.2020

JIM-FELIX LOBSIEN

A.1. Article I

»Stellarator coil optimization towards higher engineering tolerances«

J.-F. LOBSIEN, M. DREVLAK and T. S. PEDERSEN

Nuclear Fusion, Vol. 58.10 (Aug. 2018)

Stellarator coil optimization towards higher engineering tolerances

Jim-Felix Lobsien

Max-Planck Institute for Plasma Physics, Greifswald, Germany

E-mail: `jim.lobsien@ipp.mpg.de`

Michael Drevlak

Max-Planck Institute for Plasma Physics, Greifswald, Germany

E-mail: `michael.drevlak@ipp.mpg.de`

Thomas Sunn Pedersen

Max-Planck Institute for Plasma Physics, Greifswald, Germany

E-mail: `thomas.sunn.pedersen@ipp.mpg.de`

W7-X Team

Abstract. Recently designed optimized stellarator experiments have suffered from very tight construction tolerances, but some level of deviation of the coil system is unavoidable during fabrication of the coils and assembly of the coil system. In this paper, we present a new approach that incorporates reduced sensitivity to construction tolerances of the coil system into the optimization sequence. The approach was tested within the framework of the existing coil optimization scheme for Wendelstein 7-X. The results are compared with those of a coil set obtained by the original optimization. The result is a more optimal coil system with less stringent tolerances, such that small deviations cause reduced deterioration of the properties important for fusion performance.

Keywords: Stellarator, Nonlinear Coil Optimization, Reduced Engineering Tolerances, Robust Magnetic Field, Stochastic Optimization

Submitted to: *Nucl. Fusion*

1. Introduction

Stellarators confine plasma in a 'magnetic cage', which is produced by a set of external coils. These coil systems need to be optimized to fit both the physics requirements of the

corresponding vacuum field and the engineering requirements of the coil structure. The accuracy of the constructed coil system is crucial for the performance of the stellarator and is a cost and schedule driver as exemplified below.

The Wendelstein 7-X (W7-X) project required relative coil tolerances (defined as the allowed tolerance divided by the average coil radius) between 0.1% - 0.17% [1]. These strict tolerances were kept, and the device was put successfully in operation with a remarkable precision of its magnetic field topology [2]. However, precision requirements for the magnets were a major challenge and affected both cost and schedule negatively, as stated in [3]: "The assembly process which took about 1 000 000 man-hours up to March 2014, was essentially dominated by the high demands on tolerances for the position of the superconducting coils". The construction of the National Compact Stellarator Experiment (NCSX), which started in 2003, required relative coil deviation tolerances of about 0.08%. The associated difficulty and risk "was recognized but underappreciated at the project outset" [4]. Unfortunately, "the budget increases, schedule delays and continuing uncertainties of the NCSX construction project necessitate its closure" [5] in 2008.

For the design of the Columbia Nonneutral Torus (CNT), whose design started around 2001, well after the coil designs of W7-X and NCSX had started, the issue of tight coil tolerances was addressed from the beginning of the coil design. A Monte-Carlo-type perturbation analysis was performed as an integral part of determining the coil currents and coil locations [6]. A configuration was chosen that exhibited large flux surfaces even in the presence of minor coil displacements, over others that nominally had larger confinement volumes but were much more sensitive to coil placement inaccuracies. The chosen configuration had assembly tolerances of 0.5% - 1% for deviations in coil location and orientation [7], ie. about an order of magnitude looser than W7-X and NCSX. The resilience against error fields allowed the acceptance of several discrepancies. The robustness of the volume of the magnetic surfaces was directly verified experimentally [8], and significant coil displacements were later confirmed with state-of-the-art metrology [9], proving that the device was not accurately built but rather that its design point indeed was robust against coil manufacturing and installation errors.

Those results were promising, and very important for the successful construction of CNT, but the optimization goals for CNT were simple: to maximize the volume of good flux surfaces for a stellarator with only four circular coils. It was until now not clear if the approach taken would be effective for the much more complicated and multi-faceted optimization goals for stellarators designed for fusion energy research, and for the much more complicated coils that result from state-of-the-art coil design codes. The approach itself, described in more detail in [6], is one that optimizes a cloud of coil sets in the near vicinity of a particular configuration that is being optimized. This configuration will be referred to as the leading configuration and is in the center of the multidimensional cloud of other configurations, a Monte-Carlo sample of the coil configurations that could be realized within the uncertainties associated with construction and assembly of an actual device. The average performance of this cloud of coil sets is ascribed to the

leading configuration. By sampling neighboring states in this way, a penalty is given to configurations whose performance could be well below that of the leading configuration. In particular, this sample average avoids that a search ends up in a narrow "peak" (if maximizing) or trough (if minimizing) which is then, due to the narrowness, not robust against errors in the range that is to be expected. This technique also effectively smoothens the optimization landscape, as illustrated for a toy model in Figure 1. In this case, the non-robust optimum for $x \approx 0.42$ vanishes and the most stable optimum emerges as the global optimum at $x \approx 0.3$ in both locally averaged parameter spaces. For the one using a broad Gaussian distribution, the function to be optimized is now very smooth, and it even has just one maximum. For the one using a narrower Gaussian, the smoothing is also evident, and the global maximum is the robust one, but several other local maxima are still present.

Toy Model of Parameter Spaces

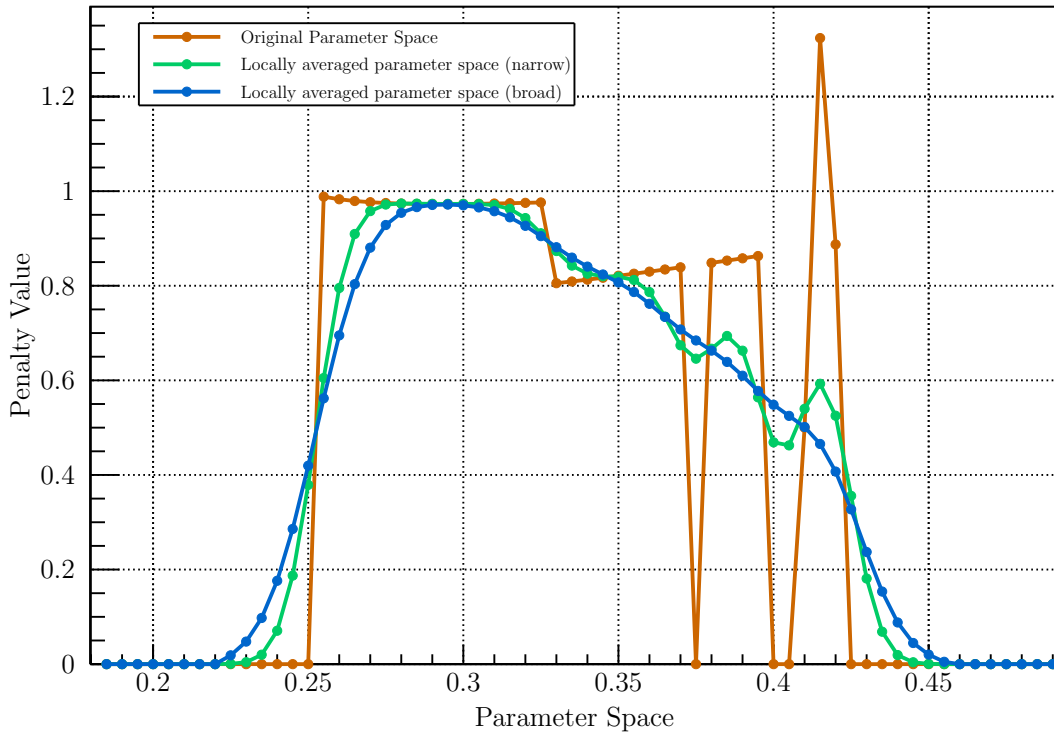


Figure 1: In stellarator optimization, the target function may be a non-smooth function of control parameters, and may exhibit a global maximum that is not robustly attainable since the control parameters (such as coil shapes) have finite tolerances. Taking the average of normal distributed samples in a small region of control parameters has a smoothing effect on the parameter space, and avoids getting stuck in non-robust optima. This is illustrated here for a toy model.

The approach presented in this paper follows the same philosophy but is applied for a much more fusion relevant problem addressed with state-of-the-art codes. Nonlinear coil optimization is expanded by an iterative perturbation analysis, which aims to

achieve higher engineering tolerances through the aforementioned technique. Instead of optimizing a single coil set, we optimize the sample average of $N + 1$ coil sets, where N is the number of additional samples. Its disadvantage, that $N + 1$ times more computational resources are needed, is partly offset by the highly efficient parallelization that is possible for this problem.

In Section 2, we transform the original optimization problem into a stochastic optimization problem. We then expand upon the sampling technique first performed for CNT, applying a more sophisticated version of it to a much more complicated optimization problem, namely that of W7-X. Since the original optimization sequence for the W7-X coil system is not available, a new coil optimization sequence was developed. Additionally, in order to achieve a high amount of experimental flexibility, the W7-X coil configuration was designed to produce multiple plasma configurations. The various features resulted in a compromise between different, at times conflicting, optimization targets. Consequently, the W7-X coil system does not correspond precisely to the original plasma boundary designed by J. Nührenberg [10] and hence, we do not use the present W7-X coil set as a reference case to validate how good our newly optimized coil sets are. Instead, we compare our results with a coil set that was found with our most recent standard optimization - one that only optimizes for a single coil set at a time without averaging over a cloud of perturbed coils. The test is described and analyzed in Section 3. We conclude in Section 4 and give an outlook on our future projects in Section 5. More details about the optimization sequence can be found in [Appendix A](#).

2. Stochastic Optimization Problem

In nonlinear coil optimization one starts with an initial coil configuration $x \in X \subset \mathbb{R}^n$, where n is the number of parameters describing the coil set, and tries to solve the optimization problem

$$\min_{x \in X} f(x) \tag{1}$$

with a nonlinear optimizer. The objective function $f : X \rightarrow \mathbb{R}$ yields the fitness of the corresponding coil set x and is the measure of optimization. It summarizes the differences of the quality criteria $q_i(x)$ and their design value q_i^{design} in a sum of squares:

$$f(x) = \sum_{i=1}^k \omega_i \left(q_i(x) - q_i^{design} \right)^2. \tag{2}$$

Here, the ω_i denote the weight constants. Since on the one hand the coil geometry and installation has a certain precision, and deviations within this precision in general are not predictable, and on the other hand our goal is to be able to relax precision requirements with minimal loss of plasma performance, the optimization problem is a stochastic one, with the following formulation:

$$\min_{x \in X} \{ F(x) := \mathbb{E}_{P_x}[f(\xi(x))] \} \quad \xi(x) = x + \epsilon \quad \text{with} \quad |\epsilon| \ll |x|. \tag{3}$$

The expectation is taken with respect to the probability distribution P_x of the random vector ξ . This includes random deviations of a manufactured and installed coil set from its as-designed geometry and placement. We therefore optimize for uncertainty of the deformation of the coil set during construction. The probability distribution P_x carries the information of the likelihood of any possible geometric deviation of each particular coil set $x \in X$. P_x is assumed to follow a normal distribution.

We follow the approach taken in [11] and use a Monte Carlo sampling approach to approximate the expected value $\mathbb{E}_{P_x}[f(\xi(x))]$. Let $\xi^1(x), \dots, \xi^N(x)$ be i.i.d. (independently and identically distributed) samples generated by the n -dimensional normal distribution $\mathcal{N}(x, \Sigma)$. Here, the mean of the normal distribution is our initial coil configuration $x \in X$ and the standard deviation is equal in every dimension and chosen appropriately to obtain the desired deviation in the euclidean space. Then by the Law of Large Numbers, for a given $x \in X$, we have

$$F_N(x) := (N + 1)^{-1} \sum_{i=0}^N f(\xi^i(x)) \longrightarrow \mathbb{E}_{P_x}[f(\xi(x))], \text{ for } N \rightarrow \infty \quad (4)$$

almost surely, where $\xi^0(x) := x$ is the unperturbed coil set (leading configuration). The sample average F_N is an unbiased and consistent estimator of $F(x) = \mathbb{E}_{P_x}[f(\xi(x))]$. The convergence in probability is of order $O_p(N^{-\frac{1}{2}})$, implying that a ten-fold increase in accuracy of the estimate of the expectation requires a 100-fold increase in sample size.

3. Results

We test our stochastic optimization technique using a newly developed coil optimization sequence for the W7-X plasma boundary [12]. The sequence consists of six optimization runs (cf. Table A1) such that the previous optimization run is used as a new starting point. The initial coil set is computed with NESCOIL [13] on a winding surface (WS) located 45 cm beyond the outer plasma surface. The objective function f , which assigns a penalty value to every coil set, is calculated by ONSET [14]. The evaluation criteria used in ONSET are shown in Table A1. A coil is defined by 12 periodic spline points and raised to 13 spline points in optimization run 4. Each spline point is defined by a poloidal angle u and a toroidal angle v . The 5-fold symmetry of W7-X combined with the stellarator symmetry reduces the primary coil set to 5 different coils. The WS is interpolated with 13 parameters between two limiting surfaces and since the auxiliary coils are not being considered we arrive at $n = 133$ or rather $n = 143$ parameters in total. We have chosen Brent's PRincipal AXIS algorithm [15] for the nonlinear optimization without using derivatives.

We modified the objective function from calculating the penalty value $f(x)$ of a single coil set $x \in X$ to generating a cloud of coil sets $\xi^1(x), \dots, \xi^N(x)$, which are slight variations of the parameters $x \in X$, computing the corresponding penalty values $f(\xi^1(x)), \dots, f(\xi^N(x))$ and assigning the average value $F_N(x)$ to the unperturbed leading

configuration. A deformation of the parameters used for the optimization results in coil deformations that preserve the 5-fold and stellarator symmetry of W7-X and target systematic errors that are equal for each coil of the same type during coil fabrication. The way this stochastic optimization problem is approached, one must provide as input a relevant scale length over which the coil deviations are distributed. We determined this as follows: During fabrication of the W7-X winding pack, the average deviation of the non-planar coils from their Computer-Aided-Design (CAD) shape were approximately 2 mm [16]. In the subsequent assembly, reference marks were used to guide and validate the assembly. "In total no reference mark co-ordinate deviated more than 5.7 mm from its manufacture value" [17]. We take these values to define the rough length scale over which we numerically displace coils in our stochastic optimization, since this was actually achieved (and therefore achievable), but only achieved with a significant engineering and metrology effort [3]. Thus, we chose the n -dimensional normal distribution $\mathcal{N}(x, \Sigma)$ appropriately to optimize numerically for robustness against deviations that are 2 mm on average, with greater than 6 mm deviations being present in roughly 10% of the numerically tracked geometric points on the coils in the Euclidean space.

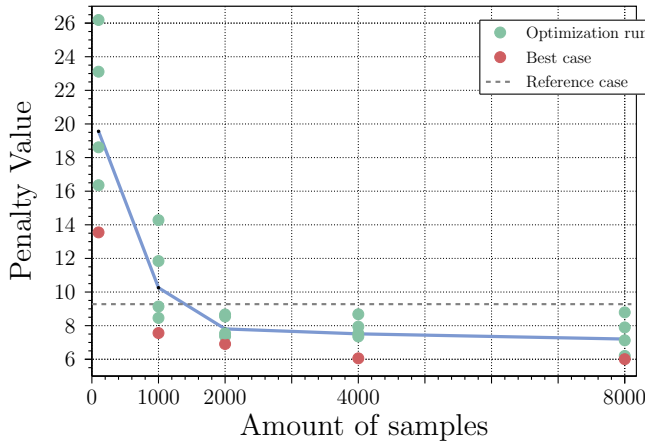
Each time the algorithm computes the modified objective function $F_N(x)$ and evaluates the fitness of the coil set x , the perturbed coil sets $\xi^1(x), \dots, \xi^N(x)$ are defined anew. Thus, the deviations are not only randomly assigned once at the beginning of every optimization sequence but continue to be re-randomized for each evaluation of $F_N(x)$. To provide a comparison basis, the optimization sequence was designed in the classical way $F_1 = f$ with $N = 1$ samples, where only one coil set is evaluated in each optimization step. We call this the reference coil set with cloud size of 1. We then increased the sample size N and optimized with a cloud size of 100, 1000, 2000, 4000, and 8000 perturbed coil sets, so as to determine if there is an optimum cloud size, and some convergence or saturation of the results at very large cloud size. We restricted the coil displacements to variations of the parameters that move the circular spline (coil) along the two-dimensional WS, instead of allowing coil deviations also perpendicular to this surface. This restriction was done in order to keep the computational effort moderate for this first study and we expect to be able to lift this restriction in future studies.

We compare the results of the first optimization run in Section 3.1 by comparing the penalty values. In Section 3.2 we compare the results after the optimization sequence has completed, ie. it has come to a stationary value of F_N . The robustness of the newly optimized coil sets is assessed by plotting the penalty value distributions. They are obtained by deviating the coil sets multiple times at the aforementioned level (average deviation 2 mm). A narrower histogram gives more confidence in the performance, ie. it is more robust against coil deviations of the size assumed here. Another important question arises if the histogram not only narrows (more robust), but also shifts to the left (lower penalty values) indicating that a better optimum has been found, and that the device would accordingly perform better than the device optimized with the classical algorithm. Furthermore, the robustness can also be quantified in terms of relaxed

tolerances, for a given performance. For that, we compare the classically optimized coil set to the best coil set obtained with the new optimization technique.

3.1. Comparison after the 1st optimization run

In Table 1 we compare the results of the 1st optimization run quantified by the penalty value. Since the algorithm is non-deterministic, we assess the results by running the 1st optimization multiple times, as suggested in [11]. Each dot in Figure 2 represents



Samples	#	Best	\varnothing	σ
1	-	9.28	-	-
100	5	13.55	19.56	4.56
1000	5	7.56	10.26	2.47
2000	5	6.91	7.81	0.69
4000	5	6.06	7.51	0.86
8000	5	6.00	7.21	0.95

Figure 2 & Table 1: Results of the 1st optimization run are listed in form of the best coil set (Best), the average penalty value (\varnothing) and the standard deviation (σ)

an independent 1st optimization run. The average penalty value is shown in the blue line. It declines the more samples are used, as does the best result (red dots & Best column). Using the stochastic optimization with a sample size less than or equal to 1000, we observe that the average penalty value is worse than the reference optimization. It indicates that in the transformed parameter space more local optima are present when the sample size is low than in the parameter space of the reference optimization, which causes the optimizer to halt even earlier. Increasing the sample size leads to the intersection between the blue and dashed line, where both parameter spaces have a similar landscape such that both optimization techniques show the same performance. Increasing the sample size further intensifies the smoothing effect and leads to a reduction of local optima which causes the optimizer to find even better results than the reference optimization.

The standard deviation shows that the statistical noise of the penalty values after the 1st optimization run is very high for low sample rates, in addition to the bad performance of the coil sets. A plausible explanation of both negative behaviours is the combination of random samples and the discrepancy between the dimension of the parameter space ($n = 133$) and a sample size of the same magnitude. In each evaluation of the penalty function, the chance is high that not every dimension is covered and the optimal path in

the vicinity of the leading configuration is not visible for the optimizer. The stochastic behaviour of our sampling technique guarantees that these situation happen, sometimes more, sometimes less. In addition to the bad convergence rate of the expected value mentioned in Section 2, this effect leads to an overall poor approximation of the expected value when the sample size is low.

Unfortunately, we do not fully understand all of the effects and their interplay which cause the parameter space to contain more local optima than the reference case for low sample rates but we intend to include a more detailed investigation in our future studies. In general, all statistical measures converge as the sample size increases.

3.2. Comparison after completion of the optimization sequence

We compare the robustness of the design of the coil sets after their last optimization run (cf. Table A1) by analyzing the penalty value distribution for clouds of 100 000 perturbed coil sets around the newly optimized leading coil sets. The entries of 100 000 provide enough statistics to compute the relevant variables of the histogram. The results are shown in Figure 3. The coil shapes are parametrized such that the 2mm average deviation in the Euclidean is not automatically kept, even if the coil shape parameter deviation is kept fixed. Since the WS is part of the optimization and changes its form, the perturbation in the Euclidean space slightly increased over the course of the optimization sequence in the cases with 100, 1000 and 2000 samples. The perturbations in Figure 3 are done with the same technique as described in Section 2 but normalized to reach again an average deviation of 2mm in the Euclidean space. The coil sets are compared by their penalty value $f(x_0)$ and their robustness, which is seen by an increased height and decreased width of the distribution function. Additionally, the high-end tails of the penalty function distributions are analyzed.

In Figure 3 the leading configuration of the optimization with 8000 samples reaches the best result of $f(x_0) \approx 5.39$, and it is nearly identical to the result for a cloud size of 4000, indicating a possible convergence of the penalty values. The reference coil set (using the classical, non-stochastic, optimization) has $f(x_0) \approx 6.65$. Thus, we observe a systematic improvement of this nonlinear coil optimization - irrespective of the issue of robustness, and we see that we need a cloud size above 2000 before the new algorithm outperforms the old one. The width of the distribution is improved already for the smallest cloud size (100), but then actually begins to get wider again for the largest cloud sizes - the coil set optimized with a 2000 sample cloud reaches the highest peak and together with the case of 1000 samples they reach the smallest widths (RMS) of the distribution function. Therefore, the case with 2000 samples is more "robust" in the sense of stable quality criteria, but will have poorer performance than the 8000 sample optimization. Overall, both robustness and average performance are significantly improved over the reference coil set. The double peak of the histogram of the reference coil set is not understood in any detail at this point, but will be further investigated in the future.

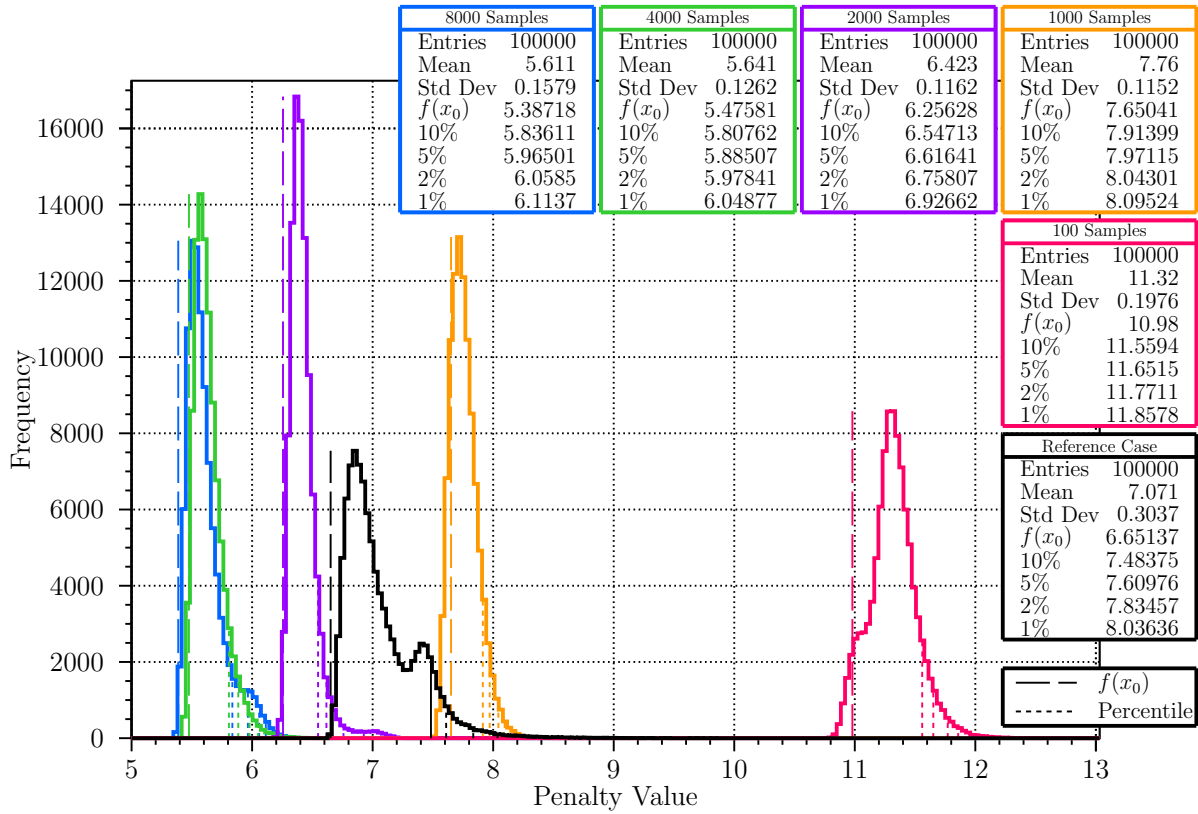


Figure 3: The result of all optimizations including the reference coil set (black) are randomly perturbed 100 000 times and the penalty value distribution is displayed.

The results in Figure 3 are positive, despite this slight broadening of the distribution function for the 4000 and 8000 sample sets relative to the results obtained with the sample size of 2000. From an experimental/user perspective, what is desired is confidence in good performance at tolerances that are relaxed enough that they do not affect the cost or schedule of construction significantly. It is clear from Figure 3 that this optimization is a significant win at the 2 mm accuracy level. This can be quantified further, and put in relation to relaxed engineering tolerances by focusing on the high-end tail of the histogram - the poorly performing configurations.

We plot in Figure 4 the development of the percentiles 10%, 5%, 2% and 1% of the penalty function histogram, thereby quantifying what performance is guaranteed at the 90%, 95%, 98% and 99% confidence level. We compare these percentiles of the reference coil set (classical optimization) and the optimization with 8000 samples (our most comprehensive stochastic optimization). For the 2 mm accuracy case which was used for the optimization and achieved in W7-X (left side of graph) it is again clear, as evident in Figure 3, that the new configuration will outperform the old with better than 99% likelihood. In Figure 4 we now increase the coil tolerances progressively (x-axis) and monitor how the penalty value for these percentiles increases (y-axis). At the 99% confidence level, the classical optimization would have led to a penalty value up to about 8, given the 2 mm tolerances achieved in W7-X. For the new optimization,

the same would be achieved with 99% confidence with coil tolerances of approximately 4.5 mm, more than a factor of two relaxation for the same risk taken. If we lower the degree of confidence (90%, 95%, 98% confidence) the relaxation of tolerances is a bit larger, approaching a factor of three, eg. 5.8 mm tolerances at the 90% confidence level. These comparison points are given as stars. The very steep ascents beyond these values are possibly due to the combination of low statistics and discontinuities in the penalty function, but should be taken with some caution at this point. Regardless of this issue, the data fully supports the statement that the stochastic optimization would give significantly better performance at the same level of engineering tolerances (Fig 3), and comparable if not better performance with a factor of two relaxed tolerances, for a variety of confidence standards.

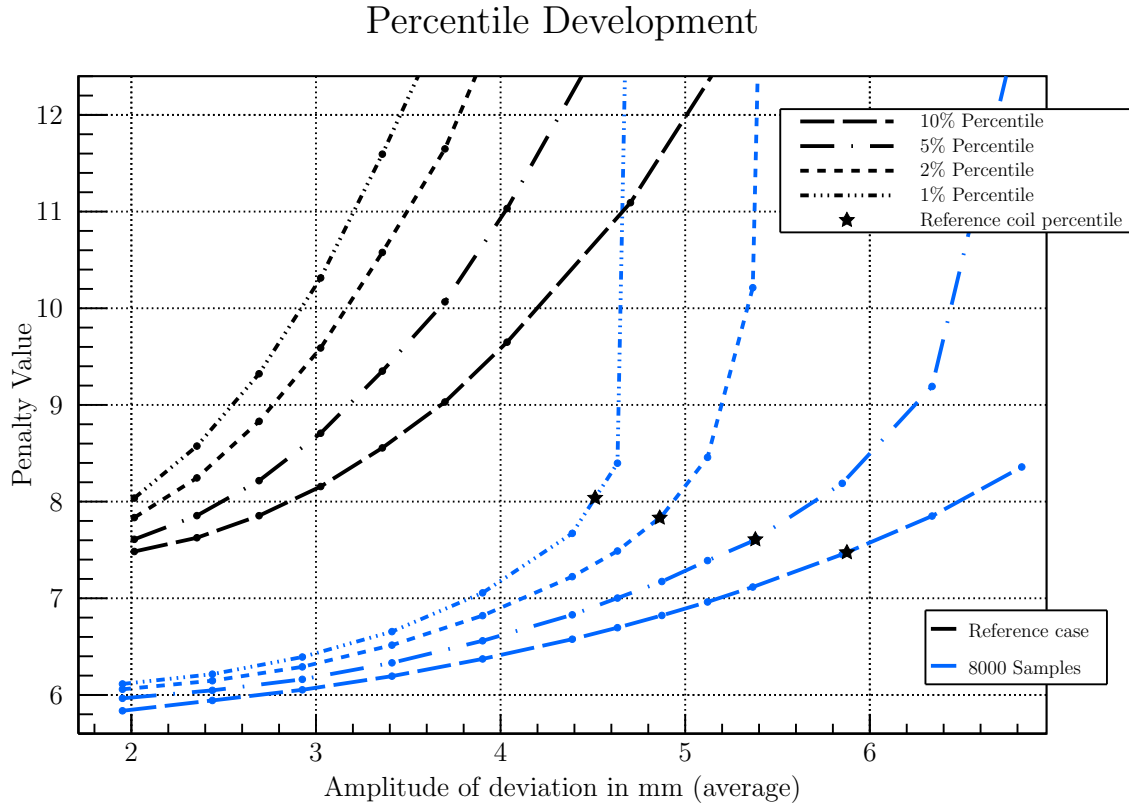


Figure 4: Percentile development of the reference coil case and the optimization with 8000 samples.

3.3. Remark

The object of optimization in this study is the approximation of the expected value which aims to represent the most likely realization of a stellarator. The relaxation of precision requirements is no direct target of the optimization since it is no criterion in the objective function. It is only indirectly represented in the sample average F_N but nevertheless leads to a coil configuration with significantly relaxed tolerances.

The optimization suite ONSET is capable of optimizing the three-dimensional shape of the WS within two constraining toroidal surfaces. This offers the possibility to extend the coil displacements from a non-planar two-dimensional in-surface deviation to also capture three-dimensional deviations. A first attempt at using this feature, which demands significantly more computer resources, has been made and will be reported on in a future publication. Initial results appear consistent with what has been reported here, but convergence studies have not yet been completed.

4. Discussion and conclusion

A stochastic technique of nonlinear coil optimization for stellarators that includes engineering tolerances has been developed and tested on a state-of-the-art optimization problem. The technique shows significant promise. Improved performance is seen - a 20% decrease in the targeted penalty function. The new optimization shows more engineering robustness - the results are less sensitive to coil displacements, and one can relax coil tolerances by at least a factor of two relative to a coil design created using earlier techniques. The relaxation of engineering tolerances was expected. But it was not necessarily expected that the algorithm found a better optimum - irrespective of engineering tolerances. As illustrated in Figure 1, this technique can have a smoothing effect in the otherwise rather spiky optimization space of stellarators, and this may have allowed the algorithm to find a better global optimum than that found by the earlier algorithm. Improved performance and then convergence with sample (cloud) size was seen, with the results from cloud sizes of 4000 and 8000 being nearly identical.

5. Outlook

This work brings up several questions, some of which can be addressed soon. Coil deviations in all three dimensions (not just within a prescribed toroidal surface, and not just stellarator-symmetric) will be addressed next. Additionally, a penalty on the width of the distribution will be included in the objective function in order to directly target reduced precision requirements. The reason why the original algorithm got stuck in a non-global minimum together with the origin of the double peak in the histogram of the reference coil set will be investigated. The new, more optimal, configuration will be compared to the configuration found with the earlier algorithm, in particular with respect to each individual physics target lumped into the penalty function, and the coil geometry will be investigated. At first glance, the geometry of the coils is somewhat different for the newly found coil set but does not appear to be more complicated than what was found with the standard algorithm.

6. Pictures

We compare the shape of the coil set of the optimization with 8000 samples in blue with the reference coil optimization in black in Figure 5 & 6. We show 2 perspectives of one stellarator segment where two half modules are connected at the triangular plane. Figure 5 visualizes the differences from the inside of the torus towards the outside and Figure 6 shows the opposite direction from the outside towards the inside. In general, the two coil sets are quite similar with a certain tendency that the blue coil set is slightly less windy than the reference coil case in black.

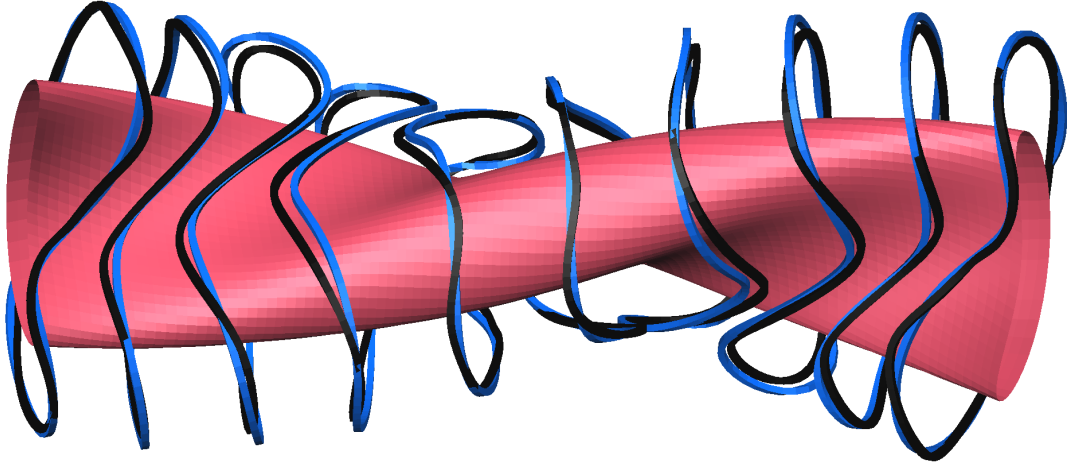


Figure 5: View of two half modules connected at the triangular plane from the inside towards the outside. The coil set in blue is the optimization with 8000 samples and the coil set in black is the reference coil optimization.

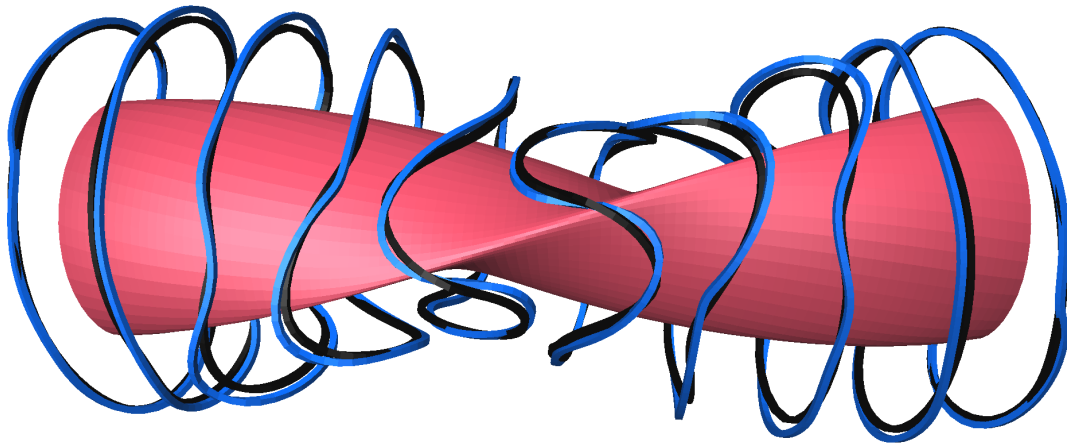


Figure 6: View of two half modules connected at the triangular plane from the outside towards the inside. The coil set in blue is the optimization with 8000 samples and the coil set in black is the reference coil optimization.

7. Acknowledgement

This work has been carried out within the framework of the EUROfusion Consortium and has received funding from the Euratom research and training programme 2014-2018 under grant agreement No 633053. The views and opinions expressed herein do not necessarily reflect those of the European Commission.

References

- [1] Th. Rummel et al., Accuracy of the construction of the superconducting coils for Wendelstein 7-X, *IEEE Trans. Appl. Supercond.* 14(2004)(2(June)), pp. 1394-1398
- [2] T. Sunn Pedersen et al., Confirmation of the topology of the Wendelstein 7-X magnetic field to better than 1:100,000, *Nature Communications* (2016) Vol. 7, 13493
- [3] H.-S. Bosch et al., Final integration, commissioning and start of the Wendelstein 7-X stellarator operation, *Nuclear Fusion*, Vol. 57, 116015 (2017)
- [4] G.H. Neilson, Lessons Learned in Risk Management on NCSX, *IEEE Transactions on Plasma Science*, (2010) Vol. 38, No. 3 pp. 320-327
- [5] R.L. Orbach, Statement about the Future of the Princeton Plasma Physics Laboratory, *Under Secretary for Science and Director, Office of Science*, U.S. Department of Energy, May 22, 2008
- [6] Jason Paul Kremer (2006) *The Creation and First Studies of Electron Plasmas in the Columbia Non-neutral Torus* (Doctoral dissertation) Retrieved from ProQuest Dissertations and Theses. (Accession Order No. AAI3249101)
- [7] T. Sunn Pedersen et al., Construction and initial operation of the Columbia Non-neutral Torus, *Fusion Science and Technology*, Vol. 50, (2006) pp. 372
- [8] T. Sunn Pedersen et al., Experimental demonstration of a compact stellarator magnetic trap using four circular coils, *Physics of Plasmas* **13**, 012502 (2006)
- [9] K.C. Hammond et al., Experimental and numerical study of error fields in the CNT stellarator, *Plasma Physics and Controlled Fusion*, Vol. 58, No. 7 (2016) pp. 074002
- [10] Nührenberg J. and Zille R. 1988 *Physics Letters A* **129** 113-117
- [11] A. Shapiro, Stochastic programming by monte carlo simulation methods, *ESAIM: PROCEEDINGS*, December (2003), Vol. 13 pp. 65-73
- [12] J. Lobsien, M. Drevlak, Status of Coil Optimisation with ONSET, *Manuscript in preparation*.
- [13] P. Merkel, Solution of stellarator boundary value problems with external currents *Nucl. Fusion* (1987) **27** 867
- [14] M. Drevlak, 20th Symposium on Fusion Technology, Marseille, France (1998) pp. 883.
- [15] K. Gegenfurtner, PRAXIS: Brent's algorithm for function minimization, *Behavior Research Methods, Instruments, & Computers*, (1992) Vol. 24, No. 4 pp. 560-564
- [16] T. Andreeva et al., Influence of construction errors on Wendelstein 7-X magnetic configurations, *Fusion Engineering and Design*, 84(2)(2009), p.408 - 412
- [17] T. Andreeva et al., Tracking of the magnet system geometry during Wendelstein 7-X construction to achieve the designed magnetic field, *Nucl. Fusion*, 55(6)(2015), p.063025.
- [18] Michael Drevlak, Automated Optimization of Stellarator Coils, *Fusion Technology*, Vol. 33, No. 2, Page 106-117, Year 1998

Appendices

Appendix A. Details about the optimization sequence

The optimization sequence is listed in Table A1, which illustrates the change of the weight constants throughout the six optimization runs. Every entry consists of two values (design value/ weight constant) which define the objective function f . Exceptions are the limiting surfaces (inner surface / outer surface), and the number of spline points which are defined per coil. The optimization sequence is divided into the optimization of the field error under observance of the geometric restrictions (1-4) followed by the optimization of the properties of the magnetic field. In the final step we compute additionally the Fourier coefficients of a magnetic surface inside the plasma boundary. The difference to the Fourier coefficients obtained from the target magnetic surface inside the original plasma boundary designed by Nühreberg [10] is then minimized in the last optimization run. The optimization of the field error took 4 runs. We refer to [12] for a detailed description of the optimization sequence and the design criteria.

Table A1: Optimization Sequence

Optimization run:	1	2	3	4	5	6
Maximum Field Error	0/ $1.0 \cdot 10^3$
Mean Field Error	0/ $1.0 \cdot 10^5$
Clearance	0.35/1	0.3/1	0.27/1	.	.	.
Curvature	3/0.7
Distortion	0.3/0.4
Magnetic Axis (bean)	-	-	-	-	5.93/4	.
Magnetic Axis (triangle)	-	-	-	-	5.17/15	5.17/450
Magnetic Ripple on Axis	-	-	-	-	0.11/3	.
Iota on Axis	-	-	-	-	$0.88/1.0 \cdot 10^3$.
Magnetic Shear	-	-	-	-	1.56/0.4	1.56/0.8
Magnetic Well	-	-	-	-	$0.007/1.0 \cdot 10^3$.
Fourier Coeff. of inner Surface	-	-	-	-	-	varies/ $1.0 \cdot 10^2$
Limiting Surfaces	+30/+60	.	+30/+65	+30/+70	.	.
Points per Coil	12	.	.	13	.	.
Points of WS	13

Description:

- Target not included in objective function.
- Value from the previous run was used.

Field Error Normal magnetic field on the plasma boundary.

Clearance Minimum distance between adjacent coils.

Curvature Maximum coil curvature $\frac{d^2x}{ds^2}$.

Distortion Weighted curvature defined in [\[18\]](#).

Magnetic Axis Major radius.

A.2. Article II

»Physics analysis of results of stochastic and classic stellarator coil optimization«

J.-F. LOBSIEN et al.

Nuclear Fusion, Vol. 60.4 (Feb. 2020)

Physics analysis of results of stochastic and classic stellarator coil optimization

Jim-Felix Lobsien*

E-mail: jim.lobsien@ipp.mpg.de

Michael Drevlak*

E-mail: michael.drevlak@ipp.mpg.de

Frank Jenko⁺

E-mail: frank.jenko@ipp.mpg.de

Maurice Maurer⁺

E-mail: maurice.maurer@ipp.mpg.de

Alejandro Bañon Navarro⁺

E-mail: alejandro.banon.navarro@ipp.mpg.de

Carolin Nührenberg*

E-mail: Carolin.Nuehrenberg@ipp.mpg.de

Thomas Sunn Pedersen*

E-mail: thomas.sunn.pedersen@ipp.mpg.de

Håkan M. Smith*

E-mail: hakan.smith@ipp.mpg.de

Yuriy Turkin*

E-mail: yuriy.turkin@ipp.mpg.de

W7-X Team

*Max-Planck Institute for Plasma Physics, Greifswald, Germany

⁺Max-Planck Institute for Plasma Physics, Garching, Germany

Abstract. In this paper we follow up on the results from our previous publication [Lobsien J, et al., Nucl. Fus., Vol 58 (2018)106013], where it was found that stellarator coil design optimization can be substantially improved by using a stochastic optimisation approach. In that paper performance was quantified by lower (better) and more narrow (more robust) distributions of the penalty functions at the end of

the optimisations. Here, we evaluate and compare the various coil sets of the previous paper but seek a verification and deeper understanding of the physics performance by replacing the relatively simple penalty function estimate with more accurate ones from state-of-the-art calculations of MHD stability, neoclassical transport in the $1/\nu$ -regime, fast particle confinement, and gyrokinetic behavior. The investigation shows that stochastic stellarator coil optimization generally outperforms the earlier non-stochastic stellarator optimization, also when using these more accurate metrics, generally confirming and quantifying the better performance. We do find some discrepancies, indicating that the penalty function does not represent a physics performance optimum perfectly. For example, as pointed out by others before us, the depth of the magnetic well is not a sufficiently good proxy for MHD stability, and the neoclassical transport can be significantly reduced in configurations that have relatively high field errors and therefore high penalty values. Thus, our work points to areas where better physics model inside the optimisation loop are needed, than what is currently represented by our penalty function.

Keywords: Stellarator, Coil Optimization, Engineering Tolerances, Robust Magnetic Field, Stochastic Optimization, MHD, Neoclassical Transport, Fast-Particle Confinement, Turbulent Transport

Submitted to: *Nucl. Fusion*

1. Introduction

A stellarator is defined by a set of nested toroidal flux surfaces which may be optimized to fulfill multiple performance criteria. In the case of Wendelstein 7-X (W7-X) these criteria were summarized in the W7-X objectives [3], which not only concentrated on the quality of the vacuum magnetic surfaces but also focused on the properties of finite-pressure equilibria. Special emphasis was placed on a small Shafranov shift, good MHD stability properties, a small neoclassical transport, a general reduction of parallel currents, and good α -particle confinement in fusion-relevant operating regimes. All these properties are determined by the shape of the plasma boundary, because this outermost flux surface defines the magnetic field in its interior, which in turn defines the corresponding behaviour when a plasma pressure is present. The design of a stellarator, therefore, may begin with the shape of the plasma boundary and continues with the optimization of a set of finite current-carrying filaments outside the plasma, which is meant to produce the desired magnetic field. The starting point is usually a first guess of the coil structure computed with NESCOIL [4] or REGCOIL [5]. Each coil is then parametrised by either Fourier coefficients or spline points and a penalty function f is defined which measures the difference between the magnetic field produced by the coils and the desired vacuum magnetic field of the stellarator called the *target magnetic field*. Nonlinear coil optimization, as done with codes like ONSET [1], COILOPT⁺⁺ [7] and FOCUS [8], then minimizes this nonlinear function f , which takes the coil parameters

as an input value and summarizes the fitness of the corresponding magnetic field in a real value $y \in \mathbb{R}$. The fitness is characterized by a set of quality criteria of which the field error is the most dominant one. It is quantified by $\mathbf{B} \cdot \mathbf{n}$, where \mathbf{B} is the vector of the magnetic field produced by the coils and \mathbf{n} is the normal on the plasma boundary. In general, \mathbf{B} may include internal plasma currents, which were absent in the optimization of W7-X. The minimization of the field error is one major challenge of stellarator coil optimization but, from a theoretical point of view, deviations from the ideal target are unavoidable due to the discrete nature of the coil set which inevitably produces a corresponding ripple of the magnetic surfaces. Additionally, deviations occur due to geometric constraints necessary for the manufacturing of the coils and assembly of the coil set.

Once the coil optimization arrives at the lower boundary of the field error, the penalty function f is extended by additional quality criteria and the optimization continues. Each new set of quality criteria describes a more intricate property of the set of nested toroidal flux surfaces which define the stellarator. But the more intricate the quality criterion, e.g. effects with finite plasma pressure, the more time it takes to compute a single evaluation of f . Therefore, it is the challenge of nonlinear coil optimization to include new elements within the penalty function f step by step, such that the field error is not increasing while keeping the complexity of the quality criteria in f moderate so as to avoid excessive computing times.

Traditionally, the coil optimization is completed when the underlying magnetic field fulfills the same performance criteria, that initially led to the shape of the plasma boundary. But optimizing them requires a transition of the optimization targets. The optimization of the quality criteria, which reduces the difference between the magnetic field from the coils and the magnetic field defined by the plasma boundary, is replaced by the direct optimization of the performance of the magnetic field produced by the coils. This last step is similar to the optimization of the target stellarator magnetic field itself, with the difference that instead of varying the plasma boundary one changes the coil configuration that defines the plasma boundary.

Once a suitable set of filaments has been found, the focus is changed and the coil configuration is evaluated in a perturbation analysis. Each deviation leads to a change of the magnetic field and consequently to a change in the performance criteria. After performing a statistical ensemble of deviations the perturbation analysis defines a measure of the change of the quality of the magnetic field w.r.t. deformations of the coil set. A prescribed lowest acceptable magnetic field quality then leads to coil construction tolerances which will require more time and resources the lower they are. Unfortunately, recent major stellarator projects have had the tendency to be negatively influenced by their own strict tolerance requirements, e.g. Wendelstein 7-X [9] and NCSX [10].

With the aim to ease the construction of future stellarator projects, we established a stochastic version of stellarator coil optimization that was able to increase the construction tolerances during the design process of the coil configuration [2]. Nonlinear coil optimization is combined with an iterative perturbation analysis with the result

that the target magnetic field is more accurately reproduced and is also more resilient against coil displacements w.r.t. the penalty function f . The new technique replaces the optimization of a single coil configuration f_1 with the optimization of a cloud of neighboring coil configurations f_N . Each element of the cloud is a perturbation of the original coil configuration at the cloud's center. The cloud is characterized by the number of samples N (number of perturbations) and their Gaussian distribution around the unperturbed configuration. With the aim to test the stochastic version of stellarator coil optimization against its classical counterpart, a compact optimization sequence for the original W7-X plasma boundary [11] was developed, in which the complexity of the penalty function stayed rather low. The test included 6 different sample sizes (1, 100, 1000, 2000, 4000 and 8000) and compared the results based on their fitness and robustness w.r.t. f . Here, f_1 is the classic, single coil optimization case. The algorithm together with the optimization sequence is described in more detail in [2]. The 6 optimization runs of the optimization sequence concentrate mainly on the field error and at the end on properties of the vacuum magnetic field, while adhering the geometric constraints throughout the optimization. The penalty values at the end of the optimization sequence resulted in the following ordering of the sample size cases

$$f_{8000} < f_{4000} < f_{2000} < f_1 < f_{1000} \ll f_{100}, \quad (1)$$

where the biggest gap in this order is between the case with 1000 and 100 samples. The case with 8000 samples has a 20% lower penalty value compared to the coil optimization that uses just a single sample. In all cases, the penalty on the field error constitutes 85% of the total penalty value since the design values of the remaining quality criteria are reached with quite high accuracy. The focus of the first study was to demonstrate the advantages of stochastic optimization in the context of stellarator coil design, using only ONSET. The improved results do not necessarily imply that these results are superior to newer coil design tools (such as FOCUS), only that the stochastic optimization itself was beneficial.

During the optimization and subsequent perturbation analysis in [2], the fitness of the coil sets and the corresponding quality of the magnetic fields were measured by the penalty function f . This perspective is limited and shows only the differences w.r.t. the target magnetic field and not how these magnetic field differences influence the more fundamental physics properties of the configuration. In this paper we move beyond the scope of f and compare the coil sets optimized in [2] by the actual performance criteria which lead to the shape of the plasma boundary. We shift the perspective, from investigating properties of magnetic fields to a physics analysis of finite- $\langle\beta\rangle$ equilibria. This way, we make a better assessment of the actual fitness of the coil sets and test the ordering obtained from the penalty values in equation (1) against the number of samples used during the optimization. Loosely formulated, we try to assess how much the lower penalty function has brought us in terms of more fundamental and important physics properties, assessed with the best tools we have available today. It is at least in principle possible that the significantly reduced penalty value in the end does not

translate into significantly improved physics properties. So part of our purpose is also to make a first assessment of the appropriateness of the penalty function itself, although admittedly the data presented here are too sparse to give more than a first indication.

In this physics analysis, the single coil optimization with a single sample is the *reference case* of classic coil optimization and we refer to the rest of the cases optimized in [2] as *stochastic case N*. All the results are ranked with the *target magnetic field*, defined by the original W7-X boundary [12]. The origin of all magnetic fields is explained in more detail in section 2 and their differences w.r.t. the quality criteria used at the end of the optimization are described in section 3. The performance criteria are chosen following the list of the W7-X objectives in [3]. We describe the development of the Shafranov shift in section 4.1 and the global ideal MHD stability properties using the CAS3D stability code [15] in section 4.2. The neoclassical transport will be discussed in section 4.3, and the confinement of fast particles using the ANTS code [16] will be compared in section 4.4. Last but not least, we move beyond the performance criteria for which the W7-X boundary was optimized and present a mode analysis in section 4.5 showing a glimpse into the gyrokinetic behaviour observable in a selection of three cases.

2. Origin of the Magnetic Fields

The optimization that led to the design of the actual W7-X coil set can unfortunately not be reproduced today. That optimization procedure involved iterations and constraints that are not easily automated and not sufficiently documented. Some of these are described below. The optimization, which compared traditional and stochastic stellarator coil optimization used the original W7-X "high-mirror" configuration as the target magnetic field. The boundary was first introduced in [12] but is better described in [20]. The coil configuration that reproduced the magnetic fields of the original W7-X configurational space is no longer available and its shape has repeatedly changed since its first publication in [17]. The main motivation was the manufacturability at the time combined with the additional desire of more experimental flexibility. With the change of the coil configuration the magnetic fields of the W7-X configurational space changed. Consequently, there is a not fully known difference between the original target magnetic field and the magnetic field for which the coils in the end were designed.

We computed an analytic current distribution on a surface outside the plasma boundary with NESCOIL [4], that reproduces the original boundary with acceptable precision. We used the magnetic field produced by this current sheet to obtain the target values used for the optimization and therefore, we refer to this magnetic field as the *target magnetic field*. Choosing a vanishing net toroidal coil current guarantees that the magnetic field of the stellarator can be generated from poloidally closed magnets, and that there is no need for toroidal or helical magnets. This way, a discretization of the current sheet into poloidally closed modular current filaments is possible. These provide the starting point of the coil optimization with ONSET [1] and its stochastic

extension [2]. The optimization ended after 6 runs with the coil sets that produce the magnetic fields we refer to as the *reference case* and the *stochastic cases*.

The finite- $\langle\beta\rangle$ MHD equilibria of the 7 magnetic fields are computed with the free boundary version of VMEC [18] [19], where we use the pressure profile of the stability analysis [20] of the original W7-X configurational space [11] which is proportional to

$$p(\rho) \propto 7 - 11\rho^2 + 4\rho^4, \text{ where } 0 \leq \rho \leq 1 \quad (2)$$

is the minor radius normalized to the minor radius of the last closed flux surface. VMEC is used with 65 flux surfaces allowing residual forces of the order of 10^{-11} . The resolution of the MGRID files uses 130 points in radial- and z-direction and 62 points in φ -direction. Here we denote that the optimization of the finite- $\langle\beta\rangle$ effects of the original W7-X boundary was done using the fixed-boundary VMEC. This means that the free-boundary VMEC equilibrium of the target magnetic field was never directly optimized, only indirectly through the fixed-boundary VMEC studies.

3. Quality Criteria

The quality criteria used during the optimization are visualized in figure 1 and the corresponding values of the stochastic and reference cases together with the target values are listed in table A1 of the Appendix A. We added the corresponding penalty values to better assess equation (1). During the optimization, the squared residual of each quality criterion w.r.t. its corresponding target value was a weighted part in the penalty function f whose minimization was the main task of the optimization sequence described in [2].

The field error is quantified with two values, the maximum local field error $\max e_l = \frac{|\mathbf{B} \cdot \mathbf{n}|}{|\mathbf{B}|}$, where \mathbf{B} is the vector of the magnetic field and \mathbf{n} is the normal on the plasma boundary, and the average global field error $e_a = \frac{\int_A e_l dA}{A}$, where A is the area of the plasma boundary. They are the most dominant quality criteria in the penalty function directly quantifying the difference between the target magnetic field and the magnetic field produced by the coils. The target magnetic field is produced by an analytic current distribution computed with NESCOIL (12 poloidal and 10 toroidal modes) on a current-carrying surface 30 cm outside the plasma boundary. Its field error sets the lower boundary compared to the field errors of the coil optimization study as can be seen in table 1.

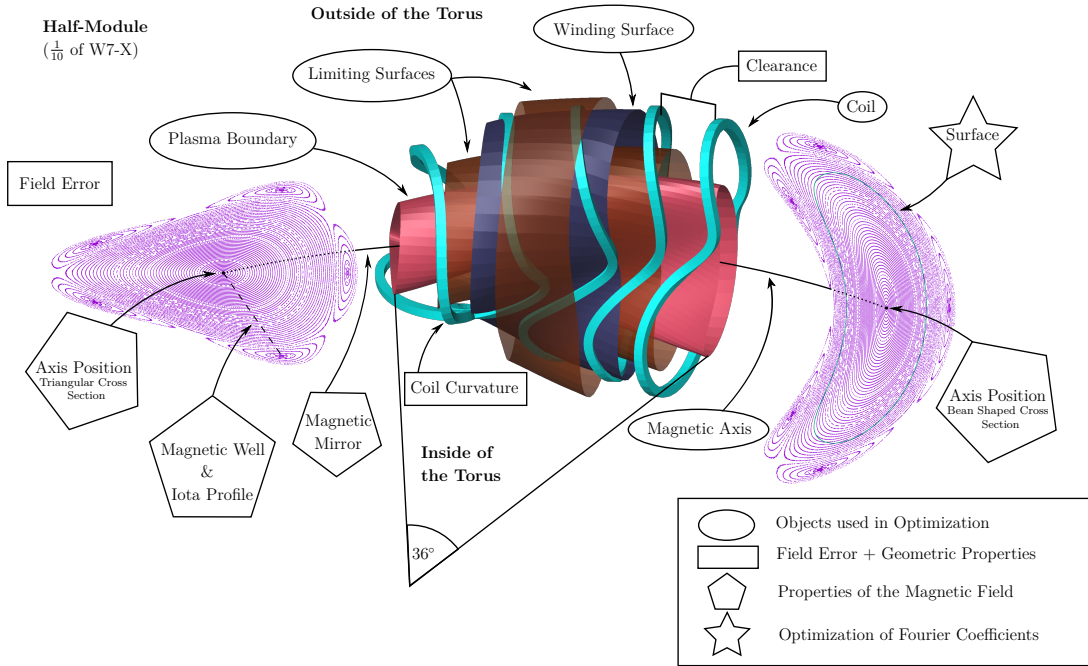


Figure 1: A W7-X half-module is shown together with the surfaces used during a stellarator coil optimization with ONSET [1]. Additionally, we present the quality criteria used during the compact optimization sequence cf. A1.

Table 1: Values of the Field Error

Magnetic Fields:	Maximum Local Field Error:	Average Global Field Error:
Target Magnetic Field	3.4×10^{-4}	9.5×10^{-5}
Stochastic Case 8000	6.0×10^{-2}	1.6×10^{-2}
Stochastic Case 4000	5.7×10^{-2}	1.66×10^{-2}
Stochastic Case 2000	6.0×10^{-2}	1.95×10^{-2}
Reference Case	7.0×10^{-2}	1.7×10^{-2}
Stochastic Case 1000	7.0×10^{-2}	1.92×10^{-2}
Stochastic Case 100	8.0×10^{-2}	2.27×10^{-2}

The differences in the field error between the optimized coil cases reflect the order of the penalty values in equation (1) obtained after the optimization and highlights that the stochastic case 8000 has nearly the same field error as the stochastic case 4000, that the reference case is somewhere between the stochastic case 2000 and stochastic case 1000 and that the worst values with the largest gap among the coil cases has the stochastic case 100. The vacuum Poincare plots of all the magnetic fields at the bean-shaped cross section presented in figure 2 confirm this situation and show that the magnetic field of the stochastic case 100 deviates most from the target magnetic field. But variations in the Poincare plots do not necessarily lead to changes in the plasma performance as stated in [13] and [14]. Table A1 visualizes in numbers that all coil configurations show

quite good agreement on the properties of the vacuum magnetic field and meet the geometric constraints such that all coil configurations are valid approximations of the target magnetic field.

Vacuum Field Poincare Plots

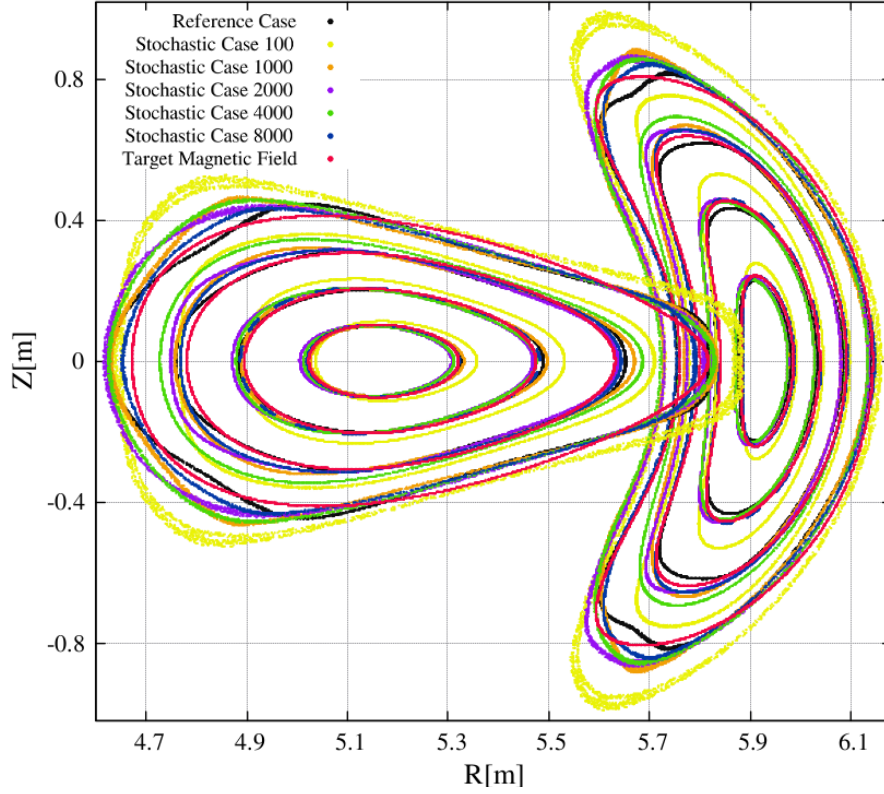


Figure 2: Poincare plots of the vacuum field at the bean-shaped and triangular cross section

The geometric properties of the filament structure guarantee the feasibility of the stellarator construction. The material used and consequently the extent of the coil usually defines the maximal allowed coil curvature. It is defined as $\kappa = \frac{1}{R}$, where R is the radius of the smallest circle representing a coil segment. Additionally, one tries to avoid unnecessary undulations, which is enforced by the second curvature. It is a weighted integral of the first curvature and fully described in [22]. The finite extent of the coil also defines the required clearance between adjacent coils, and the two limiting surfaces guarantee that the coils do not get too close or too far away from the plasma boundary. Besides these properties, coil to plasma separation and coil length ([5], [6], [8], [21]) are often used as design metrics.

The basic properties of the magnetic field are characterized by 7 aspects in the penalty function:

- The magnetic axis is determined at the beginning and at the end of the half-module.
- The difference between the magnetic field strength on the axis at the start and at the

end of the half-module is referred to as the magnetic mirror. It is normalized to the sum of the two magnetic field strength values. It is important for the confinement of fast particles and will be discussed in section 4.4.

- The value of iota on the axis and the shear is determined. The latter is computed by taking the difference of iota on axis and iota 0.2m off axis at the beginning of the half-module at $z = 0$.
- The change of the magnetic volume along the radial direction is summarized in the magnetic well, which is necessary for the global MHD stability and will be discussed in section 4.2.
- The Fourier coefficients of inner flux surfaces can be computed and optimized towards the coefficients of the corresponding surfaces of the target magnetic field. They are derived in PEST coordinates [45] and we chose the R_{mn} and Z_{mn} of a flux surface slightly inside the plasma boundary.

3.1. Remark:

We point out, that only the values of first curvature, the clearance and the two axes positions have physical units.

4. Performance Criteria

4.1. Shafranov Shift

The Shafranov shift measures the deviation of the magnetic axis when a plasma pressure is applied. The reduction of the Shafranov shift was one of the key objectives in the design of W7-X [3].

In figure 3 we compare the position of the magnetic axis at both up-down symmetric plasma cross sections as a function of normalized plasma pressure ($\langle\beta\rangle$). The Shafranov shift between $\langle\beta\rangle = 0\%$ and $\langle\beta\rangle = 5\%$ measured at the bean-shaped cross section is about 1 cm lower for the stochastic case 100 compared to the rest of the cases. They all have almost the same shift with the reference case having the largest one. At the triangular cross section the stochastic case 100 has again the smallest Shafranov shift, which is this time 2 cm smaller than the Shafranov shift of the reference case. The rest of the cases including the target magnetic field have a Shafranov shift in between the latter two cases, around 1 cm higher than the stochastic case 100 and around 1 cm lower than the reference case. The Shafranov shift is in general a factor of two lower at the bean-shaped cross section compared to the triangular cross section due to the different elongations of the two cross sections. The results yield the following ordering:

$$f_{100} < \text{Target} \approx f_{8000} \approx f_{4000} \approx f_{2000} \approx f_{1000} < f_1. \quad (3)$$

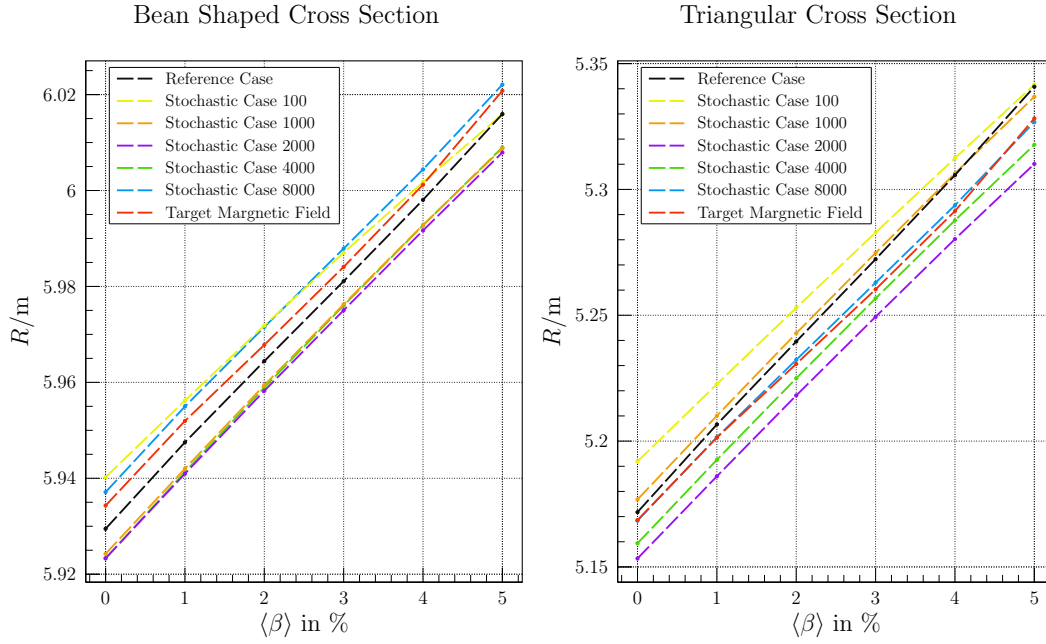


Figure 3: Shift of the magnetic axis from $\langle\beta\rangle = 0\%$ up to $\langle\beta\rangle = 5\%$ measured at both ends of the half-module.

4.2. Stability

The depth of the magnetic well is a figure of merit in the ideal MHD considerations [23]. Having a magnetic well means that the rate of increase of the contained magnetic volume with toroidal flux, $V'(s)$, decreases with radius, i.e. $V''(s) < 0$ [24]. In ONSET, the magnetic well is defined as the normalized difference of the specific volume of two well-separated magnetic surfaces (including the magnetic axis)

$$-2 \cdot \frac{V'_2 - V'_1}{V'_1 + V'_2}. \quad (4)$$

Here V'_1 is the specific volume belonging to the magnetic surface closer to the magnetic axis and V'_2 the corresponding specific volume belonging to the magnetic surface closer to the last closed flux surface. During our optimization we computed V'_1 on the magnetic axis and V'_2 on the surface at $\rho = 0.2$, where ρ is the normalized minor radius. The specific magnetic volume is computed as the average line integral along a magnetic field line normalized by the magnetic field strength and is expressed as the limit of

$$\lim_{N \rightarrow \infty} \frac{1}{N} \int_N \frac{dl}{B} = \frac{dV}{d\Psi} \quad \text{with } \Psi - \text{toroidal flux.} \quad (5)$$

The target magnetic field provides the design value of the magnetic well of 7.0×10^{-3} . The stochastic cases 4000 & 8000 possess a deeper magnetic well of $\approx 8 \times 10^{-3}$ and the reference case has a more shallow magnetic well of 5.4×10^{-3} . The magnetic well of the stochastic cases 100 & 1000 & 2000 is more than two times deeper than the magnetic well of the stochastic cases 4000 & 8000. Having a magnetic well is a necessary condition

for global ideal MHD stability and the result suggests that the stochastic cases are more stable than the reference coil case.

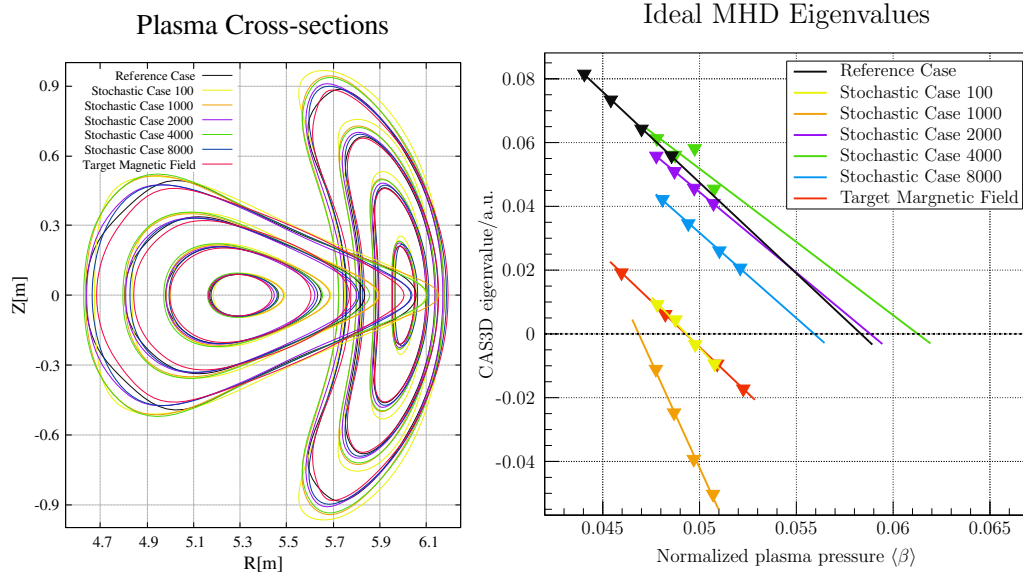


Figure 4: *Left:* Cross sections of the equilibria at $\langle\beta\rangle = 0.048$ at the triangular- and bean-shaped cross section. *Right:* Ideal MHD eigenvalue calculations versus average plasma- β .

We discuss the global ballooning stability of the reference and stochastic cases and compare the results with the target magnetic field based on four MHD equilibria each. The volume-averaged plasma- β is varied in a small range around the W7-X beta stability limit of about 5%. The rotational transform varies between $\iota = 5/6$ near the magnetic axis and $\iota = 5/5$ near the plasma boundary in the reference and the stochastic cases. Only in the target magnetic field we see $\iota < 0.8$ on the axis. For the equilibria at $\langle\beta\rangle = 0.048$ two characteristic plasma cross sections of one half-module are shown in figure 4 (left).

The ideal MHD computations were done using the CAS3D code [15] with 520 Fourier harmonics for the scalar perturbation components and 64 equidistant flux intervals for the radial discretization. We consider even-parity fixed-boundary perturbations for which the normal displacement is up-down symmetric on the up-down symmetric plasma cross sections, i.e. at the bean-shaped and triangular cross sections, figure 4 (left). The angular resolution is reduced by using a phase-factor transform that extracts a potentially strongly varying part of the scalar perturbation components.

Global ballooning stability prevails for the β -values studied of the reference case and stochastic cases 8000 & 4000 & 2000 as can be seen from their positive eigenvalues in figure 4 (right). The target magnetic field together with the stochastic cases 100 & 1000 have unstable eigenvalues for the poloidal mode number ≈ 100 considered in figure 4. Here, extrapolation from the stable or unstable side yields points of marginal stability. Above the marginal plasma- β the equilibrium is predicted to be unstable. Hence looking

at the modes with poloidal mode number ≈ 100 , we can derive the stability limit of all the cases shown in table 2.

Table 2: Stability limit of poloidal mode number 100

Magnetic Fields:	Stability Limit:
Stochastic Case 1000	$\langle\beta\rangle = 4.7\%$
Stochastic Case 100	$\langle\beta\rangle = 4.9\%$
Target Magnetic Field	$\langle\beta\rangle = 4.9\%$
Stochastic Case 8000	$\langle\beta\rangle = 5.6\%$
Reference Case	$\langle\beta\rangle = 5.8\%$
Stochastic Case 2000	$\langle\beta\rangle = 5.9\%$
Stochastic Case 4000	$\langle\beta\rangle = 6.1\%$

Higher mode numbers give more stringent stability limits, but the respective spatial structure is of very small scale. The wavelength of the poloidal mode number ≈ 100 is only one order of magnitude above the Larmor-radius of gyrating ions moving in the corresponding magnetic field. Therefore, the spatial structure is close to the point where physics beyond ideal MHD should be taken into account.

The MHD ballooning stability properties of the reference case and the stochastic cases 2000 & 4000 & 8000 are almost the same and somehow more stable than the target magnetic field. Even though the latter cases are mere approximations of its vacuum magnetic field their rotational transform profile has less shear than that of the target magnetic field at finite plasma- $\langle\beta\rangle$. The stochastic case 100 is as stable as the target magnetic field and only the stochastic case 1000 is less stable. The maximum amplitudes of the normal-displacement harmonics are located quite close to the edge in the stochastic cases 100 & 1000 for which, near the plasma boundary, the local stability Mercier criterion is violated, too. Therefore, we additionally looked at medium-mode-number free-boundary perturbations and compared the stability limits of the poloidal mode number ≈ 30 . This new perspective does not change the order obtained before and just decreases the values of the stochastic cases 100 & 1000 while increasing the values of the rest.

The values of the magnetic well are insufficient indicators, since they indicate a greater difference between the stochastic and reference cases. Here we point out that the optimization leading to the W7-X configurational space was based on fixed-boundary equilibria and that MHD stability properties entered the target function by evaluation of local stability criteria (Mercier and resistive interchange) or driving terms (local field-line ballooning) [11]. Nevertheless, both investigations arrive at a similar $\langle\beta\rangle$ -limit. Besides the vacuum-field magnetic well, other equilibrium properties are important in global ideal MHD stability, e.g. the rotational transform profile. Falling below $\iota=5/6$ in the target magnetic field in part explains why a decrease in vacuum-field magnetic

well does not result in an increased $\langle\beta\rangle$ -stability limit. The final order is:

$$f_{4000} < f_{2000} < f_1 < f_{8000} < \text{Target} < f_{100} < f_{1000}. \quad (6)$$

4.3. Neoclassical Transport

The neoclassical confinement at low collisionalities in the $1/\nu$ -regime can be characterized by the 'effective helical ripple' ϵ_{eff} (see [25] and references therein). This quantity can be determined efficiently from an analytic solution of the bounce-averaged drift kinetic equation to calculate the neoclassical transport coefficients without using a simplified model of the magnetic field [26].

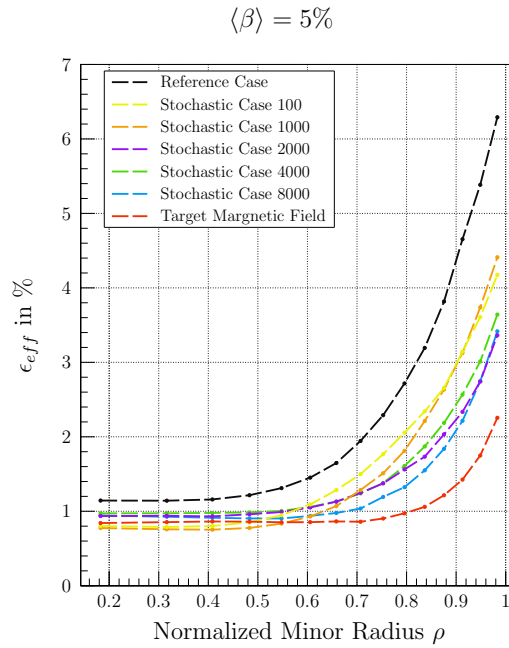


Figure 5: Profile of epsilon effective at $\langle\beta\rangle = 5\%$

In figure 5 we illustrate the ϵ_{eff} profile of all 7 cases at $\langle\beta\rangle = 5\%$. The radial profile is in all cases quite similar and only differs in the initial value and the ascent towards the edge. The target magnetic field reaches on average over the whole radial extent the lowest ϵ_{eff} profile. Its performance is only rivalled by the stochastic cases 100 & 1000 close to the magnetic axis. Their profile, in turn, has a steep ascent towards the edge which is comparable to the ascent of the reference case which has by far the highest ϵ_{eff} values. The 2nd best ϵ_{eff} performance has the stochastic case 8000 which is closely followed by the stochastic cases 2000 & 4000.

The magnetic field in Boozer coordinates can be described by Fourier coefficients b_{mn} . The Shafranov shift reduces the magnetic mirror term b_{01} when increasing $\langle\beta\rangle$ from 0% to 5% which leads in all cases to a decrease of ϵ_{eff} close to the axis [27]. The second consequence of the Shafranov shift is a general increase of the magnitude of the higher Fourier harmonics which leads to an increased transport gradient at the edge.

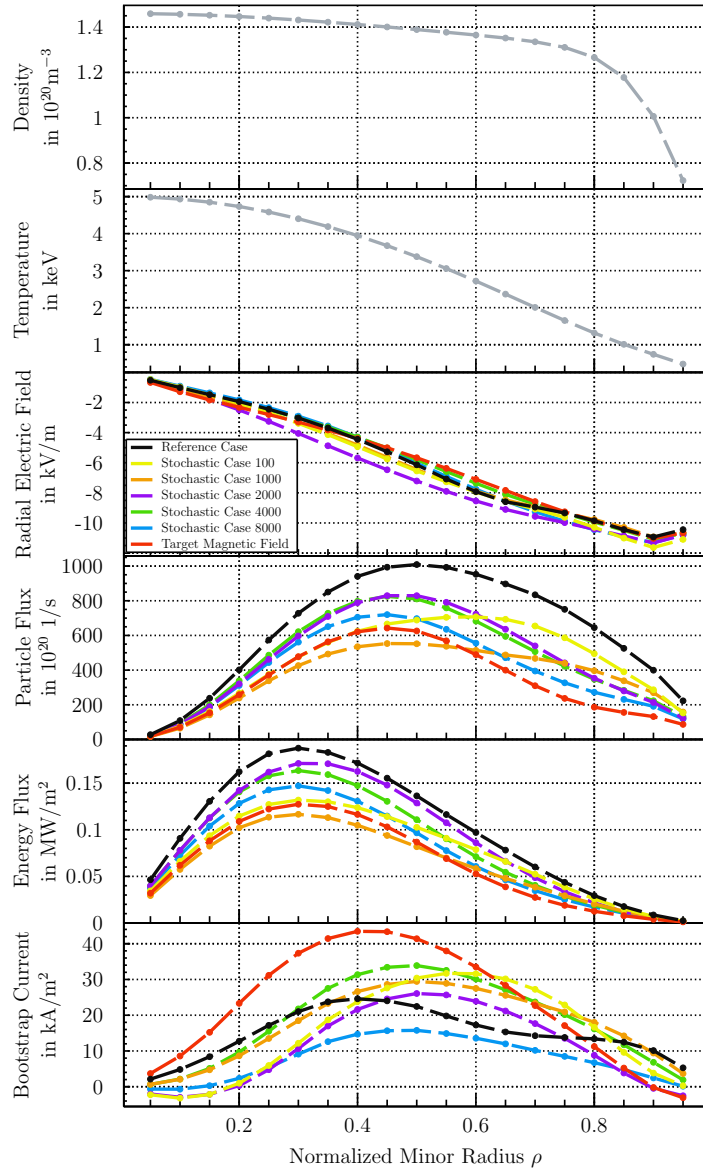


Figure 6: The neoclassical transport is shown for the density and temperature distribution displayed in the top first and top second picture. From third top to bottom the radial electric field, particle and energy flux and the bootstrap current is displayed all along the radial direction.

In figure 6 we present neoclassical transport calculations based on the 'Drift Kinetic Equation Solver' DKES [28] [29]. In order to reach $\langle\beta\rangle = 5\%$ we chose a density of $1.46 \times 10^{20} \text{ m}^{-3}$ and a temperature of 5 keV in the core. The corresponding profiles are shown in the first and second frame of figure 6. Their shape is chosen similar to profiles found during the experimental campaign OP1.2 of W7-X while the overall pressure profile reaches $\langle\beta\rangle = 5\%$. A multiplication of the density and temperature profile yields the pressure profile defined in (2), which was used for the equilibria calculations with the free boundary version of VMEC [19]. The radial electric field, the energy and particle

fluxes together with the bootstrap current along the radial direction are shown in figure 6 (third to bottom frame, respectively). There is almost no difference in the radial electric field, but the development of the particle and energy flux in the radial direction reflects that the ϵ_{eff} -profile is highest for the reference case. The stochastic case 8000 and the target magnetic field have quite similar energy flux development but are noticeably lower than the reference case. The stochastic cases 100 & 1000 have the same particle and energy flux as the target magnetic field close to the core but diverge towards the edge. The particle and energy flux development of the stochastic cases 2000 & 4000 lies in between the reference case and the stochastic case 8000. A different picture presents itself regarding the development of the bootstrap current as can be seen in table 3, where we integrated the bootstrap current density over the cross sectional area.

Table 3: Integrated bootstrap current density over the cross sectional area.

Magnetic Fields:	Bootstrap Current
Stochastic Case 8000	17 kA
Stochastic Case 2000	22 kA
Reference Case	28 kA
Stochastic Case 100	31 kA
Stochastic Case 1000	32 kA
Stochastic Case 4000	33 kA
Target Magnetic Field	35 kA

The stochastic case 8000 has the lowest total bootstrap current, the reference case is situated in the middle and the highest bootstrap current is found surprisingly in the target magnetic field. A calculation of the equivalent bootstrap current of an elongated tokamak (corr. scale found in [31]) with the same volume and aspect ratio with NTSS [32] yields values around 220 kA. The bootstrap current of a more realistic circular scaled tokamak with the same volume and aspect ratio would yield values around 600 kA. Consequently, the bootstrap current is significantly reduced in all 7 cases considered, which confirms the minimization of the bootstrap current of the HELIAS line described in [30]. The small differences in total bootstrap current between the cases can thus be neglected.

In summary, the neoclassical confinement is best in the target magnetic field and closely followed by the stochastic case 8000 & 1000, which have almost the same performance. The rest of the stochastic cases have worse neoclassical confinement although still better than the performance of the reference case, yielding the following order:

$$\text{Target} < f_{8000} \approx f_{100} < f_{4000} \approx f_{1000} < f_{2000} < f_1. \quad (7)$$

4.4. Fast Particle Confinement

In the case of W7-X a magnetic mirror of 10% or higher is a necessary condition to assure good α -particle confinement [33]. All the stochastic cases with $N > 0$ ended the optimization sequence with the same magnetic mirror as the target magnetic field and only the reference case reaches a slightly higher magnetic mirror of $\sim 13\%$. Unfortunately, the magnetic mirror is not a direct proxy for fast particle confinement which means that a higher magnetic mirror does not necessarily mean better fast particle confinement.

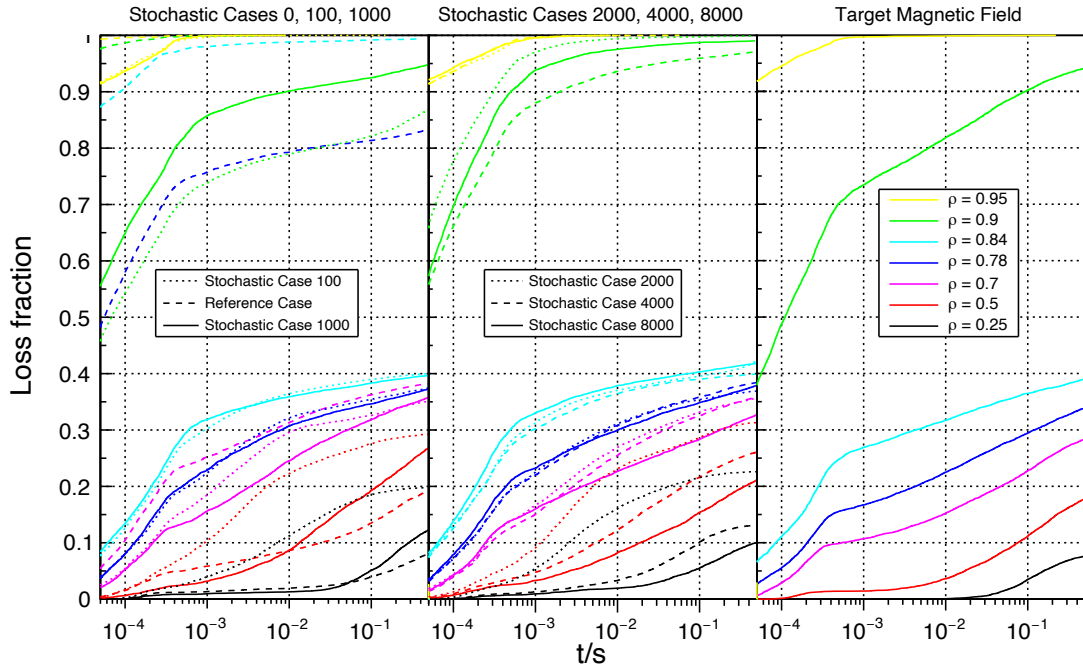


Figure 7: Comparison of the loss fraction of fast particles initiated at different starting positions along the radial direction. The reference case together with the stochastic cases 100 & 1000 are situated left, the stochastic cases 2000 & 4000 & 8000 are in the middle and the target magnetic field is placed on the right.

We measure the fast particle confinement of the 7 magnetic fields with ANTS [16]. Along the radial direction, 7 different starting positions are defined at $\rho = 0.25, 0.5, 0.7, 0.78, 0.84, 0.9, 0.95$. At each radial position an ion population of 10000 particles was initiated and the loss fraction was measured as a function of time. The deuterium ions are initiated with a kinetic energy of 60 keV, which yields about the same gyroradius-to-system-size ratio as for fusion alpha particles at 3.5 MeV in a HELIAS reactor [34]. We do not consider collisions while tracing the particles along the field lines in the magnetic field of a $\langle \beta \rangle = 5\%$ equilibrium.

In figure 7 we compare the development of the loss fraction as a function of time starting with the reference case and the stochastic case 100 & 1000 on the left, the

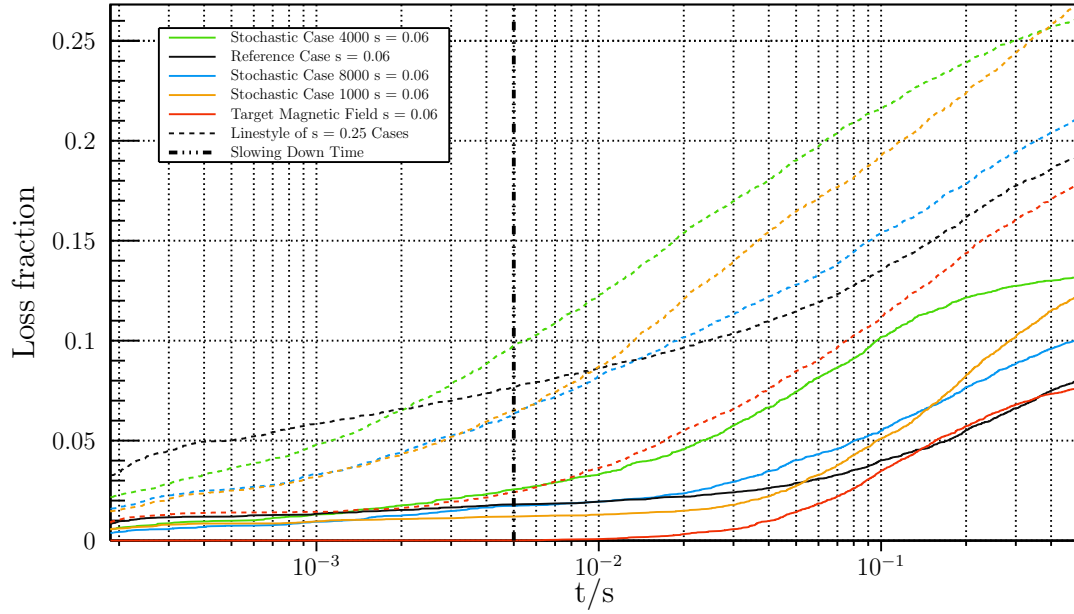


Figure 8: Zoom into the comparison of the loss fraction of the ion populations starting at $\rho = 0.25$ and $\rho = 0.5$. Additionally, the slowing down time in a similar W7-X magnetic field is indicated.

stochastic cases 2000 & 4000 & 8000 in the middle and the target magnetic field on the right. The latter exhibits excellent fast particle confinement near the axis, as is evident by the small loss fraction for $t < 2 \times 10^{-2}$ s. Details about its optimization, which focused on the confinement close to the axis only, can be found in [11]. During the optimization of the magnetic fields of the stochastic and the reference cases no proxy for the confinement of fast particles was used due to their time-intensive computation. Therefore, the fast particle confinement was only indirectly optimized through the field error.

As expected, the target magnetic field has the best confinement of fast particles at each starting position. If we compare the rest of the cases at $\rho \geq 0.7$, we see that the reference case has noticeably the worst performance while the stochastic cases with $N > 0$ have almost the same performance. At $\rho = 0.7$ we find, surprisingly, the performance ordered by the number of sample used during the optimization ($f_{8000} < f_{4000} < f_{2000} < f_{1000} < f_{100} < f_1$). Looking at the two starting positions close to the axis ($\rho = 0.25$ and $\rho = 0.5$), we see the worst performance from the stochastic case 100 & 2000. A comparison between the remaining 5 cases is shown in figure 8. Additionally, we added the slowing-down time of 5×10^{-3} s computed for a similar W7-X magnetic field stated in [35]. Its magnetic configuration only reaches a pressure of $\langle \beta \rangle = 4\%$, but the density of $1.6 \times 10^{20} \text{ m}^{-3}$ is comparable to the one shown in section 4.3. A comparison at this particular time step shows that at $\rho = 0.25$ the

fast particle confinement is second best for the stochastic case 1000, closely followed by the stochastic case 8000 and the reference case which have the same performance. At $\rho = 0.5$ the stochastic case 1000 & 8000 have the second best performance after the target magnetic field with a slightly better performance than the reference case. At both starting positions, the stochastic case 4000 performs worst among the cases considered in figure 8.

In summary, the fast particle confinement is best in the target magnetic field, which is closely followed by the stochastic cases 1000 & 8000 which have almost the same performance. Their performance is quite similar to the reference case, but only close to the axis. For $\rho \geq 0.7$ the reference case actually performs worst. Consequently, the performance of the stochastic case 4000 is still better than the reference case which is only better than the stochastic case 2000 & 1000 due to their bad performance close to the axis. The final order is:

$$\text{Target} < f_{8000} \approx f_{1000} < f_{4000} < f_1 < f_{2000} \approx f_{100}. \quad (8)$$

4.5. Turbulent Transport

As neoclassical transport is suppressed, turbulent transport becomes more important in present day stellarators like W7-X [36]. Therefore, attempts have been made to develop models to predict turbulent transport in stellarators in order to optimize future devices [37]. Here, we show simulation results produced by GENE-3D, the radially-global stellarator version of the grid-based gyrokinetic turbulence code GENE [39, 38, 40] which was recently developed at IPP Garching [41]. Previous studies of stellarators with GENE were limited to the flux-tube and flux-surface global version of GENE [42, 43]. This is one of the first studies performed with the fully global GENE-3D code. We compare three different equilibria mentioned in section 2 w.r.t. to two different temperature and density profiles. The first profile type was used in the investigation of the neoclassical transport of section 4.3 and the second profile type is a standard used in GENE. Its gradient peaks at $\rho = 0.5$ and has a Gaussian like shape (see fig. 9). It allows GENE simulations to run accurately with relatively low resolution requirements and hence lower computational cost. The differences of the profiles in location and height of the peak of the gradients can lead to different mode structures in GENE-3D simulations which is part of the upcoming investigation.

4.5.1. Linear simulations with adiabatic electrons Figure 10 shows the most unstable modes drifting in the ion diamagnetic direction in linear simulations assuming Boltzmann-distributed electrons. Looking at the solid lines which correspond to the profiles used in the neoclassical transport investigation of section 4.3, the reference case and the stochastic case 8000 peak at the same toroidal mode number of $n = 110$ and the target magnetic field peaks at a slightly smaller mode number of $n = 105$. A higher mode number indicates that the underlying mode structure varies on a smaller scale. Large scale instabilities are however more relevant in nonlinear simulations as

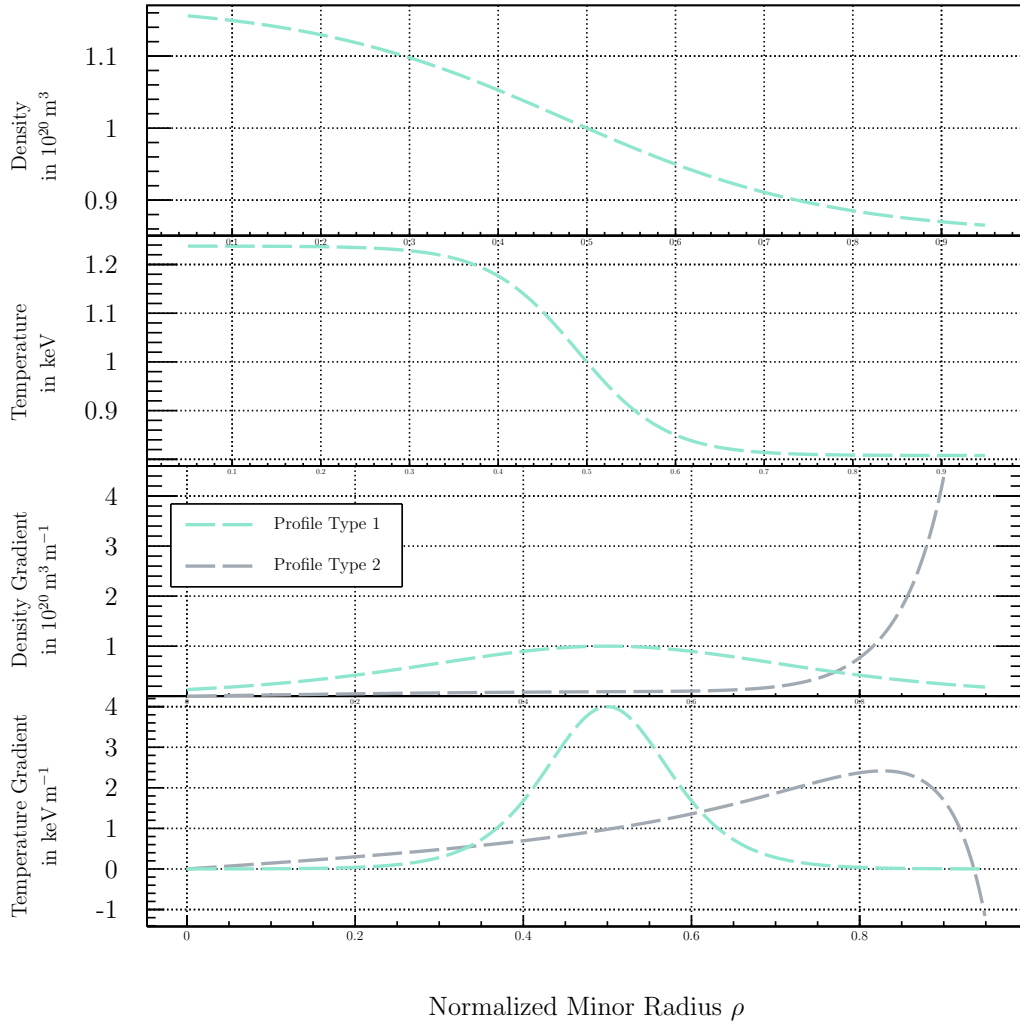


Figure 9: Density and temperature profiles used in GENE-3D simulations for the mode analysis. The gradient profiles have very different shape and peak at different positions and can therefore lead to different dominant modes in the simulations.

they lead to more particle and heat transport. The picture stays the same when looking at the growth rates, where the target magnetic field has a slightly higher growth rate of $\gamma = 0.146 \frac{v_i}{a}$ compared to $\gamma = 0.137 \frac{v_i}{a}$ for the other two cases. Here, v_i is the ion thermal velocity defined as $\sqrt{T_{i0}/m_i}$ and a is the minor radius.

Looking at the dashed lines of figure 10 which correspond to the profile type 2 in figure 9 the reference case and the stochastic case 8000 peak again at the same toroidal mode number of $n = 175$ but with slightly different growth rates. This time the target magnetic field peaks at a slightly higher toroidal mode number of $n = 185$ and has a noticeably higher growth rate of $\gamma = 0.202 \frac{v_i}{a}$.

As both temperature profiles show similar behavior in respect to differences in the magnetic field geometry we continue the simulations using the profile type 2 which leads to lower computational cost of the GENE-3D simulations.

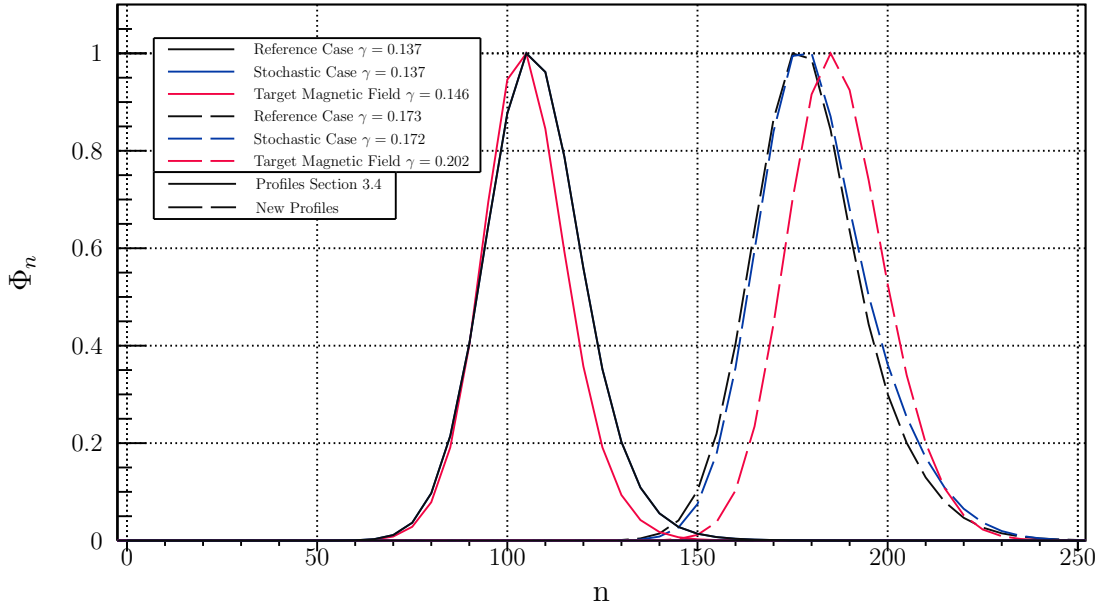


Figure 10: Most unstable modes in linear simulations of adiabatic electrons. Two different temperature and density profiles were used.

4.5.2. Linear simulations with kinetic electrons An explicit electron species can change the outcome of a simulation as the dominant mode can have different characteristics. Theoretically, the mode can change from ion modes such as ion temperature gradient (ITG) modes to electron modes such as electron temperature gradient (ETG) modes or trapped electron modes (TEM). Therefore, we repeated the tests of section 4.5.1 for kinetic electrons to investigate their effect on the mode structure and small changes in the geometry. We assume the same density and temperature gradient for the electrons as for the ions, such that the two linear cases differ only by the additional explicit heavy electron species in the system with $m_e/m_i = 1/100$ (m_e : electron mass, m_i : ion mass).

As can be seen from figure 11, adding kinetic electrons to the simulations shifts the toroidal mode number to higher values and increases the growth rate. In the performed simulations with kinetic electrons the dominant mode is still rotating in the ion diamagnetic drift direction like with adiabatic electrons. The up shift in mode number due to kinetic electrons is smallest in the target magnetic field and largest in the reference case. But in general the up shift is smaller than the change of mode number due to the difference in profiles, which indicates that an explicit electron species in the simulations does not have a strong effect on the underlying instability. The reference case again has the lowest growth rate while the target magnetic field has the highest.

4.5.3. Nonlinear simulations with adiabatic electrons Adding kinetic electrons to the simulations in the linear scenario did not have a strong effect on the outcome.

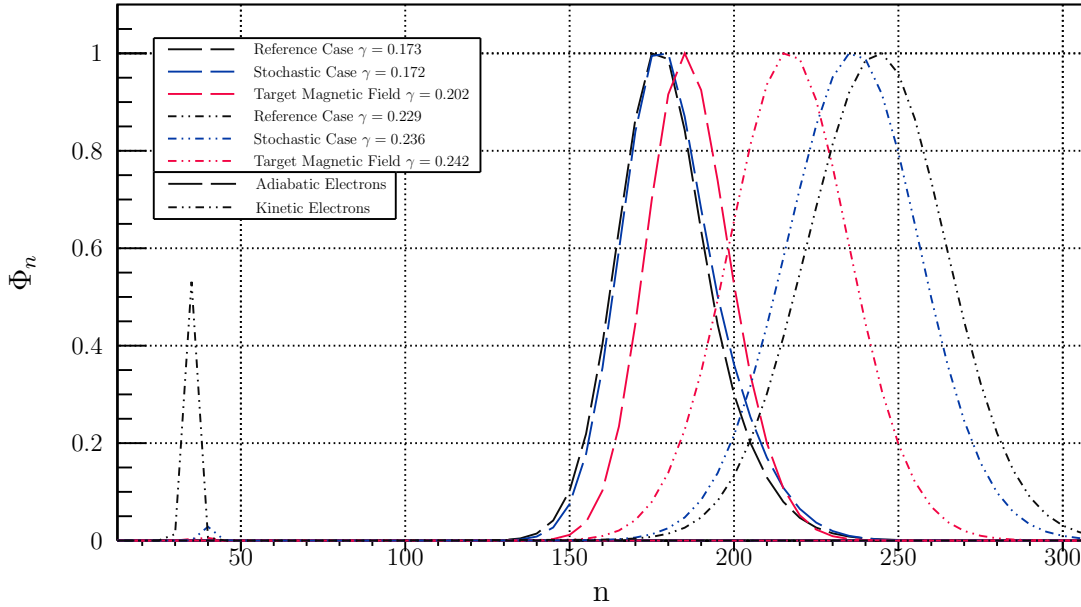


Figure 11: Most unstable modes in linear simulations of kinetic electrons

Therefore, we concentrate on nonlinear simulations of adiabatic electrons to measure the volume-averaged (electrostatic) ion heat flux. As can be seen from figure 12 the three equilibria behave almost identically for the first 250 time units. This confirms the linear results as the first part of virtually uninhibited growth (until $t \approx 100$) of a nonlinear simulation is often considered the linear phase until nonlinear effects start to take over. Hereafter, similarity or equality can only be determined statistically because two nonlinear simulations will never be exactly the same. Therefore, the qualitative features of the three equilibria are very similar since they all show the same development. After the first peak follows a dip and then another peak of heat flux. These fluctuations persist even on long time scales. Quantitatively, the heat flux averaged over time for the three equilibria is also very similar as well as their uncertainties. The uncertainty is computed as one standard deviation of the time trace in the interval used for averaging.

4.5.4. Conclusion Comparing three different free-boundary equilibria representing the W7-X high-mirror variant we find that the target magnetic field is actually linearly more unstable than the reference and stochastic case 8000. Between the reference and stochastic case 8000 we could only find minor differences in terms of mode structure or linear growth rate. Nonlinearly, the differences between the three equilibria are negligible. Therefore, considering the performed gyrokinetic simulations small differences in geometry do not affect the heat flux significantly. As the differences between the three different equilibria do not have a large impact on the GENE-3D results such that no additional runs were performed for the rest of the coil cases.

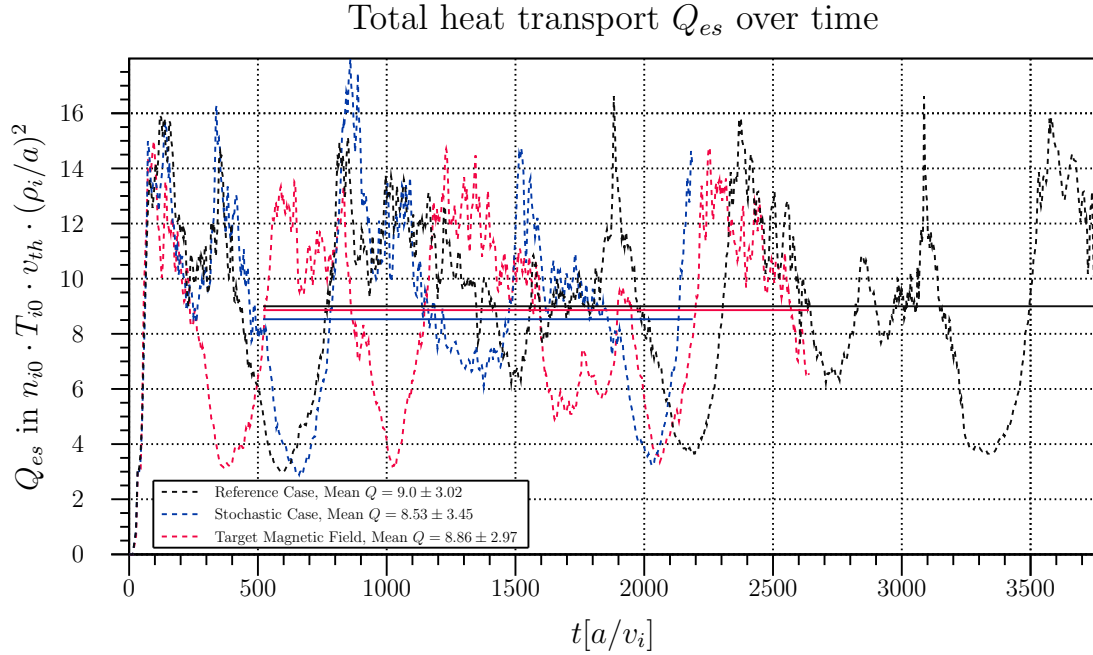


Figure 12: Heat flux development for the three different equilibria. Linear Phase, qualitative features and quantitative averages over time are all virtually the same. Here, n_{i0} and T_{i0} are the density/temperature at $\rho = 0.5$ and ρ_i is the ion Larmor-radius.

5. Discussion and conclusion

The magnetic fields of a stochastic stellarator coil optimization (*stochastic case N*) are compared with a magnetic field of the traditional stellarator coil optimization (*reference case*) on the basis of an identical optimization sequence. The results are compared with the *target magnetic field* used during the optimization. The coil sets are naturally ordered by their fitness w.r.t. the penalty function f , which measures the difference between the magnetic field produced by the coil configuration and the target magnetic field by means of several quality criteria. Except for the reference case (sample size 1), the ordering of the penalty values represents the number of samples used during the optimization: The higher the sample size, the lower the penalty value. The reference case lies between the stochastic case 2000 & 1000 and has a 20% lower penalty value than the stochastic case 8000. The stochastic case 100 has by far the highest penalty value, suggesting that it would have the worst performance. Each magnetic field is transformed into a $\langle \beta \rangle = 5\%$ equilibrium with VMEC and compared on the basis of the W7-X objectives [3], namely the Shafranov shift, stability and neoclassical transport properties, and the confinement of fast particles. At last, we investigate the gyrokinetic behavior of the stochastic case 8000, the reference case, and the target magnetic field.

The penalty function f represents the performance of the stochastic cases 8000 & 4000 & 2000 together with the reference case quite well when investigating the Shafranov shift, the neoclassical transport and the confinement of fast particles. The

target magnetic field, which has a penalty value of zero, shows in the latter two criteria the best performance, but only reflects its much better fitness w.r.t. f in the confinement of fast particles. The stability is not very well described by the penalty function and suggests that further improvement should be made. Interestingly, the stochastic cases 1000 & 100 show good results when investigating the performance criteria which means that the penalty function f did not represent their performance very well. Especially the surprisingly good performance of the stochastic case 100 questions the effectiveness of the penalty function f and shows again that an agreement in the vacuum magnetic field is not necessary for good performance (c.f. [13] and [14]). The investigation of the turbulent transport showed that the differences in the magnetic field geometry are too small to find reasonable differences in the heat flux.

Summarizing the performance investigation, the target plasma shape is optimal followed by the stochastic cases and concludes with the plasma shape of the reference case. This shows that stochastic stellarator coil optimization outperforms classic stellarator coil optimization irrespective of the number of considered samples. The original reason for introducing the stochastic coil optimization was to improve robustness, but it managed to also find coil sets that outperform the previously found coil set even when disregarding tolerances.

6. Outlook

The reason why stochastic stellarator coil optimization outperforms classic stellarator coil optimization irrespective of the number of considered samples when analyzing the physics properties of the corresponding magnetic fields is not fully understood. Stochastic optimization smooths out the optimization space which leads to lower field error values when the sample size is high enough. It is left to future work to investigate why stochastically optimized coil configurations with noticeably higher field error values performed better than the reference case.

The fitness ordering obtained from the penalty values after the optimization did not fully reflect the actual expected physics performance of the coil sets. This motivates to invent new proxies especially for the MHD stability. The coil optimization that we have been focusing on here takes as input the target magnetic field and is therefore limited to the performance of the target magnetic field, even if this target itself could be further optimized. Therefore, an obvious next step is to apply the stochastic framework to stellarator optimization, which concentrates on the optimization of the performance criteria directly.

7. Acknowledgement

The authors thank V. Perseo, C.D. Beidler, J. Geiger and J. Nührenberg for fruitful discussions and support. This work has been carried out within the framework of the EUROfusion Consortium and has received funding from the Euratom research and

training program 2014-2018 and 2019-2020 under grant agreement No 633053. The views and options expressed herein do not necessarily reflect those of the European Commission. This work was supported by a grant from the Simons Foundation/SFARI (560651, AB). The simulations presented in this work were performed at the HYDRA and COBRA HPC system at the Max Planck Computing and Data Facility (MPCDF), Germany and at the MARCONI HPC system at CINECA, Italy.

References

- [1] M. Drevlak, 20th Symposium on Fusion Technology, Marseille, France (1998) pp. 883.
- [2] J.-F. Lobsien et al., 2018 , Stellarator coil optimization towards higher engineering tolerances, *Nuclear Fusion*, 58(2018), pp. 106013
- [3] Wendelstein VII-X Application for Preferential Support, Wendelstein Project Group, IPP-EURATOM Association, AUGUST 1990
- [4] P. Merkel, Solution of stellarator boundary value problems with external currents, *Nucl. Fusion* (1987) **27** 867
- [5] Landreman, 2017, An improved current potential method for fast computation of stellarator coil shapes, *Nucl. Fusion*, **57** 046003
- [6] Paul, E.J., Landreman, M., Bader, A., Dorland, W.: An adjoint method for gradient-based optimization of stellarator coil shapes. *Nucl. Fusion* **58**, 076015
- [7] t. Brown et al., 2015, Engineering optimization of stellarator coils lead to improvements in device maintenance, *2015 IEEE 26th Symposium on Fusion Engineering (SOFE)*, pp 1-6
- [8] Zhu et al., 2017, New method to design stellarator coils without the winding surface, *Nucl. Fusion*, **58** 016008
- [9] H.-S. Bosch et al., Final integration, commissioning and start of the Wendelstein 7-X stellarator operation, *Nuclear Fusion*, Vol. 57, 116015 (2017)
- [10] R.L. Orbach, Statement about the Future of the Princeton Plasma Physics Laboratory, *Under Secretary for Science and Director, Office of Science*, U.S. Department of Energy, May 22, 2008
- [11] Lotz et al., 1990, Optimization, MHD mode and alpha particle confinement behaviour of Helias equilibria , *Procs. of 13th Conference IAEA*, IAEA-CN-53/C-III-5, p.603
- [12] Nührenberg J. and Zille R., 1988 *Physics Letters A* **129** 113-117
- [13] Long-Poe Ku, Allen H. Boozer, Stellarator coil design and plasma sensitivity, *Physics of Plasmas* **17**, 122503 (2010)
- [14] Zarnstorff M. et al., Physics of the compact advanced stellarator NCSX. *Plasma Physics and Controlled Fusion*,(2001) 43(12A), A237–A249.
- [15] C. Schwab, 1993, *Phys. Fluids*, B**5** 3195
- [16] Drevlak M., 2009, *36th EPS Conf. on Plasma Physics (Sofia, Bulgaria)*, P4.211, http://epsppd.epfl.ch/Sofia/pdf/P4_211.pdf
- [17] Kisslinger et al., 1990, Magnetic field and coil systems of the modular helias configuration HS 5-10, *Fusion Technology*, pp. 1520
- [18] Hirshman S.P. van Whitson J. C., 1983, *Phys. Fluids*, **26** 3553
- [19] Hirshman S.P. van Rij W.I. and Merkel P., 1986, *Comput. Phys. Commun.*, **43** 143
- [20] C. Nührenberg, Global ideal magnetohydrodynamic stability analysis for the configurational space of Wendelstein 7-X, *Phys. Plasmas*, 3 (1996) 2401
- [21] Strickler, D.J., Berry, L.A., Hirshman, S.P.m Designing Coils for Compact Stellarators. *Fusion Sci. Technol.* **41**, 107–115 (2002).
- [22] M. Drevlak, Automated Optimization of Stellarator Coils, *Fusion Technology*, Vol. 33, No. 2, Page 106-117, 1998
- [23] C. Nührenberg, Free-boundary ideal MHD stability of W7-X divertor equilibria, *Nuclear Fusion*, Vol. 55, 2016, pp. 076010

- [24] Bernstein I.B., Frieman E.A., Kruskal M.D. and Kulsrud R.M., 1958 *Proc. R. Soc. A* **244** 17
- [25] Beidler C. D. et al., 2011, *Nucl. Fusion*, **51** 076001
- [26] Nemov V.V. et al, 1999, Evaluation of $1/\nu$ neoclassical transport in stellarators, *Phys. Plasmas*, **6** 4622
- [27] Geiger J., 2015, Physics in the magnetic configuration space of W7-X , *Plasma Phys. Control. Fusion*, Vol. 57, Nr. 1
- [28] Hirshman S.P., Shaing K.C., van Rij W.I., Beasley C.O. and Crume E.C., 1986, *Phys. Fluids* **29** 2951
- [29] van Rij W.I. and Hirshman S.P., 1989, *Phys. Fluids B* **1** 563
- [30] Beidler C. D. et al. "Physics and engineering design for Wendelstein VII-X." *Fusion Technology* 17.1, (1990), 148-168.
- [31] Dinklage et al., 2007, Assessment of Global Stellarator Confinement: Status of the International Stellarator Confinement Database, *Fusion Science and Technology*, (51) 1
- [32] Turkin Y. et al., 2011, *Phys. Plasmas*, **18** 022505
- [33] Geiger J., 2007, Stability analysis of Wendelstein 7-X configurations with increased mirror ratio, *Proceedings of the 17th International Toki Conference*, P. 332-335
- [34] T. Sunn Pedersen et al., Key results from the first plasma operation phase and outlook for future performance in Wendelstein 7-X, *Phys. Plasmas* **24**, 2017
- [35] S. Äkäslompolo et al., Modelling of NBI ion wall loads in the W7-X stellarator, *Nuclear Fusion*, **29**, 2018
- [36] Canik, J. et al., Experimental Demonstration of Improved Neoclassical Transport with Quasihelical Symmetry, *Phys. Rev. Lett.*, (98) 8, p.085002, 2007
- [37] Hegna, C. et al., Theory of ITG turbulent saturation in stellarators: Identifying mechanisms to reduce turbulent transport, *Phys. Plasmas*, (25) 2, p.022511, 2018
- [38] Görler T. et al., The global version of the gyrokinetic turbulence code GENE, *Journal of Computational Physics*, 2011, **230**
- [39] Jenko F. et al., Electron temperature gradient driven turbulence, *Physics of Plasmas*, (7) 5, p.1904-1910, 2000
- [40] Jenko, F. et al., The GENE code, "http://genecode.org", 2019
- [41] Maurer M. et al., The 3D global version of the gyrokinetic turbulence code GENE, *To be submitted*, 2019
- [42] Xanthopoulos, P. et al., Controlling Turbulence in Present and Future Stellarators, *Phys. Rev. Lett.*, (113) 15, p.155001, 2014
- [43] Xanthopoulos, P. et al., Nonlinear Gyrokinetic Simulations of Ion-Temperature-Gradient Turbulence for the Optimized Wendelstein 7-X Stellarator, *Phys. Rev. Lett.*, (99) 3, p.035002, 2007
- [44] Boozer A., What is a Stellarator, *Physics of Plasmas*, **5** 5
- [45] R.C. Grimm, J.M. Greene, J.L. Johnson, *Methods of Computational Physics*, vol. 9 Academic Press, New York, London (1976), pp. 253-280

Appendices

Appendix A. Quality Criteria used during the Optimization

In table A1 we list the achieved values of the quality criteria of the reference & stochastic cases after the optimization together with the target values. Additionally, we show the corresponding penalty values in brackets (). The quality criteria are grouped in 4 categories and appeared at different stages during the optimization sequence. The

optimization sequence consisted of 6 optimization runs which differ in the values used for each individual quality criterion. A detailed list of the corresponding weights used in every single optimization run can be found in [2]. The optimization started with the field error together with the geometric properties and introduced the basic properties of the magnetic field in the second stage. The third stage was the optimization of the Fourier coefficients of an inner flux surface. We obtained the Fourier coefficients from the target magnetic field and optimized the corresponding coefficients in the magnetic field produced by the coil set. We use PEST coordinates [45] for this computation which assure identical poloidal angles for the different cases. In the corresponding row in table A1 we are presenting the penalty value instead of the 104 Fourier coefficients. A detailed description of the quality criteria and how they are computed in ONSET [1] can be found in [22].

Table A1: Values of the Quality Criteria

Quality Criteria:	Stochastic Case 8000:	Target Values:	Reference Case:
Maximum Local Field Error	6.0×10^{-2} (3.70)	(0)	7.0×10^{-2} (4.87)
Average Global Field Error	1.6×10^{-2} (1.25)	(0)	1.7×10^{-2} (1.45)
Curvature 1 (m^{-1})(Coil 1/2/3/4/5)	3.0/2.9/3.0/3.1/3.3 (9.2×10^{-2})	3.0 (0)	3.0/3.0/3.0/3.0/3.1 (7.0×10^{-3})
Curvature 2 (in 10^{-1})	2.7/3.1/5.1/6.1/6.2 (1.0×10^{-1})	0.3 (0)	3.6/4.2/5.6/5.1/5.4 (6.7×10^{-2})
Clearance (cm)	27/27/27.7/26.8/26.8 (1.4×10^{-3})	27 (0)	27/26.8/26.8/26.8/31 (3.1×10^{-3})
Magnetic Axis (bean-shaped cross.)	5.936 m (5.6×10^{-5})	5.934 m (0)	5.928 m (1.3×10^{-4})
Magnetic Axis (triangular cross.)	5.166 m (7.2×10^{-3})	5.17 m (0)	5.17 m (1.1×10^{-4})
Magnetic Mirror on Axis	0.10853 (8.8×10^{-6})	0.107 (0)	0.132 (1.9×10^{-3})
Iota on Axis	0.882 (9.9×10^{-7})	0.883 (0)	0.881 (3.9×10^{-3})
Magnetic Shear	1.521 (2.6×10^{-3})	1.56 (0)	1.49 (3.9×10^{-3})
Magnetic Well	8.1×10^{-3} (0)	7.0×10^{-3} (0)	5.4×10^{-3} (2.9×10^{-3})
Fourier Coeff. of inner Flux Surface	(2.83×10^{-1})	(0)	(2.44×10^{-1})
Total Penalty Value	(5.89)	(0)	(6.65)

Quality Criteria:	Stochastic Case 4000:	Stochastic Case 2000:
Maximum Local Field Error	5.7×10^{-2} (3.29)	6.0×10^{-2} (3.6)
Average Global Field Error	1.66×10^{-2} (1.39)	1.95×10^{-2} (1.9)
Curvature 1 (m^{-1})(Coil 1/2/3/4/5)	2.9/2.5/2.8/3.1/3.2 (4.0×10^{-2})	2.2/2.3/3.1/3.1/3.3 (8.5×10^{-2})
Curvature 2 (in 10^{-1})	2.2/2.4/4.1/5.3/5.4 (5.1×10^{-2})	2/3.1/4.5/5.4/5.3 (5.1×10^{-2})
Clearance (cm)	30.78/30.78/30.9/28/28 (0)	33.0/31.22/29.66/27.8/27.8 (0)
Magnetic Axis (bean-shaped cross.)	5.922 m (5.3×10^{-4})	5.923 m (5.0×10^{-4})
Magnetic Axis (triangular cross.)	5.158 m (6.4×10^{-2})	5.152 m (1.4×10^{-1})
Magnetic Mirror on Axis	0.0994 (1.1×10^{-3})	0.0953 (3.8×10^{-4})
Iota on Axis	0.8815 (6.2×10^{-8})	0.8849 (5.5×10^{-3})
Magnetic Shear	1.56 (9.2×10^{-2})	1.63 (4.2×10^{-3})
Magnetic Well	7.9×10^{-3} (0)	1.7×10^{-2} (0)
Fourier Coeff. of inner Flux Surface	0.646 (6.46×10^{-1})	(5.07×10^{-1})
Total Penalty Value	(5.48)	(6.3)

Quality Criteria:	Stochastic Case 1000:	Stochastic Case 100:
Maximum Local Field Error	7.0×10^{-2} (4.81)	8.0×10^{-2} (6.38)
Average Global Field Error	1.92×10^{-2} (1.85)	2.27×10^{-2} (2.58×10^{-2})
Curvature 1 (m^{-1})(Coil 1/2/3/4/5)	2.2/2.5/3.0/3.4/3.3 (1.7×10^{-1})	2.1/2.4/2.6/3.2/3.2 (3.2×10^{-2})
Curvature 2 (in 10^{-1})	1.9/2.2/3.2/6.1/4.8 (5.1×10^{-2})	1.7/3.5/3.9/4.8/5.0 (4.5×10^{-2})
Clearance (cm)	30.78/30.78/30.9/28/28 (0)	26.7/26/26/30.8/34.8 (0)
Magnetic Axis (bean-shaped cross.)	5.923 m (4.8×10^{-4})	5.94 m (1.6×10^{-4})
Magnetic Axis (triangular cross.)	5.174 m (1.1×10^{-2})	5.191 m (2.2×10^{-1})
Magnetic Mirror on Axis	0.1011 (8.8×10^{-5})	0.0975 (2.5×10^{-4})
Iota on Axis	0.879 (1.2×10^{-2})	0.8768 (6.6×10^{-2})
Magnetic Shear	1.43 (1.3×10^{-2})	1.52 (1.4×10^{-2})
Magnetic Well	1.8×10^{-2} (0)	1.6×10^{-2} (9.7×10^{-5})
Fourier Coeff. of inner Flux Surface	(7.34×10^{-1})	(9.62)
Total Penalty Value	(7.65)	(11.03)

Description:

Penalty Value Number in brackets ().

Field Error Normal magnetic field on the plasma boundary.

Clearance Minimum distance between adjacent coils.

Curvature 1 Maximum coil curvature.

Curvature 2 Weighted curvature defined in [\[22\]](#).

Magnetic Axis Central closed field line about which the other field lines wind [\[44\]](#).

Magnetic Shear Difference of iota on axis and an iota value off axis divided by the squared length.

A.3. Article III

»Improved performance of stellarator coil design optimization«

J.-F. LOBSIEN et al.

Journal of Plasma Physics, Vol. 86.2 (2020)

Improved performance of stellarator coil design optimization

Jim-Felix Lobsien^{1†}, Michael Drevlak¹, Thomas Kruger³, Samuel Lazerson¹, Caoxiang Zhu² and Thomas Sunn Pedersen¹

¹Max-Planck Institute for Plasma Physics, Wendelsteinstrasse 1, 17491 Greifswald, Germany

²University of Wisconsin Madison, Engineering Drive, Madison, WI 53706, United States of America

³Princeton Plasma Physics Laboratory, 100 Stellarator Rd, Princeton, NJ 08540, United States of America

(Received xx; revised xx; accepted xx)

Following up on earlier work which demonstrated an improved numerical stellarator coil design optimization performance by the use of stochastic optimization [Lobsien J., *Nucl. Fusion* **58** 106013], it is demonstrated here that significant further improvements can be made - lower field errors, and improved robustness - for a Wendelstein 7-X test case. This is done by increasing the sample size and applying fully 3D perturbations, but most importantly, by changing the design sequence in which the optimization targets are applied: Optimization for field error is conducted first, with coil shape penalties only added to the objective function at a later step in the design process. A robust, feasible coil configuration with a local maximum field error of 3.66% and an average field error of 0.95% is achieved here, as compared to a maximum local field error of 6.08% and average field error of 1.56% found in our earlier work. These new results are compared to those found without stochastic optimization using the FOCUS and ONSET suites. The relationship between local minima in the optimization space and coil shape penalties is also discussed.

1. Introduction

The construction cost of stellarators is dominated by the manufacturing and assembly process of the primary coil system, which produces the “magnetic cage” in which the plasma is later confined. Budget and schedule of the whole project strongly depends on the construction tolerances which are derived from a perturbation analysis after the primary coil system is designed. Unfortunately, the construction of recent stellarator experiments like Wendelstein 7-X (W7-X) and the National Compact Stellarator Experiment (NCSX) were negatively influenced by their low construction tolerances which led, in the case of NCSX, to the cancellation of the whole project [Orbach (2008)]. A method that increases construction tolerances without compromising the performance of the magnetic field would be highly beneficial.

We investigated the problem by integrating a perturbation analysis into the optimization loop of ONSET [Drevlak (1998b)], a nonlinear coil optimization suite. Instead of optimizing a single coil configuration, the average of a cloud of coil configurations is being optimized. Each element of the cloud is a perturbation of the coil set at the cloud’s center. The cloud is characterized by the number of samples N (perturbations) and its size is defined by the average perturbation amplitude. In our earlier work [Lobsien

† Email address for correspondence: jim.lobsien@ipp.mpg.de

et al. (2018)] that concentrated on coil configurations for the original W7-X plasma boundary the average perturbation amplitude was kept fixed at 2 mm while the number of samples N was varied between 1 and 8000. Each perturbation was two dimensional and displaced the coil set across its winding surface. For one sample this reduces to the non-stochastic case of classic stellarator coil optimization called the reference case. The stochastically optimized coil configurations were able to reproduce the target magnetic field more accurately with a local maximum field error of 6.08% and an average field error of 1.56% while we observed an increased resilience w.r.t. the objective function f . A subsequent derivation of reactor relevant $\langle\beta\rangle=5\%$ equilibria allowed us to analyse the performance of the coil configurations w.r.t. the criteria that originally led to the shape of the plasma boundary of W7-X. The investigation revealed that stochastic stellarator coil optimization outperforms classic stellarator coil optimization irrespective of the sample size [Lobsien *et al.* (2020)].

In this manuscript, we build on the results obtained in [Lobsien *et al.* (2018)] and study the effects of stochastic stellarator coil optimization with 3D perturbations on a different coil design process for the original W7-X plasma boundary. First, we solely concentrate on the field error, then implement the geometric and vacuum magnetic field properties in two subsequent phases. The number of samples is increased to $N = 20\,000$ while we test three different average perturbation amplitudes 0 mm, 2 mm and 5 mm. The case with a cloud size of 0 mm reduces again to the case of classic stellarator coil optimization called the reference case.

We also test here the effect of the nonlinear coil optimization tool FOCUS [Zhu *et al.* (2017)] to reduce the field error in the first phase of the design process. ONSET is then used to implement the geometric constraints and adjust the properties of the vacuum magnetic field. Following this procedure, we are able to compare the performance of two nonlinear coil optimization tools. Their differences w.r.t. the objective function f are described in section 2 together with the perturbation technique that is used in the stochastic version of ONSET. A detailed description of the design process closes the methodology. In section 3 we investigate the development of the field error during the design process and analyze the final fitness of the coil configurations. Their robustness w.r.t. the objective function f is investigated by a perturbation analysis. Lastly, we visualize the final coil configurations and conclude the investigation.

2. Methodology

The task of designing a stellarator coil system can be seen as the second step in the process of designing a stellarator. A given plasma boundary uniquely defines the vacuum magnetic field in its interior and together with a pressure and current profile the finite- β effects when a plasma pressure is applied. Intuitively, one first tries to find the optimal plasma shape that performs best w.r.t. predefined performance criteria like MHD stability, energy and particle transport, and fast particle confinement. In the second step one aims to reproduce the desired magnetic field with a finite set of coils. The magnetic field which later confines the plasma is the crucial element in this scenario by building the bridge between stellarator and coil optimization.

Deriving external currents that produce a given magnetic field is an inverse problem that is ill-posed, but can be solved linearly on a surface outside the plasma boundary with NESCOIL [Merkel (1987)] or its successor REGCOIL [Landreman (2017)] that allows different regularization schemes. The result is a continuous and smooth current distribution on the winding surface which can be discretized into a finite set of filaments that describe a coil set. The magnetic field of the coil set can be further improved with codes such as

ONSET [Drevlak (1998b)], COILOPT [Strickler *et al.* (2002)], COILOPT++ [Brown *et al.* (2015)] and FOCUS [Zhu *et al.* (2017)] which translate the problem into the minimization of a nonlinear objective function f . It consists of the parametrization h and the penalty function g , i.e. $f = g \circ h$.

ONSET and FOCUS show substantial differences in the choice of the coil parametrization (section 2.1), the quality criteria that define the penalty function (section 2.2), and the optimizer that minimize the objective function f . ONSET has several optimizers, but we use Brent's method [Gegenfurtner (1992)] which approximates the Hessian of f in an iterative process and optimizes along its principal axes. FOCUS, on the other hand, computes the gradient and Hessian [Zhu *et al.* (2018b)] of f analytically. FOCUS also has several optimizers to minimize the objective function f , but in this study, we will mainly use the conjugate gradient method. ONSET has the ability to optimize a coil configuration stochastically which perturbs the coil configuration to create a sample cloud. The technique is explained in section 2.3. The values of the weight constants ω_i define the coil design process (section 2.4) which is the path we chose to solve the coil optimization problem defined as

$$\min_{x \in \mathbb{R}^n} f(x), \quad (2.1)$$

where $x \in \mathbb{R}^n$ is the set of parameters describing the coil set. The objective function

$$f : \mathbb{R}^n \rightarrow \mathbb{R}, \quad f(x) = (g \circ h)(x) \quad (2.2)$$

consists of a parametrization $h : \mathbb{R}^n \rightarrow \mathbb{R}^{3S}$ which maps the set of parameters to a set of S filament points that describe the coil set in the 3D Euclidean space. Subsequently, the penalty function $g : \mathbb{R}^{3S} \rightarrow \mathbb{R}$ calculates the magnetic field with the Biot-Savart formula and measures the difference between the magnetic field produced by the coils and the target magnetic field defined by the shape of the plasma boundary. In detail, it calculates the quality criteria which are compared to the design values of the target magnetic field while it simultaneously assures that the shape of the coil set is feasible for construction.

2.1. Parametrization

Coil sets are parametrized differently in FOCUS and ONSET. FOCUS uses a three dimensional Fourier representation of the coil set, where each spatial coordinate is represented by

$$x^i(t) = x_{c,0}^j + \sum_{n=1}^{N_F} [x_{c,n}^j \cos(nt) + x_{s,n}^j \sin(nt)] \quad \text{with } t \in [0, 2\pi] \quad (2.3)$$

and $j = \{1, 2, 3\}$. This parametrization avoids the necessity of a winding surface. In total, the number of parameters defining a single coil is $3 \times (2N_F + 1)$.

The winding surface is an essential element of the parametrisation we chose in ONSET. Its two parts are visualized in figure 1. Each coil consists of $2 \times N_O$ parameters describing a cubic periodic spline in the two dimensional plane. The splines are then mapped by h onto two limiting surfaces. Additional N_O parameters then interpolate the winding surface between two limiting surfaces. The interpolation uses the arc tangent such that the winding surface can never reach the limiting surfaces. Full three-dimensional flexibility of the coil set can be achieved when the parametrisation is extended such that each coil has its own set of parameters that interpolate the winding surface between the two limiting surfaces. This way, each coil is attached to its own winding surface and can be displaced independently perpendicular to it. Such a flexibility is comparable to that available in FOCUS. The number of parameters then yields $3 \times N_O$ per coil.

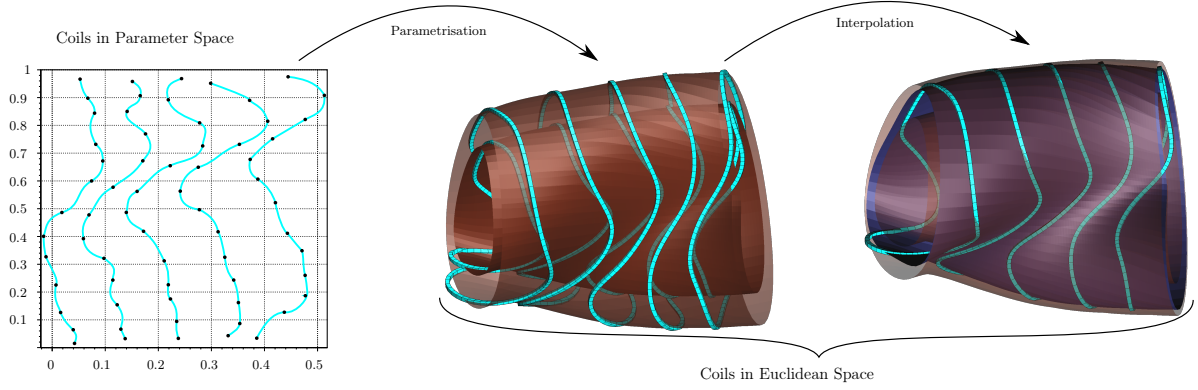


FIGURE 1. The parametrization used in ONSET.

We choose $N_O = 13$ and $N_F = 6$ such that ONSET and FOCUS use the same number of parameters per coil.

2.2. Penalty Function

In order to compute the value of the penalty function g , the magnetic field produced by the coil set is computed. Subsequently, characteristics of that magnetic field are derived called quality criteria. The analytic function that maps the quality criteria to the *penalty value* in \mathbb{R} is the last part of the calculation of the penalty function and is defined by

$$\sum_{i=1}^k \omega_i \left(q_i(x) - q_i^{design} \right)^2. \quad (2.4)$$

The value of the quality criterion $q_i(x)$ is subtracted by its design value q^{design} and yields, factorized by its weight constant ω_i , the specific contribution to the penalty function. The change of the weight constants ω_i defines the coil design process and is explained in section 2.4. The target plasma boundary uniquely defines the target vacuum magnetic field from which the design values q^{design} are derived prior the optimization.

The most dominant quality criterion is the field error evaluated by computing $\mathbf{B} \cdot \mathbf{n}$, where \mathbf{B} is the vector of the magnetic field produced by the coils and \mathbf{n} is the normal on the target plasma boundary. In general, \mathbf{B} may include internal plasma currents, which were absent in the optimization of W7-X. FOCUS minimizes the average squared field error

$$q_{ase}(x) = \int_A \frac{1}{2} (\mathbf{B} \cdot \mathbf{n})^2 dA, \quad (2.5)$$

where A is the area of the plasma boundary. ONSET uses two different measures for the normalized field error

$$q_{le}(x) = \frac{|\mathbf{B} \cdot \mathbf{n}|}{|\mathbf{B}|}. \quad (2.6)$$

The maximum local field error $\max q_{le}$ and the average global field error

$$q_{ae}(x) = \frac{\int_A q_{le} dA}{A}. \quad (2.7)$$

In ONSET, one can fully control the shape of the coil set by geometric constraints. The material used for the coils defines the finite extent of the coils which sets the minimal clearance between adjacent coils. This design process uses two limiting surfaces

which guarantee that the coils do not get too close or too far away from the plasma boundary. The finite extent of the coils also defines the maximal allowed coil curvature. Its computation in ONSET follows $\kappa = \frac{1}{R}$, where R is the smallest radius of curvature for a given coil. Unnecessary undulations are penalized by a second curvature which is a weighted variant of the first curvature described in [Drevlak (1998a)]. Ultimately, crossing points are penalized. These criteria define the geometric properties absolute necessary for the construction of the W7-X central coil system.

ONSET has additionally the capability to optimize properties of the vacuum magnetic field by following magnetic field lines and calculating magnetic flux surfaces. The properties and their calculation are explained in more detail in [Drevlak (1998a)] and briefly summarized here:

- The position of the magnetic axis is determined by finding the fixed-point of the field line map and two positions of the magnetic axis at the beginning and at the end of the half-module are evaluated.
- The difference between the magnetic field strength on the axis at the start and at the end of the half-module is referred to as the magnetic mirror. It is normalized to the sum of the two magnetic field strength values.
- The value of iota on the axis and the shear is determined. The latter is computed by taking the difference of iota on axis and iota 0.2m off axis at the beginning of the half-module at $z = 0$.
- The magnetic well (hill) is defined as the normalized difference of the specific volume of two well-separated magnetic surfaces (including the magnetic axis). The specific volume is defined as $\lim_{N \rightarrow \infty} \frac{1}{N} \int_N \frac{dl}{B} = \frac{dV}{d\Psi}$ where Ψ is the toroidal magnetic flux.
- The Fourier coefficients of inner flux surfaces can be computed and optimized towards the coefficients of the corresponding surfaces of the target magnetic field. They are derived in PEST coordinates [GRIMM *et al.* (1976)] and we chose the R_{mn} and Z_{mn} of a flux surface slightly inside the plasma boundary.

FOCUS has less control of the coil geometry than ONSET despite having penalty functions over the coil length, coil-to-coil separation, coil-plasma separation and coil curvature. To use analytic derivatives, FOCUS employs integrated formulas for these engineering constraints. The primary constraints used in this study are the coil length and coil curvature. The penalty on the coil length is

$$q_L(x) = \frac{1}{N_C} \sum_{i=1}^{N_C} \frac{1}{2} \frac{(l_i(x) - l_{i,o}(x))}{l_{i,o}(x)} \quad , \text{where} \quad l_i(x) = \int_0^{2\pi} |x'_i| dt \quad (2.8)$$

is the length of the i -th coil, $l_{i,o}$ is the target length and N_C is the number of coils. It has the disadvantage that chosen $l_{i,o}$ too low one can perfectly approximate the plasma boundary but cannot control the geometric properties of the coil. Chosen $l_{i,o}$ too high, one obtains values of the field error that are too large. The introduction of a penalty on the curvature improved the shape of the coil sets but could not completely avoid the violation of the second curvature and the coil-to-coil clearance used in ONSET. Compared to ONSET, the squared curvature was optimized. Due to technical limitations, a version of FOCUS that could use the curvature and coil-to-coil constraint was not available during our computations.

2.2.1. Remark:

Both ONSET and FOCUS have the ability to optimize additional physics properties. We list them here to give a full overview of the characteristics of the two coil optimization

ONSET:

- Following magnetic field lines, ONSET can check the existence of magnetic flux surface.
- On a flux surface ONSET can also compute:
 - The Fourier coefficients of the magnetic field H_{mn} in PEST coordinates.
 - Epsilon effective ϵ_{eff} .
- ONSET can detect the fixed-point of magnetic islands and optimize their width by computing their residual [Greene (1968)].
- ONSET has the ability to do equilibrium calculations with VMEC [Hirshman & Whitson (1983)] such that all performance criteria available in the stellarator optimization suite ROSE [Drevlak *et al.* (2018)] can be optimized.
- A NESCOIL calculation can be invoked to compute the current distribution needed to eliminate the residual field error. This is useful for optimizing systems of simple primary field coils (toroidal field component in a mixed-topology coil system) so as to minimize the burden on a saddle coil or permanent-magnet solution providing the rotational transform.

ONSET and FOCUS can optimize the current that flows through the coils. In this manuscript, all coils were equipped with an equal current of 1.45 MA.

FOCUS:

- FOCUS can detect magnetic islands and optimize the island width [Zhu *et al.* (2018a)].
- FOCUS can optimize the quasi-symmetry of the configuration [Zhu *et al.* (2018a)].

We did not optimize any of these properties because their investigation would be out of the scope of this manuscript.

2.3. Perturbation of the Coil Set

Stochastic coil optimization extends the optimization of a single coil configuration (c.f. equation (2.1)) to the optimization of a cloud of coil configurations

$$\min_{x \in \mathbb{R}^n} F_N(x). \quad (2.9)$$

The cloud is characterized by the number of samples N . Each element of the cloud is a perturbation of the original coil set at the cloud's center. A perturbation of the coil configuration can be intuitively achieved by perturbing the set of parameters that define the coil set. This leads to the objective function

$$F_N(x) := \frac{1}{N+1} \sum_{i=0}^N f(\xi_i(x)) + \omega_\sigma \sigma = \frac{1}{N+1} \sum_{i=0}^N (g \circ h \circ \xi_i)(x) + \omega_\sigma \sigma, \quad (2.10)$$

where $\xi_0(x) = x_0$ is the original parameter set and $\{\xi_i(x)\}_{i=1, \dots, N}$ is the set of perturbed parameter sets which have a Gaussian distribution around the cloud's center. The last term after the sum $\omega_\sigma \sigma$ is a penalty on the standard deviation σ of the penalty value distribution of one sample cloud. It is a tool of risk averse programming and intends to increase the robustness w.r.t. f . In the previous coil optimization study [Lobsien *et al.* (2018)], we only perturbed the parameters that deform the coil set across its winding surface. Here, we perturb all of the input parameters and assure that the deviation of the winding surface itself has the same magnitude as the deviation across the winding

Optimization Phase:	I	II	III
Maximum Field Error	0/ $1.0 \cdot 10^3$.	.
Mean Field Error	0/ $1.0 \cdot 10^5$.	.
Clearance	-	0.27 m/1	.
Curvature 1	-	$3 \text{ m}^{-1}/0.7$.
Curvature 2	-	0.3/0.4	.
Magnetic Axis (bean)	-	-	5.93 m/2450
Magnetic Axis (triangle)	-	-	7.17 m/2450
Magnetic Mirror on Axis	-	-	0.11/3
Iota on Axis	-	-	$0.88/1.5 \cdot 10^3$
Magnetic Shear	-	-	1.56/1.6
Magnetic Well	-	-	$0.007/1.0 \cdot 10^3$
Fourier Coeff. of Surface	-	-	varies/ $2.0 \cdot 10^2$
Limiting Surfaces	+30 cm/+75 cm	.	+30 cm/+80 cm
Points per Coil	13	.	.
Variables of WS	13	.	.
ω_σ	0.5	.	.

TABLE 1. Design Sequence in ONSET: q^{design}/ω_i

surface. The perturbation of the parameters has the disadvantage that the outcome of the displacement is hard to control and strongly depends on the parametrization.

We describe the extent of the cloud of samples in physical units of mm by the *average perturbation amplitude*. It is defined by

$$\frac{1}{N} \cdot \frac{1}{500} \sum_{i=1}^N \sum_{j=1}^{500} \overline{p_{ij} p_{ij}^u}, \quad (2.11)$$

where $\overline{p_{ij} p_{ij}^u}$ is the distance between the perturbed p_{ij} and unperturbed p_{ij}^u filament point. The sum goes over all the 500 filament points that describe a coil set and over all the coil sets in the cloud except the unperturbed one.

2.4. Design Sequence

The coil design process is divided into three phases. The first phase solely concentrates on the field error, the next phase then targets the geometric properties, and last but not least properties of the vacuum magnetic field are optimized. Each phase is defined by the corresponding values of the weight constants ω_i which are shown in table 1.

The optimization of the field error consists of multiple adjustments that shift the outer limiting surface further away to find the optimal coil-to-plasma distance. Similarly, we start the optimization phase with fewer points per coil to slowly increase the geometric freedom of the coil set while the weights for the field errors and the standard deviation ω_σ are kept fixed throughout the whole design process.

The 2nd design phase focuses on controlling and improving the geometric properties

while keeping the weights on the field error fixed. The whole process adjusts the weights of the coil-to-coil clearance and the two curvatures to their final values with the overall aim to not increase the value of the field error. This may not always be possible. In some cases, large kinks and/or self-intersections of the coils appear, and the code can get stuck with these unacceptable features, even after the geometric properties have been included in the penalty function in phase II. We find that this can be avoided by either using stochastic optimization already in phase I, or switching to phase II early, i.e. before having completed phase I. This is another indication that the optimization space has many local minima in which the optimizer can get stuck. The coil sets first optimized with FOCUS enter the design sequence with ONSET at phase II.

After the shape of the coil set meets the geometric constraints, the coil design process concludes with the optimization of properties of the vacuum magnetic field. The last design phase usually concentrates first on the magnetic axis, iota profile and the magnetic mirror and well, and then it concentrates on the Fourier coefficients of an inner flux surface. All the design values q^{design} were previously deduced from the target vacuum magnetic field which corresponds to the original W7-X plasma boundary. The boundary was first introduced in [Nührenberg & Zille (1988)], but the high-mirror configuration we are using is better described in [Nührenberg (1996)].

The design sequence described here is slightly different from the one used in the previous study [Lobsien *et al.* (2018)]. There, the geometric properties are optimized simultaneously to the field error such that phases I and II are combined into a single phase. In its concluding phase the weights of the vacuum field properties are reduced and the outer limiting surface is kept fixed at +75 cm.

3. Results

In this section, we investigate the effects of stochastic stellarator coil optimization using 3D perturbations. We follow the coil design process described in section 2.4 that consists of three phases. Two coil configurations are optimized using the stochastic version of ONSET with an average perturbation amplitude of 2 mm and 5 mm. In both cases, the cloud consists of 20 000 samples. The investigation includes two reference cases: One reference case passes the whole design process with the single sample version of ONSET, the other reference case is first optimized with FOCUS and then enters the design process with the single sample version of ONSET at phase II. We refer to them as reference case ONSET and HYBRID. In order to be consistent with the first design phase of the previous design process [Lobsien *et al.* (2018)], the two stochastic cases and the reference case ONSET use a single winding surface in phase I and II while in phase III they use the extended parametrisation where each coil is attached to its own winding surface. The perturbation used in the stochastic optimization always uses the current set of parameters that describe the coil set. The reference case HYBRID uses the extended parametrisation of ONSET throughout phase II and III.

3.1. Comparison after design phase I

In table 2 we list the maximal and average field error of the coil configurations after the completion of the first design phase.

The reference case HYBRID reaches by far the lowest average field error which is directly targeted through the average squared error in its objective function. Not directly covered is the maximal field error which is slightly higher than the value of the stochastic case 2 mm. The reduced coil flexibility of the stochastic case 2 mm in phase I inhibited

Coil Configuration:	Maximal Field Error	Average Field Error
Stochastic Case 2 mm	3.73×10^{-2}	1.3×10^{-2}
Stochastic Case 5 mm	6.64×10^{-2}	2.01×10^{-2}
Reference Case HYBRID	4.0×10^{-2}	0.53×10^{-2}
Reference Case ONSET	5.71×10^{-2}	1.37×10^{-2}
Stochastic Case 8000 [Lobsien <i>et al.</i> (2018)]	6.1×10^{-2}	1.59×10^{-2}

TABLE 2. Values of the maximal and average field error after design phase I.

a further reduction of the field error but is not responsible for the large difference in the average field error values compared to the reference case HYBRID.

In the previous study [Lobsien *et al.* (2018)], where geometric constraints were part of the penalty function g throughout the first design phase, the lowest field error values after its first design phase were achieved by the stochastic case 8000. Compared to these values, the stochastic case 2 mm could reduce the maximal field error by 40% and the average field error by 15%. This shows that in principle geometric constraints inhibit the optimization of the field error because they restrict the shape of the coil. The stochastic case 5 mm occupies the lowest rank which shows that an increase of the average perturbation amplitude negatively influences the optimization of the field error similar to geometric constraints.

We compare the speed and the corresponding efficiency of the three optimization approaches by the number of evaluations of their individual objective functions assuming that the evaluations takes a similar amount of time. In the stochastic optimization this does not include the 20 000 samples, since their computation is parallelized which only marginal contributes to the evaluation time due to the communication between the processes. FOCUS only needed 300 evaluations of its objective function f to arrive at that very low minimum. The stochastic case 5 mm needed 5000 evaluations of its objective function F_N , corresponding to 10^8 evaluations of f , to converge and the stochastic case 2 mm needed 28 000 evaluations of F_N (5.6×10^8 evaluations of f) to arrive at a slightly worse performing minimum. That is two orders of magnitude more evaluations of the objective function which shows the advantage of optimizing with derivatives.

3.2. Comparison after design phase II

The design phase II fully concentrates on implementing the geometric properties of the coil configurations. This was not possible for the reference case ONSET because the geometric penalties used in the design process were not able to repair the kink in coil number 1 counting from left. We visualize the reference case ONSET together with both stochastic coil cases in figure 2. Both have a much smoother coil shape, which shows that the technique of stochastic coil optimization works as a geometric constraint and reduces the maximal and average coil curvature.

The development of the field error in phase II is especially interesting, because geometric constraints are not necessary to obtain an optimal approximation of the desired magnetic field. We visualize the values of the two stochastic cases and the reference case HYBRID in table 3. The relatively low field errors increased in the stochastic case 2 mm and in the reference case HYBRID which shows again that geometric constraints

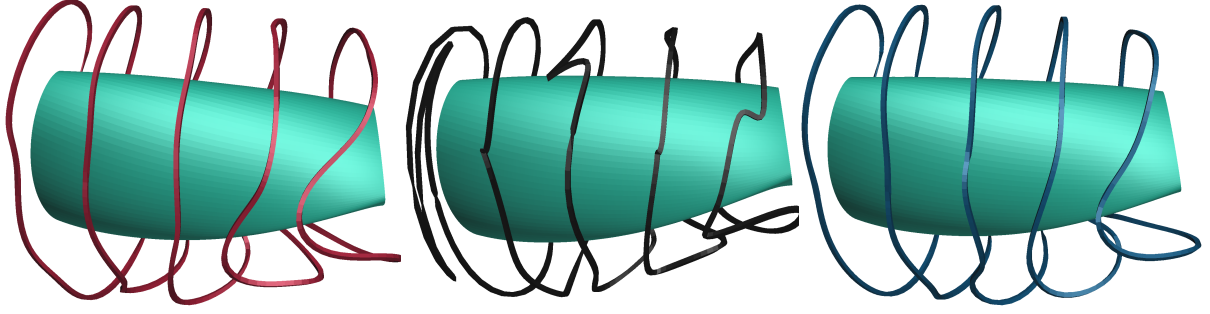


FIGURE 2. The stochastic case 2 mm is situated left, the reference case ONSET is situated in the middle and the stochastic case 5 mm is situated right.

Coil Configuration:	Maximal Field Error	Average Field Error
Stochastic Case 2 mm	4.8×10^{-2}	1.38×10^{-2}
Stochastic Case 5 mm	5.39×10^{-2}	1.50×10^{-2}
Reference Case HYBRID	3.44×10^{-2}	0.69×10^{-2}

TABLE 3. Values of the maximal and average field error after design phase II.

negatively influence the optimization of the field error. But the relatively high field errors of the stochastic case 5 mm decreased. This does not contradict the previous statement because in principle geometric constraints just change the landscape of the optimization space. An optimization which was previously halted by the increased average perturbation amplitude can continue to minimize the field error if the change of the landscape includes a beneficial change of the local minimum. The increase in field error indicates that geometric constraints set the lower boundary of the field error. We point out that the stochastic case 2 mm still has lower field error values than the stochastic case 8000 (c.f. table 2) which shows the advantage of adding shape penalties at a later step in the design process when using stochastic optimization.

FOCUS can reduce the field error to values much lower than shown in table 2 by increasing the length of the coil. It gives the coil more freedom to take shape and thus better approximate the magnetic field. Unfortunately, the field error later increased again in phase II to values higher than shown in table 3. This shows that for a coil configuration with our desired geometric properties the average coil length of 8.5 m is optimal to approximate the magnetic field of the W7-X configuration. This is confirmed by the average coil length of the two stochastic cases.

The absence of a penalty on the coil curvature in FOCUS could initially in phase I also reduce the field error to values lower than shown in table 2, but they increased again in phase II to values higher than shown in table 3. The situation was not as fatal as for the reference case ONSET but it shows that the geometric constraints can be beneficial and can prevent the optimizer from entering local minima that are far from the global minimum.

3.3. Comparison after design phase III

In this section we investigate the fitness and robustness of the two stochastic cases together with the reference case HYBRID after they completed the coil design process.

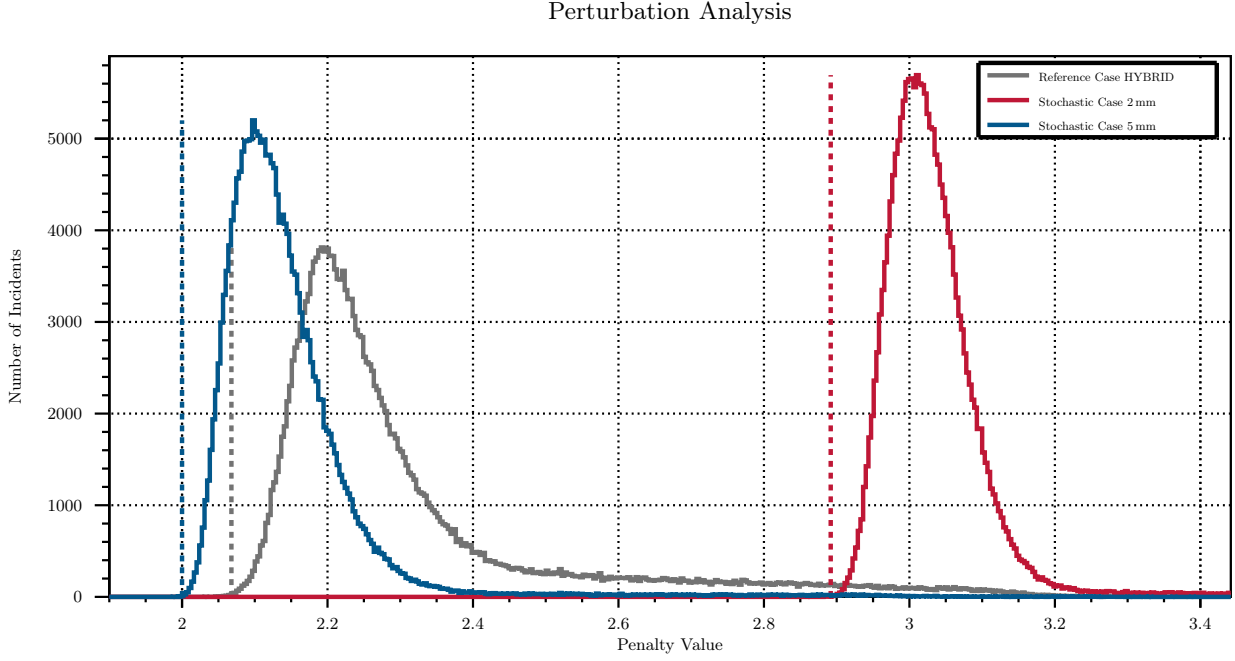


FIGURE 3. Perturbation analysis of the two stochastic cases and the reference case HYBRID. All the coil sets were perturbed 200 000 times by changing the input parameters. The vertical dashed line shows the penalty value of the unperturbed coil configuration.

The total fitness is represented by the penalty value and the robustness is visualized by the penalty value histograms obtained by a perturbation analysis. Each coil configuration is perturbed 200 000 times with an average perturbation amplitude of 2 mm. Their penalty value histogram together with the penalty value of the unperturbed coil configuration is shown in figure 3.

The stochastic case 5 mm has the lowest penalty value after the completion of the design process which needed 58 000 evaluations of the objective function F_N (1.16×10^9 evaluations of f). Closely behind follows the reference case HYBRID which needed 86 000 evaluations of the objective function f to complete phase II & III. The stochastic case 2 mm arrives at a slightly higher penalty value but needed only 69 000 evaluations of F_N (1.38×10^9 evaluations of f) to conclude the design process. This means that the larger the average perturbation amplitude, the fewer evaluations are necessary to converge. Figure 3 additionally shows that a larger average perturbation amplitude does not necessarily lead to a lower performance. The penalty value histogram of the stochastic case 2 mm shows the highest peak and the smallest width. Thus, the coil configuration is most robust w.r.t. the objective function f which is closely followed by the stochastic case 5 mm. The lowest robustness w.r.t. f shows the reference case HYBRID with a noticeable difference to the stochastic cases. This was expected because it was not optimized for that.

We visualize the field errors after the completion of the design process in table 4. The penalties on the properties of the vacuum magnetic field and the increased flexibility through the extended parametrisation in phase III could further reduce the field error of the stochastic cases, which means that the design process before ended again in a local minimum. The design process of the reference case HYBRID took a completely different path, because it started with a very low average field error which increased during the design process and only the maximum field error slightly decreased. During phase II and III, coil configurations that used a stronger penalty on the coil length in FOCUS could not decrease their final field error to values lower than shown in table 4, whereas

Coil Configuration:	Maximal Field Error	Average Field Error
Stochastic Case 2 mm	4.32×10^{-2}	1.09×10^{-2}
Stochastic Case 5 mm	3.66×10^{-2}	0.95×10^{-2}
Reference Case HYBRID	3.45×10^{-2}	0.72×10^{-2}
Stochastic Case 8000 [Lobsien <i>et al.</i> (2018)]	6.08×10^{-2}	1.56×10^{-2}

TABLE 4. Values of the maximal and average field error after design phase III.

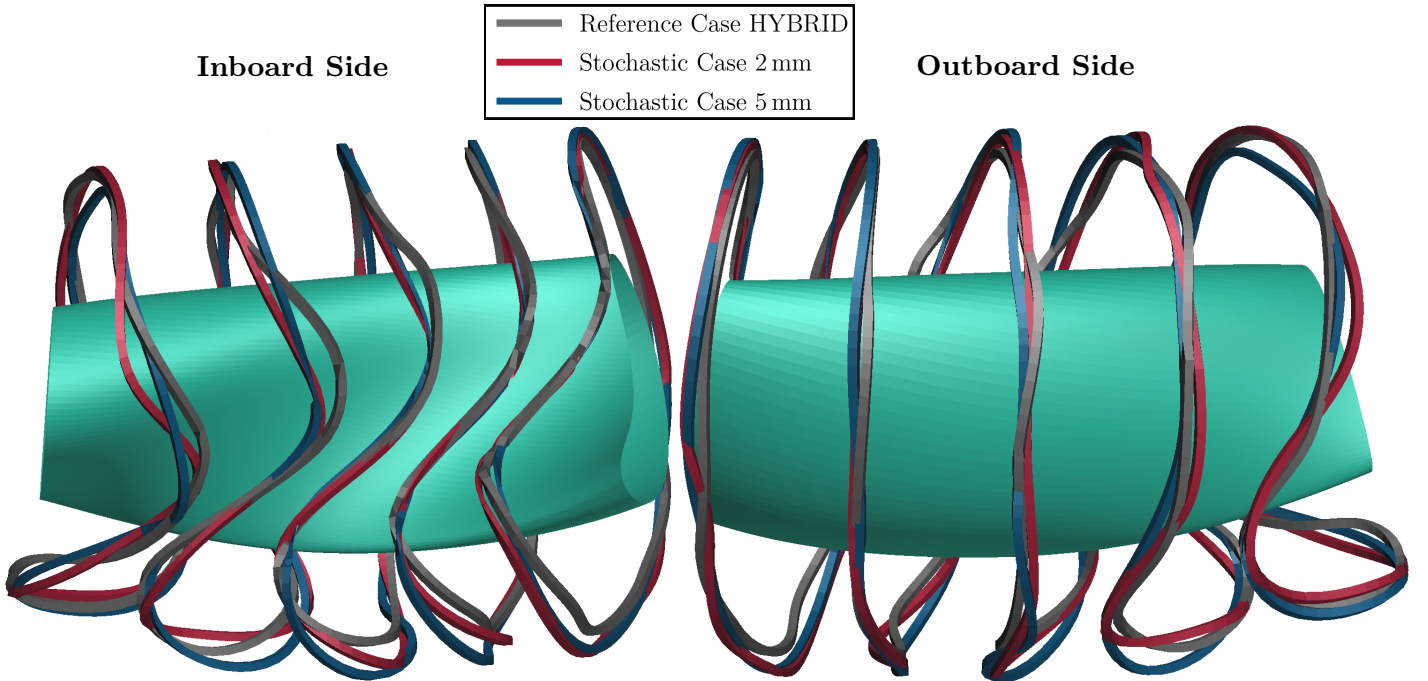


FIGURE 4. The final coil configurations of the reference case HYBRID together with two stochastic cases are shown from both sides.

a weaker penalty led to field error values as well higher than shown in table 4. All of the coil configurations discussed here have reached lower field error values than the best results of previous W7-X design studies [Lobsien *et al.* (2018)] [Drevlak (1998a)] .

3.4. Picture of the Coil Configurations

In figure 4 we visualize the coil configuration of the two stochastic cases and the reference case HYBRID after they completed the coil design process. Although having similar fitness their coil shapes are quite different and only coincide at the diagonal section on the inboard side (c.f. figure 4 right).

4. Discussion and conclusion

We investigated the effects of 3D stochastic stellarator coil optimization and followed a coil design process for the original Wendelstein 7-X plasma boundary that focused on the reduction of the field error. The design process consists of three phases: Field error, geometric properties, and properties of the vacuum magnetic field. The stochastic

optimization is used with an average perturbation amplitude of 5 mm, 2 mm and 0 mm, with the latter case reducing to the single sample version of ONSET, i.e. the reference case ONSET. Unfortunately, the reference case ONSET could not finish the design process successfully, which shows that certain geometric properties are necessary to prevent the optimizer from entering a local minimum that leads to unpractical coil shapes. The stochastic case 5 mm completed the design process and reached the lowest penalty value of exactly 2 and consequently the best fitness. Its field errors are 3.66% maximal and 0.95% on average and except of phase II they reduced over the course of the design process. With the aim to put our results into a broader perspective, we used the FOCUS code to reduce the field error in phase I and then finished the design process with the single sample version of ONSET. This reference case HYBRID concluded with a slightly higher penalty value of 2.07 but lower field error values of 3.45% maximal and 0.72% on average. In contrast to the two stochastic cases, the field error increased during the optimization of the geometric and vacuum magnetic field properties (phase II and III). This is consistent with, but does not prove that the field error values obtained here are close to a global field error minimum of a coil configuration that meets the geometric constraints necessary to build Wendelstein 7-X. Comparing the results to our previous design study [Lobsien *et al.* (2018)] it shows that the absence of most of the geometric constraints in the first phase of the design process in combination with an increased sample size and fully 3D perturbations yielded lower field error values. We conclude that geometric constraints are responsible for the creation of local less performing minima in which the optimizer got stuck.

We have shown in this paper that the enhanced robustness in our previous study can be extended to three-dimensional perturbations facilitated by the penalty on the standard deviation $\omega_\sigma \sigma$. We also compared the penalty value histograms for coil sets designed with the stochastic version of ONSET and ones designed with FOCUS first and then ONSET. The robustness of the reference case HYBRID w.r.t. the objective function is noticeably lower than the two stochastic cases. This is consistent with our previous finding that the stochastic optimization approach tends to improve robustness, although stochastic optimizations with FOCUS in the future will shed more light on this. The FOCUS code uses nearly two orders of magnitude fewer evaluations for similar results in phase I.

We also found that, when optimizing with FOCUS in phase I and with ONSET for phase II and III without stochastic optimization, results are improved significantly over previous non-stochastic optimizations, but still less well performing and significantly less robust than the best stochastic optimization results.

4.1. Remark on geometric constraints

A coil configuration needs to fulfil certain geometric properties such that its design can be realized during a subsequent construction. The corresponding geometric constraints used during the optimization have a strong effect on the optimization space. Omitting them completely leads to a reduction of the field error, but allows the optimization to arrive in a non optimal minimum that terminates the design process. From testing stochastic stellarator coil optimization without geometric constraints we can say that a penalty on the coil curvature is necessary to prevent such a situation, but previous studies have shown that a penalty that is too large has a negative effect on the field error. The study conducted in this manuscript shows that one is able to fix the geometric properties at a later step in the design process, when the coil configuration was optimized with only a small penalty on the curvature, without dramatically increasing the field error. To summarize, geometric constraints are necessary to prevent the optimizer from getting stuck in non optimal minima, but chosen to high can halt the whole optimization process.

5. Acknowledgement

The authors thank L. Rudischhauser and D. Böckenhoff for fruitful discussions and support. This work has been carried out within the framework of the EUROfusion Consortium and has received funding from the Euratom research and training program 2014-2018 and 2019-2020 under grant agreement No 633053. The views and options expressed herein do not necessarily reflect those of the European Commission. This work was supported by a grant from the Simons Foundation/SFARI (560651, AB). The simulations presented in this work were performed at the HYDRA and COBRA HPC system at the Max Planck Computing and Data Facility (MPCDF), Germany and at the MARCONI HPC system at CINECA, Italy.

REFERENCES

- BROWN, T., BRESLAU, J., GATES, D., POMPHREY, N. & ZOLFAGHARI, A. 2015 Engineering optimization of stellarator coils lead to improvements in device maintenance. In *2015 IEEE 26th Symposium on Fusion Engineering (SOFE)*, pp. 1–6.
- DREVLAK, MICHAEL 1998*a* Automated optimization of stellarator coils. *Fusion Technology* **33** (2), 106–117, arXiv: <https://doi.org/10.13182/FST98-A21>.
- DREVLAK, MICHAEL 1998*b* Coil designs for a quasi-axially symmetric stellarator. *20th Symposium on Fusion Technology Marseille France* p. 883.
- DREVLAK, M., BEIDLER, C.D., GEIGER, J., HELANDER, P. & TURKIN, Y. 2018 Optimisation of stellarator equilibria with ROSE. *Nuclear Fusion* **59** (1), 016010.
- GEGENFURTNER, KARL R. 1992 Praxis: Brent’s algorithm for function minimization. *Behavior Research Methods, Instruments, & Computers* **24**, 560–564.
- GREENE, JOHN M. 1968 Two-dimensional measure-preserving mappings. *Journal of Mathematical Physics* **9** (5), 760–768, arXiv: <https://doi.org/10.1063/1.1664639>.
- GRIMM, RAY C., GREENE, JOHN M. & JOHNSON, JOHN L. 1976 Computation of the magnetohydrodynamic spectrum in axisymmetric toroidal confinement systems. In *Controlled Fusion* (ed. JOHN KILLEEN), *Methods in Computational Physics: Advances in Research and Applications*, vol. 16, pp. 253 – 280. Elsevier.
- HIRSHMAN, S. P. & WHITSON, J. C. 1983 Steepest-descent moment method for three-dimensional magnetohydrodynamic equilibria. *The Physics of Fluids* **26** (12), 3553–3568, arXiv: <https://aip.scitation.org/doi/pdf/10.1063/1.864116>.
- LANDREMAN, MATT 2017 An improved current potential method for fast computation of stellarator coil shapes. *Nuclear Fusion* **57** (4), 046003.
- LOBSIEN, JIM-FELIX, DREVLAK, MICHAEL, JENKO, FRANK, MAURER, MAURICE, NAVARRO, ALEJANDRO BAÑON, NÜHRENBURG, CAROLIN, PEDERSEN, THOMAS SUNN, SMITH, HÅKAN M. & AND, YURIY TURKIN 2020 Physics analysis of results of stochastic and classic stellarator coil optimization. *Nuclear Fusion* **60** (4), 046012.
- LOBSIEN, JIM-FELIX, DREVLAK, MICHAEL & PEDERSEN, THOMAS SUNN 2018 Stellarator coil optimization towards higher engineering tolerances. *Nuclear Fusion* **58** (10), 106013.
- MERKEL, P. 1987 Solution of stellarator boundary value problems with external currents. *Nuclear Fusion* **27** (5), 867–871.
- NÜHRENBURG, CAROLIN 1996 Global ideal magnetohydrodynamic stability analysis for the configurational space of wendelstein 7–x. *Physics of Plasmas* **3** (6), 2401–2410, arXiv: <https://doi.org/10.1063/1.871924>.
- NÜHRENBURG, J. & ZILLE, R. 1988 Quasi-helically symmetric toroidal stellarators. *Physics Letters A* **129** (2), 113 – 117.
- ORBACH, R.L. 2008 Statement about the future of the princeton plasma physics laboratory. *Under Secretary for Science and Director, Office of Science, U.S. Department of Energy*.
- STRICKLER, DENNIS J., BERRY, LEE A. & HIRSHMAN, STEVEN P. 2002 Designing coils for compact stellarators. *Fusion Science and Technology* **41** (2), 107–115, arXiv: <https://doi.org/10.13182/FST02-A206>.
- ZHU, CAO XIANG, HUDSON, STUART R, LAZERSON, SAMUEL A, SONG, YUNTAO & WAN,

- YUANXI 2018*a* Hessian matrix approach for determining error field sensitivity to coil deviations. *Plasma Physics and Controlled Fusion* **60** (5), 054016.
- ZHU, CAO XIANG, HUDSON, STUART R., SONG, YUNTAO & WAN, YUANXI 2017 New method to design stellarator coils without the winding surface. *Nuclear Fusion* **58** (1), 016008.
- ZHU, CAO XIANG, HUDSON, STUART R., SONG, YUNTAO & WAN, YUANXI 2018*b* Designing stellarator coils by a modified newton method using FOCUS. *Plasma Physics and Controlled Fusion* **60** (6), 065008.



Acknowledgements

I wish to express my sincere appreciation to my supervisor, Thomas Sunn Pedersen, who has the substance of a genius: he convincingly guided and encouraged me to be professional and do the right thing even when the road got tough. Without his persistent help, the goal of this project would not have been realized. The assistance and guidance of Michael Drevlak is truly appreciated. Without his support, this project could not have reached its goal. I am indebted to Per Helander and Samuel Lazerson whose support proved monumental towards the success of this thesis. I wish to thank Golo Fuchert, Maurice Maurer, Carolin Nührenberg and Craig Beidler whose assistance was a milestone in the completion of this project. I would like to recognize the fruitful discussions with Hakan M. Smith and Jürgen Nührenberg. I wish to acknowledge the support and great love of my family, my mother, Anne-Rose; my father Jochen; and my brother, Valentin. They kept me going on and this work would not have been possible without their input.